ENERGY PARTITIONING IN BALLISTIC IMPACT FRAGMENTATION OF TITANIUM BORIDE

by

Madhusudan Jagannathan

A thesis submitted to the faculty of
The University of Utah
in partial fulfillment of the requirements for the degree of

Master of Science

Department of Metallurgical Engineering

The University of Utah

December 2010

The University of Utah Graduate School

STATEMENT OF THESIS APPROVAL

The thesis of **Madhusudan Jagannathan**

has been approved by the following supervisory committee members:

Ravi Chandran	, Chair	**09/02/2010** Date Approved
Zhigang Zak Fang	, Member	**09/02/2010** Date Approved
Rebecca Brannon	, Member	**09/02/2010** Date Approved

and by **Jan Miller** , Chair of

the Department of **Metallurgical Engineering**

and by Charles A. Wight, Dean of The Graduate School.

ABSTRACT

The study focuses on setting up a laboratory-scale ballistic testing apparatus in order to investigate the mechanisms through which the ballistic energy of a projectile is dissipated by a nearly monolithic nanostructured ceramic (titanium boride or TiB) and to determine the partitioning of the ballistic energy. From the past research in our group, it has been found that nanostructured TiB possesses attractive mechanical properties such as high hardness and high elastic modulus which makes it a potential candidate for armor applications.

The ballistic testing system consisted of a chamber made from compressed rubber pads with a backing plate made of steel or aluminum (on which the target sample was attached) and a rifle mounted on a rest pad at the other end. To validate the testing system, mild steel plates of three thicknesses were impacted with bullets having velocities in the range of 700 to 830 m/s. The velocities were controlled by varying the amount of gunpowder load in the bullets. Complete penetration was observed in the thin plates (with thickness 9.5 mm) whereas the penetration was partial in the 15.9 and the 19.1 mm thick plates.

Two batches of nine TiB plates with thicknesses varying between 5 mm to 18 mm were hot pressed and impacted by bullets having velocities in the range of 725 to 750 m/s. Aluminum backing plates were glued to the TiB plates to help in calculating the energy absorbed by the ceramic. The thinner TiB plates had a larger proportion of finer

fragments compared to the thicker plates. The calculated energy of fragmentation for the TiB plates was found to be negligible with respect to the bullet kinetic energy. The energy spent in backing plate deformation was calculated by adding the energies for bending and tensile stretching of the plate. It was found that for the thinnest TiB plate (5 mm), the percentage of the bullet energy that went into backing plate deformation was close to 50 % whereas for plates thicker than 12 mm, it was between 5-10 %. The energy absorption of the TiB plates increased with the plate thickness but beyond a certain thickness (15 mm), the increase was not significant. The kinetic energy of the fragments, erosion of the bullet, sound, heat, and light appear to be additional mechanisms of energy dissipation.

To my parents, Mr. S. Jagannathan and Mrs. Padma Jagannathan

TABLE OF CONTENTS

LIST OF TABLES

LIST OF FIGURES

ACKNOWLEDGMENTS

I would like to express my heartiest gratitude to my dissertation advisor, Dr. Ravi Chandran, for providing me with the opportunity to pursue this research project under his guidance. His encouragement and suggestions through different stages of the project made the research work interesting and challenging. I would also like to thank Dr. Zak Fang and Dr. Rebecca Brannon for serving on my supervisory committee and for their valuable input.

I am grateful to Shawn Madhta, Paul Chang, and Biplab Sarma for their ideas and support in the laboratory over the course of this research. Special thanks to Dr. Rajamani for guiding me on the topic of fragment sieve analysis and to Robert Burns for helping me set up the hot press. This acknowledgment would not be complete without thanking Kay Argyle and Karen Haynes for their help and cooperation.

This research was funded by the Office of Economic Development of the State of Utah under the Center of Excellence Program and by the National Science Foundation.

CHAPTER 1

INTRODUCTION

1.1 History

Ceramics have been extensively used to provide protection against fast moving impact threats in personnel as well as vehicular armor. The threats include kinetic energy penetrators, soft core and hard core bullets, and high velocity shaped charge jets. Ceramics are often preferred over metals in various armor applications, because they offer better ballistic resistance, at lower densities. Ceramic tiles are usually attached to the surfaces of land vehicles to provide additional protection [1]. Kevlar, a synthetic fiber developed by DuPont, is commonly used in bullet-proof and stab-proof jackets worn by police/military forces. These vests are reinforced with hard ceramic facings where the threat is more severe, for example, during warfare [2].

The first use of ceramics in armor applications was in 1918, when it was observed that a hard enamel coating on steel improved its resistance to bullets [3]. The early ceramic armor systems consisted of alumina tiles bonded to ductile backing panels like aluminum or glass fiber reinforced plastic (GFRP). Such panels were fastened to UH-1 helicopter seats and provided reasonably good ballistic protection [4]. During the 1960s, Norton Company developed boron carbide (B_4C) tiles for armor applications by hot pressing at high temperatures. Owing to its lower density, B_4C-based armor systems were

about 30% lighter than the alumina systems. Since armor systems were mainly developed for personnel and helicopter protection, the armor weight was a crucial factor and hence, B_4C was an attractive alternative. Currently, B_4C is used in personnel armor vests for soldiers. Many companies have developed improved methods to fabricate B_4C tiles of different shapes and sizes. These companies, however, are faced with the challenge to make the manufacturing processes more economical [4, 5].

Since the 70s, other ceramics such as silicon carbide (SiC) and titanium diboride (TiB_2) have also been used successfully in armor systems. Hot pressing is the most common fabrication method for ballistic ceramics because most of these ceramics are covalently bonded and hence, have high melting points. B_4C, TiB_2, and SiC powders are typically hot pressed at about 2150-2200°C and using pressures of around 1000 psi, often under controlled atmospheres. Because of the high temperatures involved, carbide and boride ceramics are expensive to fabricate. Oxide ceramics like alumina, on the other hand, can be manufactured through various processes like slip casting and injection molding but have relatively lower hardness and strength values [6].

1.2 Ceramic Armor System

Armor systems, in general, consist of a hard brittle ceramic facing the projectile with a soft deformable backing material. The ceramic destroys the projectile tip, slows it down, and distributes the load over a large area of the backing. The backing supports the ceramic and brings the comminuted ceramic and projectile to rest [3]. The backing material is selected on the basis of structural, ballistic, and weight considerations [7]. Kevlar, fiberglass, Spectra, and aluminum are most commonly used as the backing material. Kevlar is a high modulus, low density fiber developed by DuPont. Its

subsequent replacement of conventional E-glass in glass fiber reinforced plastic has reduced the overall armor weight by about 10-12% [6].

The mechanical properties of a ceramic determine its ballistic efficiency. The hardness of the ceramic causes the erosion and disintegration of the projectile, thus preventing further penetration. The armor plate is exposed to very high bending stresses; hence, the ceramic must have high flexural strength and high tensile strength. If the fracture toughness of the material is too low, the crack propagation might be too severe after the impact which can damage the ceramic significantly. This can reduce the degree of multihit protection offered by the ceramic armor system. Lower density is preferred as it reduces the overall weight of the armor. An ideal armor ceramic material must have a combination of these desired properties and should also be easy to manufacture.

1.3 New Armor Materials

There has been considerable interest in the use of ceramic matrix composites (CMCs) for armor applications. The damage after impact in ceramic matrix composites is not as severe as in monolithic ceramics and hence, the CMCs can show better multihit performance. Some of the systems which have been tested for armor applications include Al_20_3/SiC whiskers, Ni/TiC, borosilicate glass reinforced with SiC or C fibers, TiB_2/B_4C particulates, TiB_2/SiC particulates, Al/B_4C particulates, and Al reinforced with various ceramic particulates or whiskers. CMCs are more expensive to fabricate than monolithic materials [8].

Newer materials have also been developed to replace the traditional glass-only transparent armor systems. Saint Gobain Crystals have developed transparent sapphire (Al_20_3) sheets as a component of a laminated armor system. These sheets break apart the

core of the armor piercing projectile which makes it easier for the subsequent layers of glass and backing materials to defeat the smaller and lower energy projectile [9].

Our research group at the University of Utah has successfully fabricated near monolithic nanostructured titanium boride (TiB) through hot pressing and has investigated its mechanical properties [10]. TiB was found to show high hardness, high flexural strength, and good fracture toughness levels. The material can be fabricated by hot pressing at < 1400°C, which is a relatively lower temperature compared to the sintering temperatures involved in the synthesis of other armor ceramic materials. These factors make TiB an attractive candidate for use in armor applications.

1.4 Objectives of the Present Research

The focus of this thesis is the characterization of ballistic performance of TiB. A laboratory ballistic test system was built and the ballistic performance of the near monolithic TiB was determined. The main objectives of this research are the following:

- To set up a laboratory ballistic test system where the projectile velocity can be controlled within acceptable limits.
- To validate the ballistic testing setup using metallic plates as targets.
- To fabricate near monolithic nanostructured TiB plates of different thicknesses and to evaluate their ballistic performance as a function of plate thickness.
- To investigate the mechanisms through which the ballistic energy of a projectile is dissipated by TiB and to determine the partitioning of the ballistic energy.

CHAPTER 2

LITERATURE REVIEW

2.1 Ballistic Ceramics

A ceramic can be defined as a solid compound formed by the application of heat, sometimes along with pressure, and consists of two elements of which at least one is nonmetallic. The other element can be a metal or a solid nonmetal [11]. Ceramics generally possess high hardness and stiffness values and melt at very high temperatures. These properties can be attributed to the strong ionic/covalent bonding between the elements. Some of these ceramics are preferred in armor applications due to the attractive combination of mechanical properties and low density [12]. The properties that are considered as desirable in a ceramic material, from the point of view of armor, will be discussed in this section. The influence of a ceramic's microstructure on these properties will also be discussed.

2.1.1 Mechanical Properties and Microstructure of Ceramics

In ceramics, the microstructural parameters, especially the grain size, shape, and orientation, play a key role in determining its basic mechanical properties such as tensile and compressive strengths, hardness, toughness, and wear properties. These properties are generally considered to be important in defeating projectiles [12].

For most ceramics, compressive strength is inversely proportional to the square

root of the grain size with strengths extrapolating to single crystal values at infinite grain size. This relation is similar to the Hall Petch relationship in metals. Similar trends are observed for tensile or flexural strength values. In general, there is a decrease in the tensile strength with increasing grain size. As can be seen from Figure 2.1, this decrease is modest at fine grain sizes but becomes stronger at larger grain sizes. This has been explained by the presence of machining-flaws. The flaws are larger than the size of fine grains and smaller than that of the large grains. Carniglia [13] suggested that microplasticity was the failure mechanism for the finer grain sizes. For the larger grain sizes, where the flaw dimensions are comparable to or greater than the grain sizes, the suggested failure mechanism was Griffith flaw failure. The change in the slope could be attributed to the transition from one failure mechanism to another.

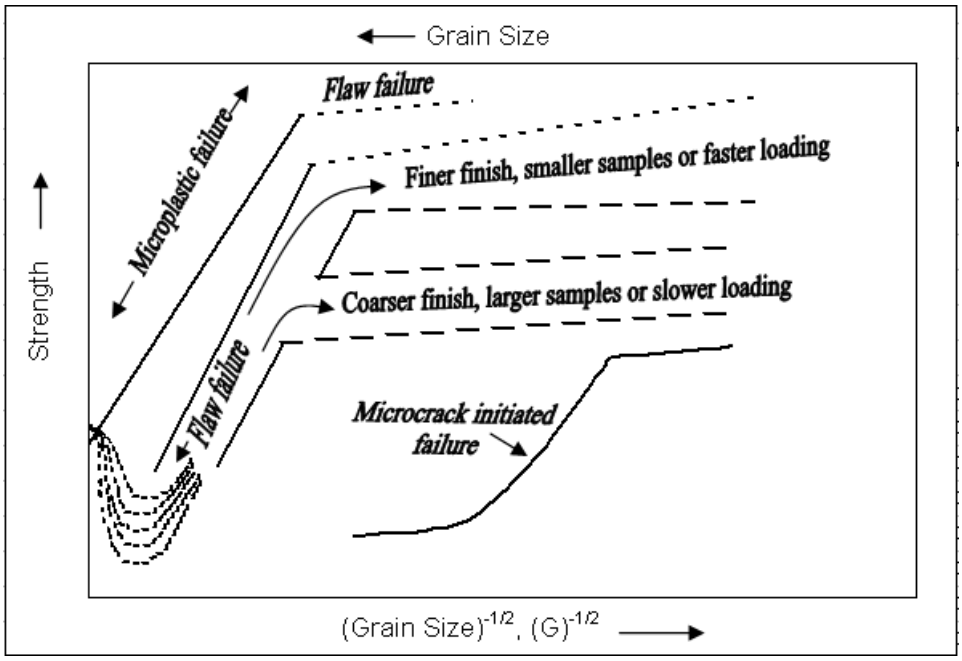

Fig. 2.1 Common trend of tensile strength vs. (Grain size, G)$^{-1/2}$ in ceramics. Adapted from [12]

The ceramic hardness also decreases with an increase in the grain size, G. The functional form of hardness variation is $\propto G^{-1/2}$, similar to that observed for strength. In some ceramics [14] such as MgO, Al_20_3, $MgAl_2O_4$, ZnS, and B_4C, the hardness decreases with increasing grain size until it reaches a minimum value, which is lower than the single crystal values, for a particular grain size. It then increases with grain size approaching single crystal values. This minimum is believed to be due to the increased grain cracking and spalling around indents when the indent and the grain sizes are similar [12].

Fracture toughness is an important property that affects the ballistic performance of ceramics. The fracture toughness is a strong function of bonding and microstructure in ceramics. In addition to grain size, fracture toughness is influenced by grain shape, presence of second phases, grain orientation, and porosity.

For cubic ceramic materials, in general, the dependence of fracture toughness on grain size is limited over the range of grain sizes from a few microns to ~ 100 microns. However, cubic ceramics like β- SiC, ZnS, and MgO [15] tested over a large range of grain sizes, tend to show a maximum toughness, a modest value, for intermediate values of grain size.

Noncubic materials show a more pronounced dependence of fracture toughness on grain size. For example, Al_2O_3 and B_4C show definite maximum fracture toughness values at particular grain sizes [16]. In some ceramics, the fracture toughness remains constant over a range of grain sizes or decreases with grain size, as in the case of TiB_2 [16].

The physics of failure in a typical ballistic impact is very different from

conventional failure because of the very high loading rates involved. The failure front propagates at speeds approaching the velocity of sound in both the projectile and the ceramic. Ferguson and Rice [12] conducted ballistic tests on fully dense alumina bodies with different grain sizes and purity levels using 0.22″ caliber ductile bullets. These tests showed some increase in the stopping power as the grain size became finer and the purity levels increased in Al_2O_3 materials (Figure 2.2). The stopping power was calculated as the ballistic limit velocity (the velocity at which half the projectiles penetrate the target and half fail to do so) normalized by the ceramic areal density (weight per unit area). However, this grain size dependence is not clear for heavier projectiles [12].

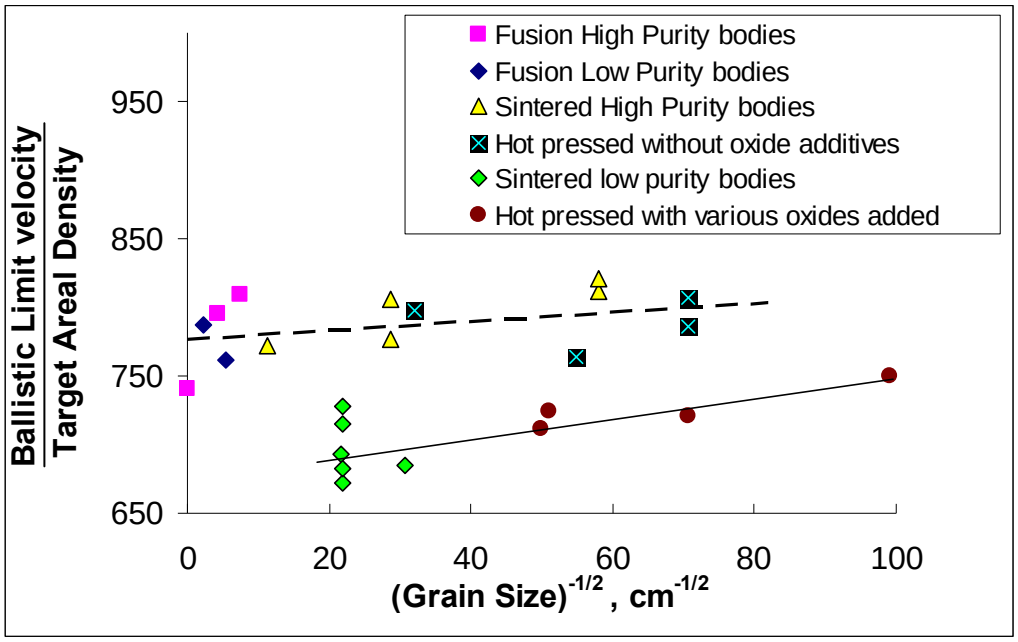

Fig. 2.2 Ballistic efficiency of ceramic vs. (Grain Size) $^{-1/2}$ for different alumina bodies. Adapted from [12]

2.1.2 Influence of Mechanical Properties of Ceramics on Ballistic Performance

Though no direct correlation has been found between the ballistic performance of a ceramic and its mechanical properties, researchers have attempted to study the role of individual properties in determining the ceramic's resistance to penetration. The following properties are generally believed to have some influence on the ballistic resistance of a ceramic.

1. Hardness: Woodward *et al*. [17] observed that the act of blunting the projectile can decrease its ability to penetrate a backing material. If the ceramic has sufficient hardness to blunt or destroy the projectile tip, the ballistic efficiency is improved. Reijer [18] suggested that the ceramic hardness must be greater than that of the penetrator in order to erode the tip of the projectile. He observed that any further increase is not necessarily beneficial. Hardness is one of the few properties which has been used directly to predict the ballistic performance of a ceramic [19].

2. Strength: Shockey *et al*. [20] suggested that the compressive strength of the ceramic dictates the initial resistance to the projectile to a certain extent. The projectile tip can be fractured, deformed, and deflected depending on the strength. If the stress at the tip exceeds the projectile strength and the projectile is relatively short, it can be defeated. However, for longer projectiles, the intact rear portion might continue to penetrate the ceramic even after the front is severely blunted or destroyed.

High stress gradients exist in the ceramic material between the area under the projectile core (under compression) and the regions adjacent to the contact area which experience tensile stresses. These gradients cause high shear stresses and therefore, a high

shear strength will enable a ceramic to resist failure more efficiently [21]. Low flexural strengths are unacceptable as the ceramic experiences tensile and bending loads during the impact.

3. Density: Lower density is beneficial for armor material not only because it can decrease the overall weight of the armor but also because it allows a thicker ceramic to be used without much increase in the weight [18, 21]. However, lower density achieved by incomplete densification is not preferred as porosity can lead to deterioration of the key mechanical properties [22].

4. Bulk, Shear, and Elastic Moduli: These properties are responsible for resisting deformation to failure and hence, must be as high as possible to defeat the projectile [21]. In particular, the Young's modulus for ballistic ceramics should be high. The velocity of sound in the material determines how efficiently the impact energy can be dissipated away from the impact site. It is given by

$$C = \sqrt{\frac{E}{\rho}} \tag{2.1}$$

where C is the sonic velocity, E, the Young's modulus, and ρ, the density of the material [8]. Hence, higher Young's moduli and lower densities lead to higher sonic velocities. High sonic velocity also indirectly indicates good densification or low porosity [22].

5. Hugonoit Elastic Limit (HEL): This is defined as the yield stress of a material under uniaxial dynamic loading [23]. This is important because during the initial stages of the impact, very high transient pressures are reached near the point of impact [24]. Materials dynamically loaded beyond their HEL might lose their yield strength

drastically compared to the materials that experience loads below the HEL [3].

6. Fracture Toughness: The influence of fracture toughness on the protective power of a ceramic is not well understood. Some ceramics with high K_{1C} values like zirconia do not exhibit good ballistic performance. It has been observed in many ceramic systems that the second phases and reinforcements which often increase the fracture toughness by crack bridging and branching typically lead to poorer armor performance [12]. But on the other hand, researchers [22] have been able to design carbide-based and metal infiltrated ceramics such as SiC/Al with elevated K_{1C} values that provide good ballistic protection. The crack propagation must not be too severe after the first strike to retain multihit capability. To achieve this, it appears that an optimum balance between the hardness and the fracture toughness must be maintained.

Apart from these factors, as discussed in Section 2.1.1, microstructural features also influence the crack propagation mechanisms and hence, the ballistic response of a ceramic [22]. The projectile stopping power of a ceramic depends on more than one property and changes with the nature of the projectile. However, most of the successful armor ceramics show similar trends in some properties, which suggest the dependence of their ballistic performance on these properties to an extent. The better performing armor ceramics typically have high Young's Moduli and indentation hardnesses, moderate to low densities (at low porosity), and moderate to fine grain sizes [12].

2.1.3 Common Ballistic Ceramics

The ceramic materials used for ballistic protection can be either monolithic structural ceramics or ceramic matrix composites. Oxide ceramics like alumina (Al_2O_3) and nonoxide ceramics like silicon carbide (SiC), boron carbide (B_4C), and titanium

diboride (TiB_2) are the most commonly used monolithic structural ceramics [25]. To gain an understanding of the requirements for a good ceramic armor material, it is important to look into the mechanical properties and the relative ballistic performances of each one of these ceramics.

2.1.3.1 Aluminum Oxide (Al_20_3)

Aluminum oxide or alumina has a combination of high hardness and high wear resistance with low friction coefficient. Alumina, in general, is used in both single crystal and polycrystalline forms in various applications requiring heat resistance and wear resistance. In advanced applications, whisker-reinforced and transformation-toughened forms are used. Its common applications include refractories, spark plug insulators, armor, and bearings. However, its high brittleness is a major disadvantage that severely limits its extent of application. Al_20_3 does not show any plastic deformation until about 1200°C. Alumina's low toughness makes it especially vulnerable to thermal and mechanical shock loading.

Alumina ceramics can be fabricated by a variety of processes, including slip casting, hot pressing, and injection molding, without the need for expensive equipment. These ceramics are fabricated with varying contents of alumina. The materials containing more than 95% alumina are commonly referred to as high alumina ceramics while those with at least 99% are termed as high purity alumina ceramics [26, 27]. It has been observed that the hardness, Young's modulus, and sound velocity increase with the Al_20_3 content [22].

2.1.3.2 Titanium Diboride (TiB_2)

TiB_2 is a ceramic with relatively high specific strength, hardness, and wear resistance. Current applications of this ceramic include wear resistant coatings, armor, cutting tools, and crucibles.

Hot pressing, hot-isostatic-pressing (HIP), pressureless sintering, and microwave sintering can be used to yield nearly fully dense TiB_2. Pressureless sintering is particularly advantageous because it reduces the complexity of equipment and near-net shape components can be fabricated. Pressureless sintering requires high temperatures in the range of 2000˚C but grain growth is also promoted at these temperatures. Therefore, sintering aids like Cr, CrB_2, Carbon, Ni, Fe, etc. are used to reduce the sintering temperature to about 1700-1800˚C. The sintering time is also reduced in the presence of these aids to about 1 hour. Nearly dense TiB_2 components or samples have been fabricated at 1600º C with the help of Si_3N_4 as sintering aid. In this case, the formation of SiO_2 eliminates the titanium oxide layer on the surface of the sample. When transition metals like Fe, Ni, or Co are used as sintering aids, the sinterability is improved because of the formation of a liquid phase between the particles. The elastic modulus of TiB_2 is very high (560 GPa) and like most ceramics, it is stronger in compression than in flexure or tension [28, 29].

2.1.3.3 Boron Carbide (B_4C)

Boron carbide is an exceptionally hard material that has a relatively high strength, low density, and good wear resistance. Diamond and cubic boron nitride (CBN) are the only materials harder than B_4C [30]. B_4C is used in ballistic vests, cutting tools, grit blast nozzles as wear coatings, and in the B10 isotope enriched form for nuclear shielding and

control rods. It is used as a thermoelectric material as it has a high Seebeck coefficient and in beta voltaic batteries due to its tolerance to radiation damage.

Boron carbide has a compositional range from $B_{4.3}C$ to $B_{11.2}C$. The commonly available powders and monoliths tend towards the carbon rich limit. The unit cell consists of 12 atom icosahedra bonded by 3 atom chains. The chains are rich in carbon and are stiff while the icosahedra have more B and can deform under stress. The chain is responsible for the mechanical performance and the chain composition and distribution affects the mechanical properties [31].

Boron carbide cannot be fabricated using cold pressing and sintering or pressureless sintering techniques. Typically, B_4C is hot pressed at a temperature of 1900-1950°C and a pressure of about 50 MPa, often under inert gas atmospheres [30]. Sintering should be done at a temperature below 2250°C to avoid the peritectic decomposition into carbon rich phase and boron. Activated sintering can be achieved by finely grinding B_4C powders or by using nonstoichiometric phases of B_4C. High cost of hot pressing and finish machining and low fracture toughness (< 3 $MPa.m^{1/2}$) are some of the disadvantages associated with B_4C. The fracture toughness can be improved [31] by using additives like CrB_2, from 2.5 to 3.5 $MPa.m^{1/2}$. It has been observed that the presence of these additives changes the dominant fracture mechanism from transgranular to intergranular. The increase in the fracture toughness is attributed to crack deflection.

2.1.3.4 Silicon Carbide (SiC)

SiC is one of the most widely used nonoxide ceramics. It has high hardness, moderate strength, and good strength retention at high temperatures. It exists as two forms: β-SiC having a cubic structure and α-SiC comprised of different hexagonal and

rhombohedral modifications. Its common applications include automobile brakes, heating elements, armor plates, and high temperature semiconductor electronics [26]. It is also used in seals and bearings because of its high corrosion resistance [32].

Synthetic SiC is formed by the reaction between Si and C. This is known as Acheson process [33]. The manufacturing processes used to fabricate SiC materials are reaction bonding (mixing SiC powder with carbon or silicon powder), second phase bonding (using a mixture of SiC with resin, glass, clay, etc.) , sintering, and CVD reaction bonding. Pure SiC does not sinter without pressure.

Sintering of fine SiC powder can be achieved using boron and carbon as sintering aids. The sintering is carried out typically at 2150° C for about half an hour to achieve complete densification. The carbon prevents formation of silicon dioxide whereas boron enhances diffusion [26]. To obtain the hexagonal form of SiC (α-SiC), the processing temperature should be less than 1650°C to prevent phase transformation [6].

2.1.4 Comparison of Mechanical Properties of the Ballistic Ceramics

A comparison of some of the mechanical properties of commonly used ballistic ceramics is provided in Table 2.1. As was seen in Section 2.1.2, these properties are believed to have some influence on the ballistic resistance of the ceramics.

B_4C is one of the hardest ceramics whereas TiB_2 and SiC are also endowed with reasonably high hardness values. The hardness will help in eroding the projectile tip more efficiently and is hence preferred. SiC and B_4C have comparable elastic moduli whereas TiB_2 has an exceptionally high value (550 GPa). While TiB_2 and SiC have similar sonic velocities, B_4C has a higher sonic velocity. A higher sonic velocity would lead to a

Table 2.1 Comparison of mechanical properties of ballistic ceramics. Adapted from [34]

Material, Manufacturing process	**Density (g/cc)**	**Vickers Hardness (GPa) (tested at different loads)**	**Fracture Toughness K_{IC} ($MPa.m^{1/2}$)**	**Young's Modulus (GPa)**	**Sonic Velocity (km/s)**	**Flexural Strength (MPa)**
Alumina, sintered	3.60-3.95	12-18	3.0-4.5	300-450	9.5-11.6	200-400
Silicon carbide, sintered	3.10-3.20	22-23	3.0-4.0	400-420	11.0- 11.4	300-340
Silicon carbide, hot pressed	3.25-3.28	20	5.0-5.5	440-450	11.2-12.0	500-730
Boron carbide, hot pressed	2.45-2.52	29-35	2.0-4.7	440-460	13.0-13.7	200-500
Titanium diboride, sintered	4.55	21-23	8.0	550	-	350
Titanium diboride, hot pressed	4.48-4.51	22-25	6.7-6.95	550	11.0-11.3	270-700

higher rate of energy dissipation. TiB_2 has the highest fracture toughness followed by Al_2O_3, SiC, and then B_4C. From the properties in the table, it can be summarized that the high hardness and the high sonic velocity of B_4C, coupled with its low density, are responsible for its excellent ballistic resistance and its extensive use in personnel armor.

Apart from these properties, the cost of manufacturing also plays an important role in the eventual usage of these ceramics in armor applications. Nonoxide ceramics generally have better mechanical properties and relatively lower densities (except titanium diboride). But most of these ceramics are manufacturable only by hot pressing at elevated temperatures and are hence expensive. Alumina does not possess properties as attractive as the other carbides, but is still preferred in some armor applications due to its

low cost and its fabricability by a variety of processes without the need for expensive equipment [34].

2.2 Ballistic Behavior and Testing

Before going on to discuss the relative ballistic performances of each of the above mentioned ceramics, a discussion on the ballistic penetration process and the ballistic testing methods is necessary.

2.2.1 Physics of Ballistics

It is essential to understand the physics behind the ballistic impact on ceramic armor systems in order to appreciate how the kinetic energy of the bullet is dissipated during the penetration. Metal plates absorb the projectile energy by localized plastic deformation which is manifested by the formation of craters and bulges.

2.2.1.1 Ballistic Impact on Fabric Composites

In Kevlar bullet-proof jackets, the long fiber strands form a dense net which absorbs the ballistic energy. The fibers distribute the impact over the entire vest so that the trauma is not felt locally [2]. Such fibers have high elastic modulus and low densities, thus having a high wave velocity which helps in distributing the impact energy over a wider area and prevents large strains from developing at the impact point. After the impact, transverse shock waves as well as longitudinal waves travel through the fibers. The longitudinal wave propagates at the speed of sound in the material from the point of impact through the impacted fibers. This leads to straining of the fibers which is considered to be the most important energy absorbing mechanism. However, the longitudinal wave cannot propagate if the fiber ruptures at the point of impact due to high

stresses. Hence, the fibers should also have high ultimate tensile strengths [35].

2.2.1.2 Ballistic Impact on Ceramic Armor Systems

The mechanism of energy absorption is quite different in ceramic systems. A schematic of the ballistic response of a composite ceramic armor system is illustrated in Figure 2.3. The ceramic destroys and erodes the projectile tip, decelerates it, and distributes the load over a large area of the composite. The backing plate supports the ceramic and brings the comminuted ceramic and projectile to rest.

An effective ceramic armor should dissipate the impact over as large an area as possible in order to prevent localized loading which can cause "behind armor blunt trauma" (BABT). In personnel armors, BABT is a principal injury mechanism, especially with fast moving projectiles. It is caused by the deformation and impact from the rear

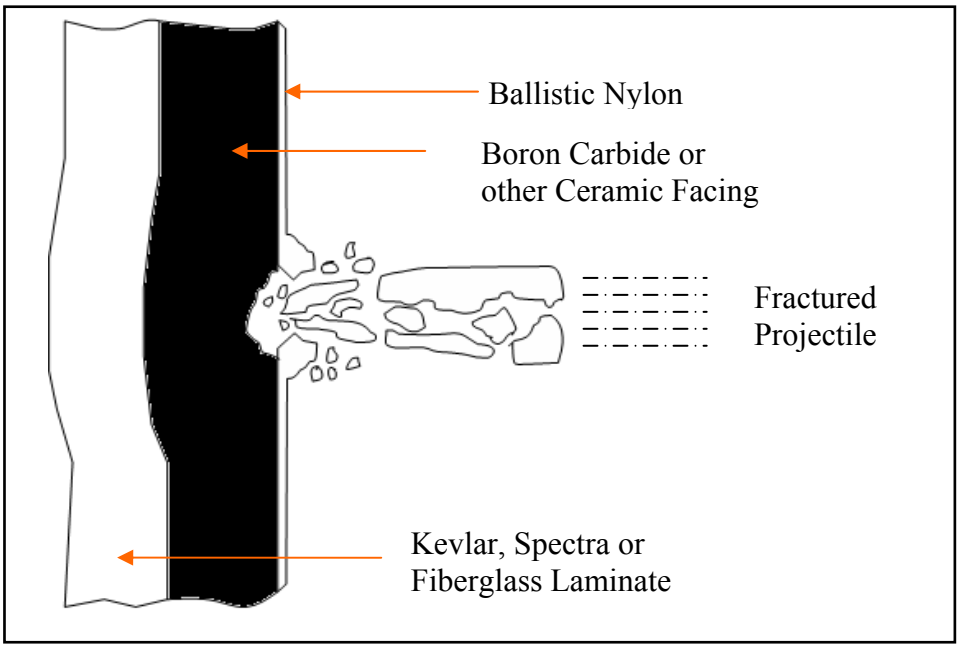

Fig. 2.3 Schematic of a ballistic impact on a ceramic armor system. Adapted from [6]

surface of the vest armor to the torso of the user. In some cases, it can result in fatal events like rib fracture, cardiac injury, or pulmonary contusion even if the projectile has been defeated [36-38].

2.2.1.3 Damage to Ceramic Plate

Most of the military threats fall in the range of intermediate velocities, *i.e.*, between 700 and 3000 m/s. For this regime, the penetration can be divided into many stages. Figure 2.4 shows four such stages in a typical ceramic armor configuration. The stages are (1) initial impact with hydrodynamic flow of penetrator and armor ceramic; (2) breakup and continued flow of the penetrator and high speed jetting of ceramic; (3) ceramic fracture, formation of the Hertzian cone crack, and tensile crack on the rear face; and (4) erosion of the penetrator and widespread fracture of the ceramic [8].

Surface waves propagate outward till they reach the lateral boundaries of the

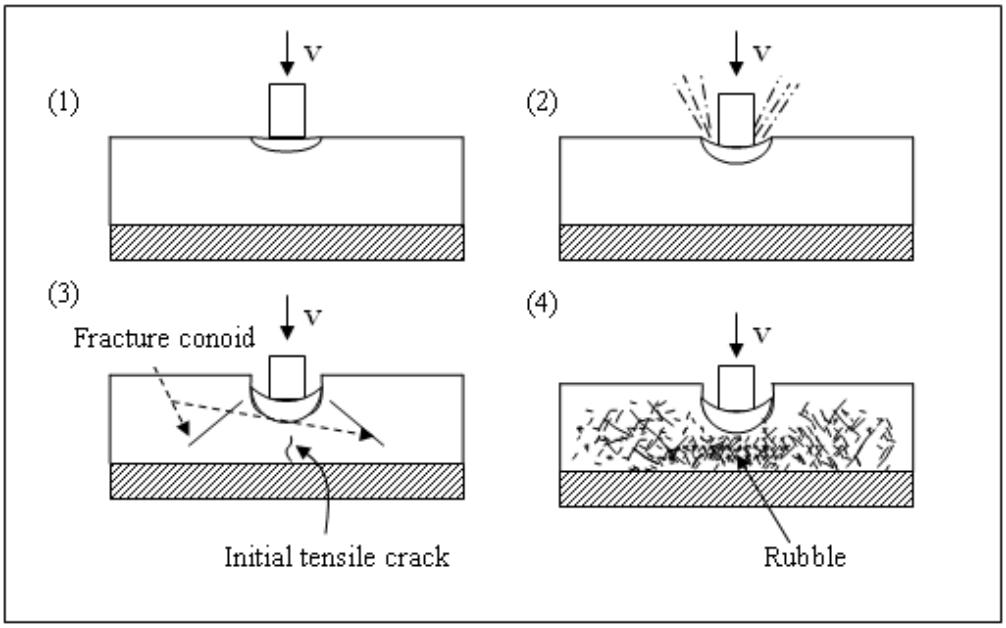

Fig. 2.4 Four stages of penetration into a ceramic armor. Adapted from [8]

ceramic, after which they are reflected back in the form of tensile or relief waves. When these relief waves reach the impact point, they relieve the confinement of the ceramic and hence, the compressive yield strength suddenly decreases. Due to this reduced strength, the projectile begins to penetrate the ceramic [39]. The initial damage originates at many points around the impact site. Coaxial cracks propagate from these points, forming a shallow cylinder [3]. Figure 2.5 gives a sketch of the loads present in the ceramic plate and the penetrator during the impact.

Combinations of the compressive waves and the tensile waves result in a cone of fracture surfaces and debris, known as the fracture conoid [39]. This conoid consists of cylindrical cracks which end at the rear plane of the armor [3].The conoid transfers the impact to the backing plate through its larger diameter at the interface, thus spreading the bullet impact over a much larger area than the bullet diameter [6].

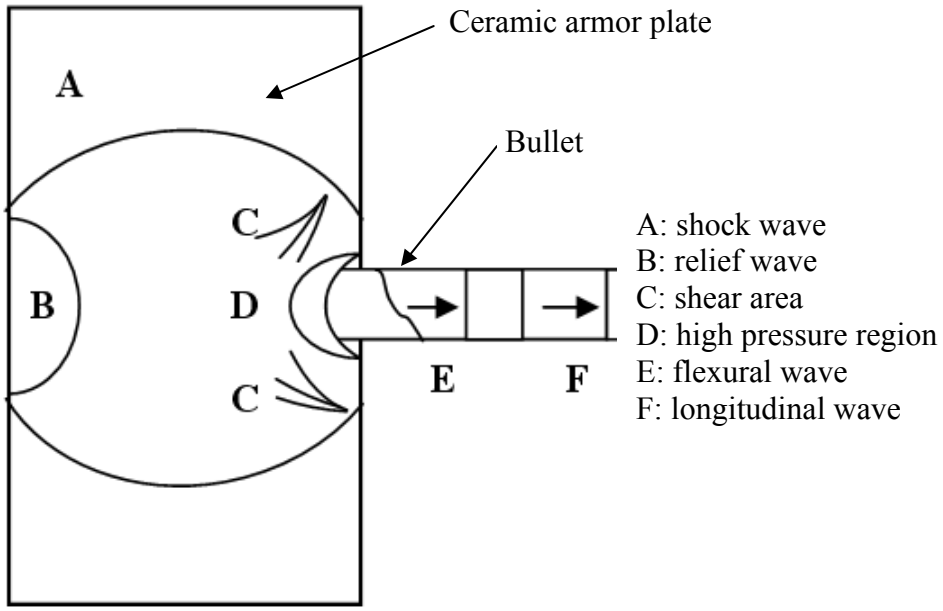

Fig. 2.5 Sketch of loads in a ceramic target and projectile during penetration

The tensile wave, reflected from the boundary or a free surface, causes the ceramic to break free of the adhesion and ejects the fragments [40]. Tensile cracking occurs at the interface between the backing material and the ceramic just after compressive shear damage [41]. Typically, the tensile failure strength of ceramics is relatively low, compared to the compressive strength. Apart from reflected tensile waves, local shear deformation or the bending loads can also cause tensile failure [1]. The ceramic will fracture at any point where the dynamic tensile yield strength is exceeded [3].

Thus, a tensile failure front moves from the back towards the point of impact. When this tensile fracture front meets the fracture conoid moving towards the rear, the conoid is complete and the remaining projectile and ceramic debris are pushed out [39]. Tensile and compressive fractures coexist during impact. A compressive wave travels through the backing plate as well [42]. As the fractured cone propagates, it causes lateral spread of ceramic fragments [2]. All these processes occur over a time frame of microseconds.

Radial tensile cracks are formed at the rear surface while star cracks form at the side of the conoids and tangential spall cracks occur due to reflection of stress waves from the edges of tile. Lateral cracks are a result of the reflection of longitudinal stress waves [22].

A small amount of comminuted ceramic is formed near the impact zone [3]. The total energy spent in fragmenting has been found to be quite low when compared to the kinetic energy of the projectile [40]. The different cracks formed in the ceramic plate lead to the formation of coarse chunks as well as fine powder [34]. Figure 2.6 shows the

Fig. 2.6 Fracture cone with lateral spread of fragments in a typical ceramic (boron carbide)

rear face of a ceramic plate fractured after ballistic impact. The fracture conoid and lateral spread of fragments can be seen.

Comminution and erosion of ceramic occurs in the cone area. The thickness of the ceramics affects the crack formation mechanism. More conoids are usually formed in thicker plates [22]. Once the ceramic fails, the strength depends on the confinement pressure and fragments can be displaced from the path of the penetrator easily [1].

2.2.1.4 Projectile Erosion

It is known that after the ballistic impact, compressive shock waves travel across the ceramic thickness semispherically and also backward through the projectile. The

shock waves travel through the materials at their respective sonic velocities. The more the difference between the sonic velocities of the projectile material and the ceramic, the stronger will be the shock wave impact, resulting in greater disintegration of the projectile [6].

For bullet velocities of about 3000 feet/s, the compressive pressure exerted can be up to 28000 MPa [2, 6]. Compressive strengths of ceramics typically increase with increasing confining pressures. Figure 2.7 shows an example of increasing compressive strength in alumina with increasing confining pressure. During the first few microseconds after the impact, the compressive strength of the ceramic plate increases which causes erosion of the projectile tip. The projectile flows radially outward and then in the backward direction. It has been postulated that in the first 9 μs after the impact, the projectile tip is destroyed and the backing plate starts to yield at the interface of the fracture conoid [6]. Projectile erosion and flattening continues with slight ceramic

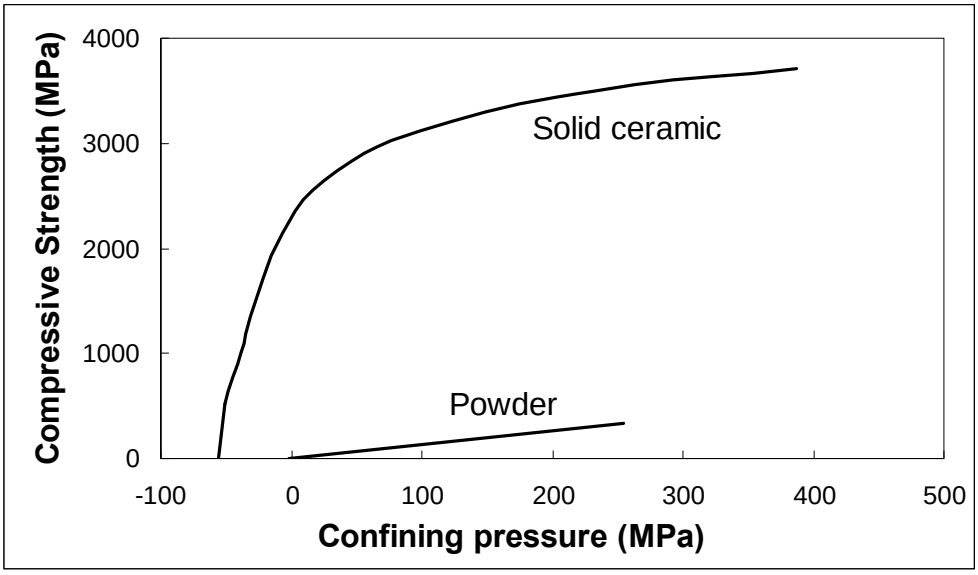

Fig. 2.7 Compressive strength vs. confining pressure for AD-85 alumina. Adapted from [39]

penetration following the formation of the fracture conoid [3]. This occurs over a time period of 9 μs to 15 μs after impact [6].

The energy consumed in projectile erosion has been found to be up to 12% of the total energy for a steel projectile (traveling at 1400 m/s) but it is less for lead bullets [40]. High hardness of a ceramic can help in disintegrating the projectile into fragments that can be absorbed by the flexible base [2].

2.2.1.5 Backing Plate Deformation

After about 15 μs, the ductile backing material absorbs the residual energy of the projectile by plastic deformation [2, 6]. This stage, which occurs over several milliseconds, determines whether the projectile is stopped effectively or if the armor is defeated. As the backing material deforms, projectile erosion products and the fragmented ceramic are ejected out of the impact area [3]. The nature and thickness of the backing material influence the fracture mechanisms because of its ability to reduce the stresses [22]. The energy dissipation by compressive shear fracture is one order of magnitude higher than that by tensile fracture; therefore, the backing material must be reinforced to compensate for the tensile weakness of the ceramic [41].

In an ideal scenario, the residual energy of the projectile is widely distributed and absorbed by the backing plate by dynamic deflection. Localized projectile loading is to be avoided because it can lead to stresses more than the shear strength of the backing material and cause a punch out and defeat of the armor system [6]. If the load is focused over too small an area, a thin backing plate can fail either by plug shearing or bending [18]. The ceramic and backing should preferably remain bonded after the impact. Hence, adhesive and bonding techniques must be optimized. The ceramic damage at impact

should be more conical than cylindrical. The hole in the damage area must be small. This is possible if the bullet speed decreases significantly after contact [22].

After the bullet impact, the armor system is damaged. In order for the armor system to provide protection against further attacks in the near vicinity of the first one, the damage zone has to be controlled. This ability of the armor is called the multihit capability. The cracks should be shorter with small cones while the remaining region should be largely unaffected to ensure multihit capability [22]. Using segmented ceramic tiles to make an armor system is one method to increase its multihit capability because it is difficult for the cracks to travel from one tile to another. Strong stress waves can, however, still travel from the edge on one tile to another and cause fracture. The lateral displacement of the tiles and the deformation of the backing plate can also crush the adjacent tiles. A continuous layer of elastomeric material placed around the tiles can help in attenuating the stress waves [43].

2.2.2 Ballistic Testing

Ballistic tests can be classified into the following categories: (1) phenomenological, (2) armor material characterization, and (3) armor design oriented.

2.2.2.1 Phenomenological Tests

These tests are carried out to determine material properties which affect the ballistic performance of a ceramic. These include indentation tests, four-point bending tests, and tensile and bar impact tests. They are not direct ballistic testing methods but they help in providing some picture of the material behavior under shock impact. Attempts have been made to correlate these properties with the ballistic performance of

the material but have not been very successful. Though these tests are nonballistic and do not involve armor configurations, they help in constructing models used in numerical simulations for design [1].

2.2.2.2 Armor Material Characterization Tests

Armor material characterization tests are used to directly measure material properties indicative of resistance to projectile penetration. They are further subdivided into traditional and nontraditional techniques. The traditional methods are the most commonly used techniques in ballistic testing. They include the following tests:

1. Semi-infinite Penetration Tests: The penetration vs. impact velocity curves are obtained and fitted with models. This gives an idea about the rate of erosion of the projectile and the ceramic's resistance to penetration.

2. Depth of Penetration (DOP) Tests: During the 1980s, this technique was developed by Woolsey *et al*. [44] in an effort to standardize a technique to rank ceramics for armor applications. Data from DOP tests are widely used to investigate a ceramic's ballistic efficiency. Figure 2.8 shows a typical setup for a DOP test. The front portion consists of the ceramic (of thickness t_c) to be tested and the rear portion is usually made of rolled homogeneous armor (RHA), a type of steel commonly used in the construction of armored vehicles. Some researchers have also used aluminum or GFRP composites as the backing material [42]. The rod penetrator after impacting the ceramic leaves a residual penetration into the RHA, $P_{r,}$ which is then accurately measured. This is the only quantitative parameter that can be obtained from these tests [45].

The residual penetration into the steel backing is measured as a function of the

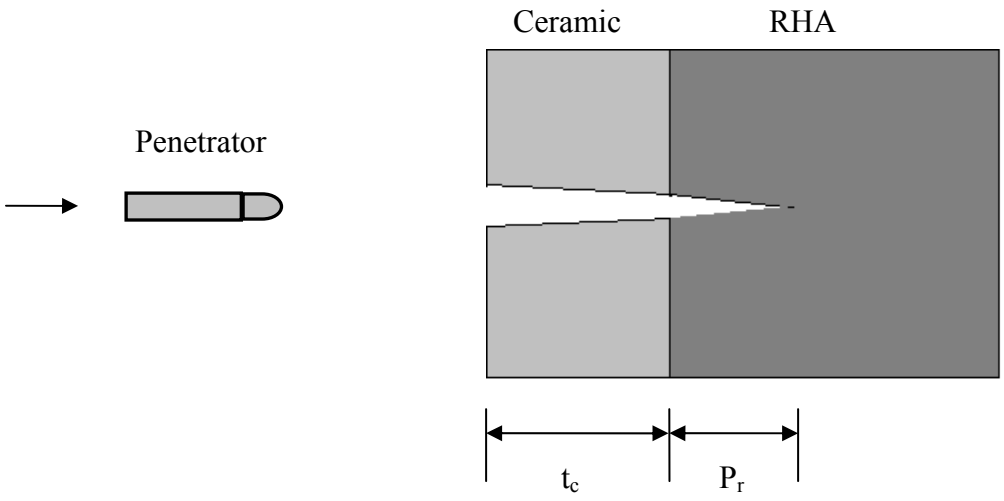

Fig. 2.8 A typical configuration of a depth of penetration (DOP) test

impact velocity and the ceramic thickness [8]. Assuming a thick backing, Rosenberg *et al*. [46] introduced a parameter, η, to measure the ballistic efficiency. It was defined as

$$\eta = \frac{\rho_b (P_b - P_r)}{\rho_c \, t_c} \tag{2.2}$$

where ρ_b, ρ_c are the densities of the backing and ceramic, respectively, t_c is the ceramic thickness, P_b is the depth of penetration in the backing without the ceramic and P_r is the residual penetration depth in the backing plate with the ceramic. As t_c is in the denominator, the efficiency is normalized with respect to thickness [47]. This parameter is also referred to as the differential efficiency factor (DEF). Analyses of many DOP tests [46, 48-50] reveal a linear increasing relation between the DEF and the thickness of the ceramic. In some cases like that

of SiC, as can be seen from Figure 2.9, the DEF can also decrease with increased thickness. This indicates that beyond a certain thickness, the projectile gets entirely defeated within the ceramic material and any further increase in the thickness would not be beneficial [43].

Though the DOP is the most popular ballistic testing method, its results are debated because the configuration is different from that of the actual armor used in real life situations. There are many variables like target configuration, penetrators, and presence or absence of cover plates which can influence the results to a large extent [1].

3. Dwell Tests: From experiments conducted by Hauver *et al*. [51], it was observed that when a penetrator entered a strongly confined ceramic target, it appeared to stall at the surface of the ceramic. During the first 10 μs after impact, the penetrator seemed to spread out radially at a 90 degree angle with respect to

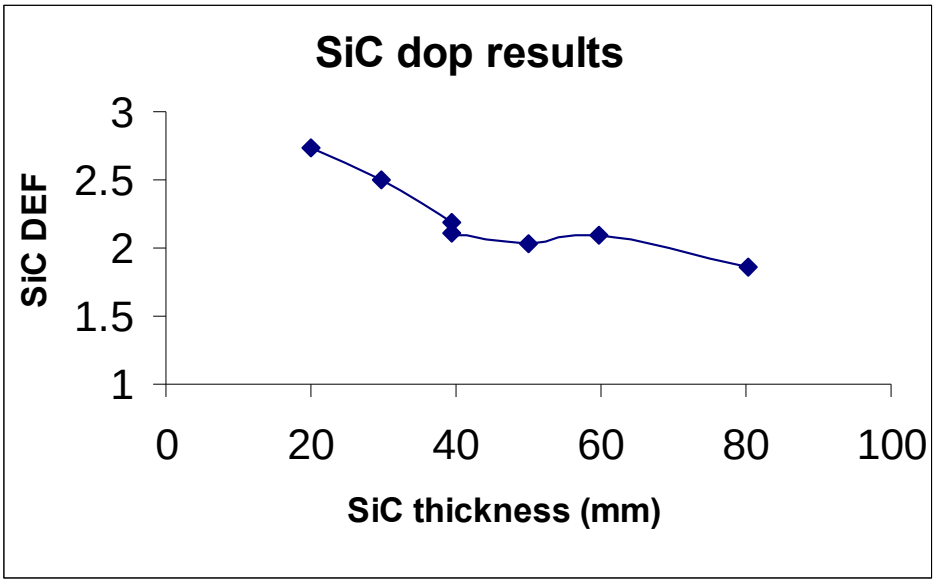

Fig. 2.9 Differential efficiency factor (DEF) vs. thickness for SiC plates. Adapted from [43]

the axis of penetration. This phenomenon is defined as dwell. The penetrator dwell is believed to be present in all ballistic impact experiments and thus has to be studied to interpret data, even from traditional ballistic experiments.

The theory of dwell states that a ceramic will resist penetration, until it fails in some manner due to many possible reasons, after which penetration will begin. In these experiments, in order to study dwell, there is erosion of the projectile with no penetration and hence, the impact velocities are not very high [1].

4. Dwell/Penetration Transition Tests: As the impact velocity is increased to a critical value, the surface stresses generated by the projectile exceed the compressive strength of the ceramic and further dwell is no longer possible, leading to penetration. This critical velocity, at which a transition occurs from interface defeat to normal penetration, is studied in the dwell/penetration transition tests [1].

Lundberg *et al*. [52] performed the dwell penetration tests on two types of SiC materials, TiB_2, and B_4C targets. Tungsten heavy alloy projectiles were used as the penetrators. Table 2.2 lists the range of critical velocities for the dwell/penetration transition obtained in those tests.

2.2.2.3 Armor Design Tests

Armor-design-oriented tests are used for direct evaluation of armor systems. They are the most important tests, yet the most difficult to carry out. They might require a lot of experiments to be conducted because of the probabilistic nature of the tests. The various types of tests in this category include the following:

Table 2.2 Dwell/penetration transition velocities for ceramic targets (data from [52])

Projectile/Target	**Transition velocity interval (m/s)**
WHA/SiC-1	1645-1705
WHA/SiC-2	1615-1715
WHA/TiB_2	1465-1545
WHA/B_4C	1430-1480

1. Fixed Target Geometry: This method is used to rank materials in a more realistic armor environment as it uses finite thicknesses**.** A finite armor plate is defined as one in which the free surfaces (side or rear) affect the depth of penetration. One example of such fixed target geometry tests is the 1-4-3 tests where the target configuration consists of a metallic cover plate of unit thickness, the ceramic plate of 4 times the unit thickness, and a metal backing plate with 3 times the unit thickness.

2. Tandem Composite Armor: Due to accumulative damage effects and pressure-dependent behavior of fragmented ceramic, thicker ceramic tiles do not generally perform as multiples of lesser thicknesses, making them expensive and less mass efficient. An alternative was developed by the Ballistics Research Laboratory and the Army Materials Research Laboratory [1] where the target configuration consisted of repeated sets of thin ceramic tiles backed with a metallic backing plate. The performance of this armor system approached the

multiplicative performance of each independent system and was superior to that of a single ceramic plate of an equivalent thickness.

3. Ballistic Limit Tests (VBL, V50, or VL tests): Ballistic limit can be regarded as the maximum velocity of a threat that can be countered effectively by a given amount of ceramic or conversely, the amount of material required to defeat a given velocity of the projectile. The V50 test has been widely accepted, especially for small fire arms threats. V50 is defined as the velocity at which the projectile has a 50% chance of complete penetration [53]. Its value is arrived at by bracketing it with higher and lower velocities, some of which defeat the material and some of which do not. This requires a minimum of five experiments out of which there should be at least two cases of partial penetration and two cases of complete penetration to determine the V50. The procedure is expensive and requires a large number of shots to reduce the scatter in the data.

In order to rank the armor ceramics at constant volume, on the basis of the ballistic limit velocity, the US Army Ballistic Research Laboratory arrived at a standard configuration. This consists of a 1/4/3 laminate of a 6.4 mm thick steel front plate, a 25.4 mm thick ceramic, and a 19.1 mm thick steel backing plate. Flash ray X-ray equipment is used to measure the penetrator velocity as a function of time accurately [8].

Among all the methods, the DOP and the V50 determination are the most widely accepted methods, especially for comparing the ballistic performances of different ceramic materials.

2.2.3 Ballistic Behavior of Common Armor Ceramics

As ceramic armor systems are quite expensive when compared to metallic armor, they are used only when their performance justifies their cost [8]. Many researchers have attempted to compare the relative ballistic efficiencies of ceramics like alumina, boron carbide, silicon carbide, and titanium diboride. It is difficult to analyze ballistic data for comparisons since there are many variables like the projectile material and geometry, the confinement method, thickness of the ceramic, the backing plate material and thickness, etc. We can only compare two materials tested under identical conditions [47]. There is no one best armor ceramic material. Each of the above mentioned ceramics has its own unique advantages and disadvantages [8]. We will assess the ballistic performance of the ceramics one by one followed by a relative comparison.

2.2.3.1 Alumina (Al_20_3)

Alumina tiles fabricated by Coors Ceramics were used as breast plates in body armor in the Vietnam War. Though they were heavy, they could stop the 0.30 caliber bullets fired from AK-47 rifles. To hold the fragments together for multihit performance, backing materials such as aluminum, fiber-reinforced plastic, and woven roving were used. Alumina is the major low cost ceramic material that has been used as hard face in the armor systems. The price of these tiles as of 1993 was $10-20 per kg. The typical thickness of the Al_2O_3 used in body armor is about 4-11 mm. For vehicle armor, it is up to 25 mm thick. The ceramic thickness required depends on the backing material and the threat. The commercial Alumina grades contain 92-99.7% Al_20_3 and have densities varying between 3.65-3.91 g/cc [54, 55].

Alumina ceramics are classified on the basis of their alumina content (*e.g.* 96, 97,

98, 98.5 wt % Al_20_3). The dominant crystalline phase in alumina ceramics is the α-Al_2O_3 (or corundum) and a glassy phase, usually silicate-based, is distributed uniformly between the grains. It has been observed that the hardness and the elastic modulus values increase with increasing amounts of corundum phase. Fine grain sizes and high purity levels are desirable from a ballistic point of view.

Medvedeski *et al*. [22] tested alumina ceramics (with Al_20_3 content 96, 97, 98, 98.5, and 99.6 wt %) bonded with aramid-based and fiberglass backing materials against 7.62 mm diameter projectiles. For single shot testing, 100 mm X 100 mm flat tiles with thicknesses between 7 and 15 mm were used. These systems were able to provide ballistic protection to level III, *i.e.*, they were able to defeat projectiles moving at up to 2750 feet/s. The ceramics with higher hardness values, (98.5 and 99.6 wt% α- Al_20_3) showed less trauma and less bullet intrusion, but the crack growth was more compared to other ceramics. The projectile erosion was also the highest for these higher purity materials. The crack propagation was not as severe in the alumina plates with higher amounts of glassy phase (97 and 98 wt% Al_20_3) when compared with the plates having higher percentages of alumina. Therefore, the former grades could be more useful for multihit applications. The 96 wt % alumina tiles showed the greatest trauma and fracturing although the system was not entirely defeated [55]. It was found that the ballistic performance of the tiles improved with the purity and hence, manufacturers have attempted to increase the purity levels.

Through a process known as ceramic armor process 3 (CAP-3), alumina consisting of very fine grains was manufactured by Coors. Researchers have manufactured 99.9% pure alumina, sintered to maximum density with the finest possible

microstructure [56]. The ballistic performance of this material was better than Coors CAP-3 alumina. Alumina ceramics are less brittle than other carbide-based ceramics, which can be an advantage for armor applications [34].

2.2.3.2 Boron Carbide (B_4C)

The first prototype of personnel armor for ground use was made of B_4C. Cold pressed armor pieces were loaded into susceptors and hot pressed at temperatures between 2150 and 2200º C and at a pressure of 1 ksi [6]. Its low density (~ 2.5 g/cc) coupled with its high hardness makes boron carbide an attractive armor material. The price of hot pressed boron carbide as of 1993 was about $150/kg [54].

The Hugonoit elastic limit (HEL) of B_4C is about 17-20 GPa. Its elastic behavior is retained at threat velocities up to 850 m/s which is more than twice the limiting velocities of SiC and Al_20_3. But B_4C fails catastrophically at dynamic pressures exceeding the Hugonoit limit unlike SiC and Al_20_3 which exhibit residual plastic behavior when stressed above the elastic limit. This phenomenon has not been completely explained [57]. One explanation offered is that B_4C exhibits amorphous phase transition above HEL which might account for the anomalous ballistic response at very high velocities imparting an impact pressure of more than 19 GPa. It is theorized that this amorphous phase might be formed due to the elastic modulus anisotropy in B_4C crystals and might cause an increased intergranular fracture under impact [58]. Chen *et al*. [59] suggested that the formation of nanoscale intragranular amorphous bands at higher pressures might be responsible for this phenomenon. The presence of these 2-3 nm wide amorphous bands, which could be induced due to the shock in well-defined lattice directions, was confirmed by transmission electron microscopy [53]. At lower contact

pressures, deformation is predominantly caused by the twinning mechanism. Amorphous and graphitic carbon inclusions that have been often observed in B_4C can also influence its deformation behavior under ballistic conditions [61].

2.2.3.3 Silicon Carbide (SiC)

SiC is the armor of choice for medium to heavy threats due to the amorphitization of B_4C at high pressures [62]. SiC became a good candidate material for use in armor when Prochazka [63] accomplished pressureless sintering of SiC with B and C additions. It has a density of about 3.2 g/cc and as of 1993, the price of reaction-bonded SiC was $35/kg whereas that of liquid-phase-sintered silicon carbide (LPSSC) was $80/kg [54]. The performance of SiC armor varies significantly depending on the microstructure. The failure surfaces usually show a lot of defects, such as carbonaceous particulates. The hot pressing of SiC involves two types of additives: (a) carbon and (b) metallic oxides, carbides or nitrides such as AlN, B_4C, Al_2O_3, etc. Carbon is used to remove the passivation layer of silica by vapor transport of CO and SiO gases into the pores prior to densification. If this layer is not removed, the microstructure would coarsen excessively, resulting in incomplete densification. The cationic additives may also form a liquid phase which aids in densification.

If the sintering additives are added in excess, they might lead to poor ballistic performance by initiating fracture [64]. Both B_4C and SiC have limited plastic slip systems and hence, there is no plastic flow at lower stress levels and the dynamic strengths are close to the theoretical strength. They have high HELs (15-20 GPa) but their postyield behaviors are different. B_4C has a higher HEL but subsequent deformation results in sudden loss of strength. SiC, on the other hand, has a HEL of 15-16 GPa and

the postyield strength remains unchanged or increases with subsequent deformation [65]. This strengthening effect in SiC provides comparable strength with more ductility than B_4C [66].

2.2.3.4 Titanium Diboride (TiB_2)

Because of its high flexural strength and elastic modulus values, TiB_2 shows ballistic performance that is comparable to B_4C and SiC [67]. But its ballistic efficiency, owing to its higher density, is lower than that of SiC or B_4C. This is because, as seen from Equation 2.2, the differential efficiency factor is inversely proportional to the density of the ceramic. For ballistic protection, TiB_2 is used more widely in composite ceramic systems, such as Al_20_3-TiB_2 or SiC-TiB_2, than as monolithic TiB_2. The ballistic efficiency of certain Al_20_3-TiB_2 systems with optimized microstructures has approached that of monolithic TiB_2 systems [68]. Functionally graded material (FGM) systems of TiB_2 can also be used for armor applications. A FGM can be considered as a stack of layers, each layer having a different composition and hence, different mechanical properties. In the FGMs used in armor applications, the compositions of the ceramic and the metallic constituents are varied gradually from one end to the other in the thickness direction. The ceramic on one side provides high protection while the metal on the other end offers ductility. In Ti-TiB_2 FGMs, fine TiB whiskers are produced in situ in the intermediate composition layers. These whiskers improve the ballistic properties of the material. Spark plasma sintered FGMs with Ti content varying between 1 wt% and 10 wt % showed better ballistic performance than hot-isostatically-pressed TiB_2 inserts [69].

2.2.4 Relative Comparison of Ballistic Performances

Several researchers have carried out ballistic tests on the above-mentioned ceramics under identical conditions to compare their ballistic performances.

O'Donnell *et al*. [70] performed impact tests on SiC, B_4C, Al_2O_3, and TiB_2 tiles bonded to 2024 T351 aluminum alloy plates with 0.30 caliber conical nose shaped steel projectiles. The surface area of the fragments generated was computed. It was found that boron carbide had the maximum fragment surface area while SiC had the least. TiB_2 caused the greatest erosion in the penetrator. It eroded about 59% of the initial projectile mass whereas alumina eroded the least mass.

Alumina, SiC, B_4C, and TiB_2 tiles backed with thick steel plates were impacted with tungsten cylinders shot at velocities between 1.35 and 2.65 km/s by Reaugh *et al*. [67]. The residual penetration into the steel was measured to quantify the ballistic performance. TiB_2, B_4C, and SiC showed almost similar residual penetration depths whereas alumina's performance was poorer.

A depth of penetration study was conducted by Kaufmann *et al*. [3] to evaluate the performance of Ceramor alumina, Hexoloy silicon carbide, and Ceralloy 5460 boron carbide when impacted by a 12.7 mm (0.50 caliber) AP projectile. 6061 T6 aluminum cylinders (6" diameter and 6" long) were used as the backing material and the depth of penetration method was used to quantify the ballistic performance of the materials. It was determined that silicon carbide had the best ballistic performance at the range of velocities tested. However, in many cases, the performances of B_4C and SiC were similar. Alumina was outperformed by SiC and B_4C. For an impact velocity of 750 m/s, the SiC tiles showed the least penetration depth while at impact velocities of 850 and 910

m/s, SiC and B_4C had similar DOPs which were five times less than that of alumina tiles. The ballistic efficiencies of SiC and B_4C increased as the projectile velocity increased.

Moynihan *et al*. [71] conducted ballistic tests against Coors 94% pure Al_2O_3, Cercom SiC, and Cercom B_4C targets of various thicknesses to determine the minimum thickness for each material required to completely defeat the armor piercing 0.3 caliber steel core projectiles. The impact velocity was maintained at 841 $\pm$ 15 m/s and a 3" thick aluminum plate was used as the backing. The projectile was entirely defeated within the ceramic for 5.1 mm thick B_4C and SiC tiles and 6.3 mm thick Al_2O_3 tile. The residual penetration areal density, which is defined as the density of aluminum backing times the DOP (ρ_{Al} P_r), was plotted against the ceramic areal density (ρ_c t_c) for the three ceramics (Figure 2.10). For similar DOP values, a ceramic having a lower areal density would be preferred as it would be lighter or thinner. We can see that B_4C is the most effective while Al_20_3 is the least effective armor material.

50 mm thick alumina and TiB_2 targets with 6.5 mm cover steel plates were impacted by tungsten rod projectiles (9.80 mm diameter, 14:1 aspect ratio) by Bourne *et al*. [47]. The velocities of the tungsten rods were 1345 m/s and 1340 m/s, respectively. The depth of penetration on the backing plate was observed to be 25.5 mm for the TiB_2 and 53.8 mm for alumina.

Roberson *et al*. [72] fired 7.62 X 51 mm (7.62 mm bullet diameter and 51 mm case length) tungsten carbide core (with copper gliding jacket) projectiles at TiB_2 (hot pressed Ceralloy 225), B_4C (hot pressed Ceralloy 546-3E), and SiC (hot pressed Ceralloy146-1S). The DOP into aluminum alloy backing block was measured. The

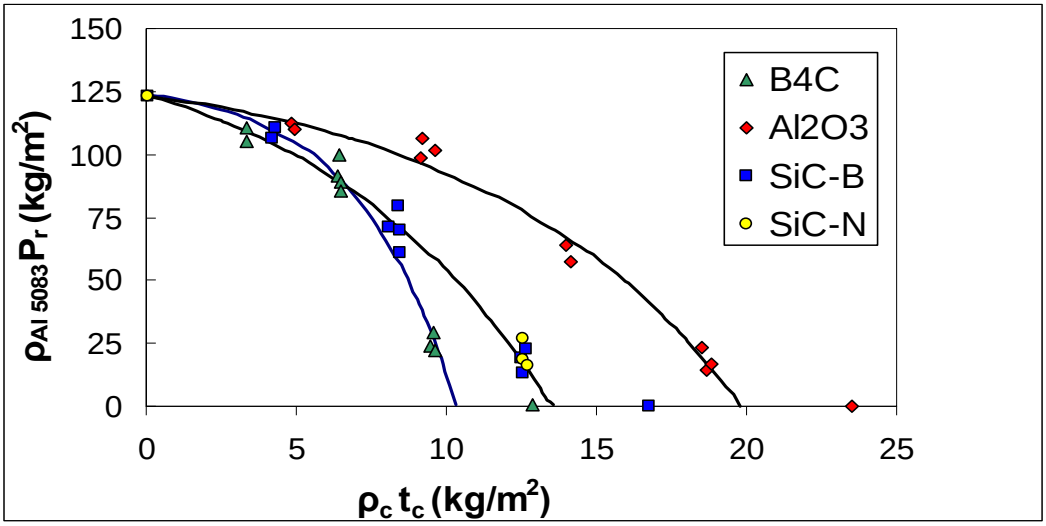

Fig. 2.10 Residual penetration areal density vs. ceramic areal density plots for B_4C, Al_20_3, Cercom SiC-B, and Cercom SiC-N. Adapted from [71]

critical thickness of the ceramic for which there would be no residual penetration was arrived at by extrapolating the residual penetration vs. the thickness curve. These critical thicknesses were found to be 8 mm, 10.5 mm, and 8.5 mm for TiB_2, B_4C, and SiC, respectively. TiB_2 had the lowest critical thickness, but SiC and B_4C outperformed TiB_2 on a weight-by-weight basis. The areal densities of B_4C and SiC were similar even though B_4C has a lower density and higher hardness value.

Vyshnyakov *et al*. [73] suspended plates of SiC, TiB_2, and Al_2O_3 (fabricated by different routes) from a pendulum and then released them to hit an obstacle. A ballistic parameter, I_s' was defined as

$$I_s' = \frac{I_s}{\rho_c \, S_c} \tag{2.3}$$

where ρ_c and S_c are the density and the thickness, respectively, of the ceramic and I_s=

I_{br}/I_0 with I_{br} being the breakdown momentum, *i.e.*, the momentum absorbed in passing through the obstacle and I_0 the initial momentum of the pendulum. B_4C showed the maximum breakdown resistance followed by SiC and TiB_2. Al_2O_3 displayed the least resistance to breakdown.

Therefore, in conclusion, we can say that the ranking of these ceramics could be (1) B_4C (2) SiC (3) TiB_2 (4) Al_2O_3 with B_4C and SiC showing similar ballistic performances and TiB_2 losing out due to its higher density. In all the tests, alumina showed the poorest performance.

2.3 Titanium Boride (TiB)

Titanium monoboride (TiB) is an intermediate compound formed between Ti and TiB_2. From the past research in our group, it has been found that TiB possesses attractive mechanical properties such as high hardness and high elastic modulus [74]. Panda *et al*. [74] and Sahay *et al*. [75] have fabricated Ti-TiB composites consisting of fine TiB whiskers in Titanium matrix. Fully dense and nearly monolithic TiB with less than 5% of residual β-titanium has been synthesized by Madtha *et al*. [10].

2.3.1 Ti-B Phase Diagram

As can be seen from the titanium-boron phase diagram (Figure 2.11), TiB, Ti_3B_4, and TiB_2 are the three compounds formed at 18-18.5 wt% B, 22.4 wt %, and 30.1-31.1 wt % boron, respectively. Figure 2.12 shows how in both TiB_2 and TiB, the trigonal prism is the fundamental building block. In TiB_2, the prisms are stacked one over the other with each prism sharing all three rectangular faces with its neighboring prisms, thus making a hexagonal structure. In TiB, the prisms are packed such that the rectangular faces of

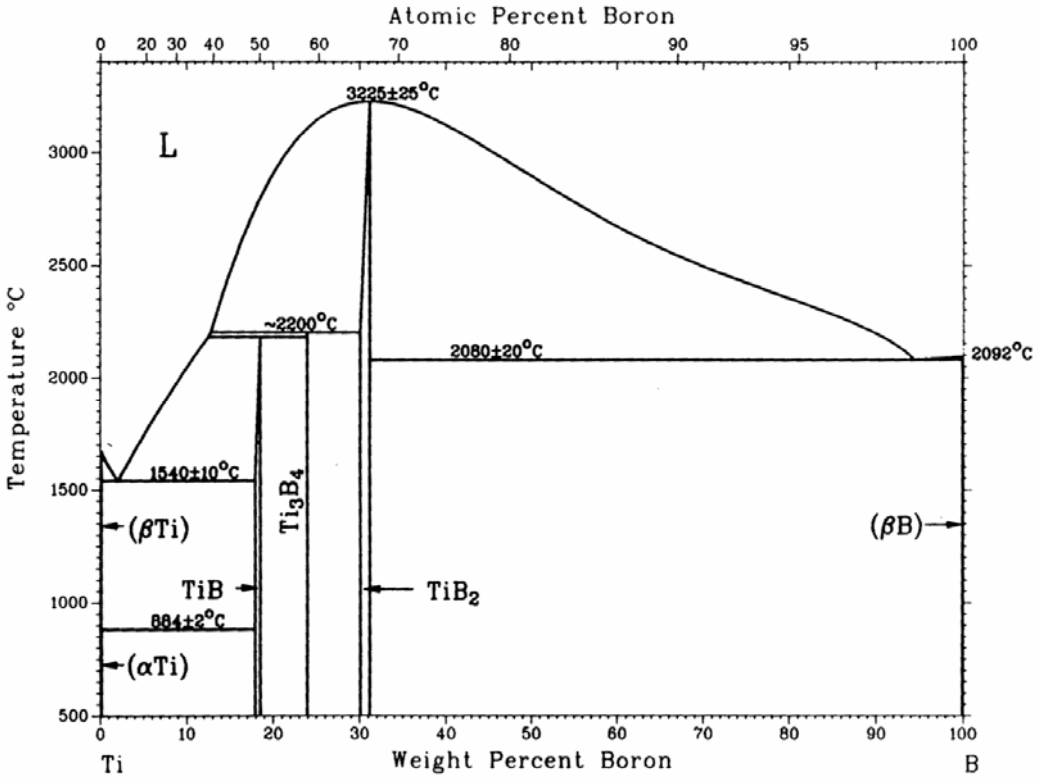

Fig. 2.11 Titanium - boron phase diagram. Adapted from [76]

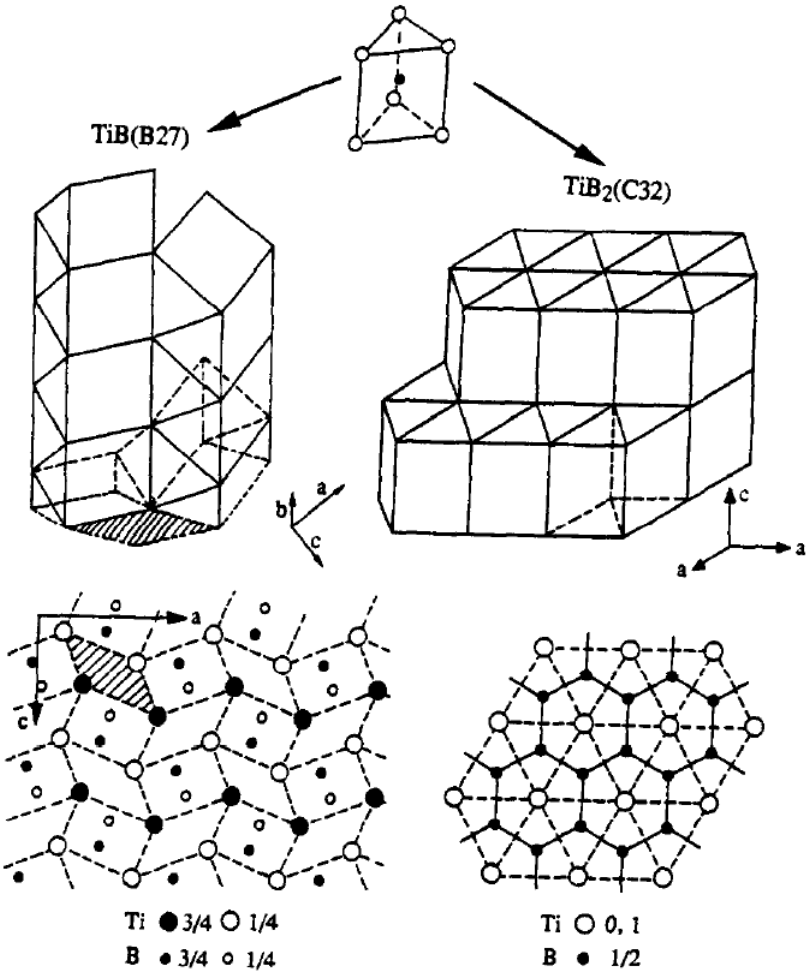

Fig. 2.12 Unit cells of TiB_2 and TiB. Adapted from [77, 78]

neighboring prisms are in contact with the TiB prisms oriented horizontally.

The boron atoms form a zig zag chain along the [010] direction. The boron atoms diffuse preferentially along this direction and hence, the growth of TiB is in the form of whiskers. The growth of high aspect ratio TiB whiskers can lead to improved stiffness, strength, and creep resistance in metal matrix composites. While TiB_2 is known to form particulates or plates, there has not been much evidence of intermediate Ti_3B_4 having formed during reactions between Ti and TiB_2 powders during hot pressing [10].

2.3.2 Synthesis of TiB by Reaction Sintering

Panda *et al*. [74] and Sahay *et al*. [75] fabricated Ti-TiB composites by carrying out reaction sintering of Ti and TiB_2 powders. TiB whiskers of varying volume fractions were obtained in situ in titanium matrix. Madtha *et al*. [10] synthesized nearly monolithic TiB by the same process which involved hot pressing Ti and TiB_2 powders under inert gas atmosphere of argon at a temperature of 1340°C and at a pressure of about 10-15 MPa.

When the overall boron content is less than 18 wt%, a composite of Ti-TiB with TiB whiskers in a continuous titanium matrix is formed. In solidification processing, when a liquid melt containing the appropriate boron content is solidified, the resulting microstructure consists of titanium matrix with TiB phase separating out through a peritectic reaction. But the TiB thus formed has been found to be relatively coarse and contains internal porosity [79, 80]. The other method is by solid state reaction of Ti and B or Ti and TiB_2 powders, *i.e.*,

$$Ti + B = TiB \tag{2.4}$$

$$Ti + TiB_2 = 2\ TiB \tag{2.5}$$

The first reaction is highly exothermic. Figure 2.13 shows that the second reaction is thermodynamically favorable as the change in the free energy for higher temperatures is slightly negative. As can be seen, the formation of TiB_2 has a more negative free energy than that of TiB and hence, when we mix Ti and B powders, TiB_2 would be formed preferentially. The free energy for the second reaction, however, is slightly negative. Therefore, it is possible to obtain a microstructure of TiB with Ti without

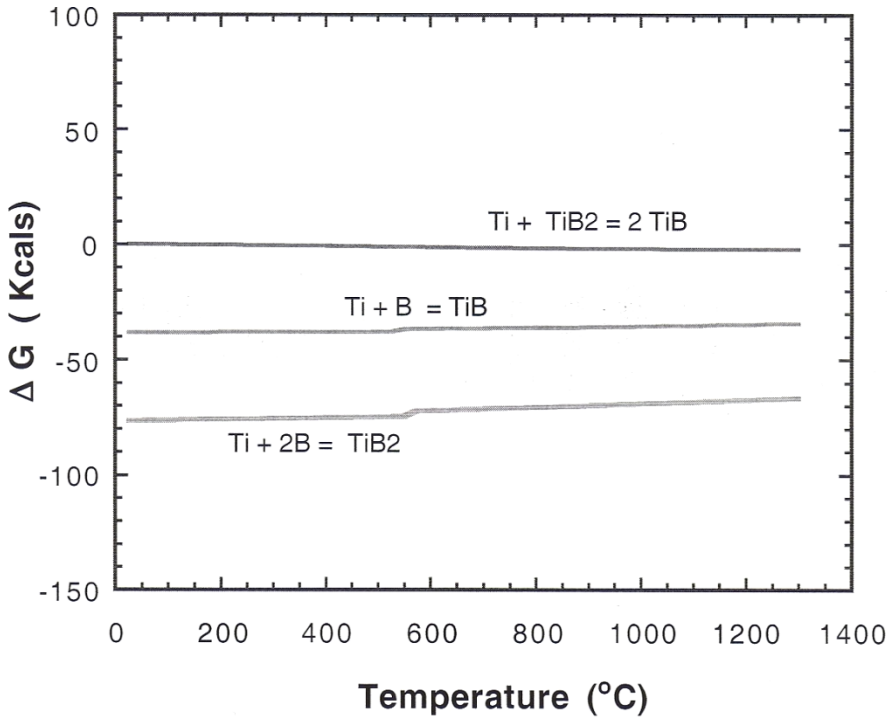

Fig. 2.13 Free energy diagram for TiB, TiB_2 formation

getting TiB_2 if the powders are mixed in the appropriate proportions.

In our research group [75], Ti-TiB composites were fabricated by simultaneous synthesis and densification. On the basis of equation 2.5, the basic reaction for forming different volume fractions of TiB in titanium matrix can be written as:

$$a\ Ti + b\ TiB_2 = x\ Ti + y\ TiB \qquad (2.6)$$

where a, b are the moles of the starting Ti and TiB_2 powders, respectively, and x, y the moles of Ti and TiB obtained after the sintering. Different volume fractions of TiB can be synthesized by varying a and b.

2.3.3 Ti-TiB Composite Systems

Sahay *et al*. [75] noted that as the TiB whisker volume fraction was increased in the Ti-TiB composites, the microstructure consisted of a network of interconnected and finer TiB whiskers as opposed to large TiB whiskers in Ti-rich composites. This is because for higher volume fractions of TiB whiskers, the growth of the whiskers is limited due to space constraints. Also, the increase in the number of nucleation sites for TiB would lead to finer whiskers, as demonstrated in Figure 2.14.

Some of the earlier synthesized composites with higher amounts of TiB_2 powders in the initial mixture were found to have up to 6% unreacted TiB_2. This was believed to be a result of reduced direct contact between TiB_2 and Ti particles which limited the diffusion of boron from TiB_2 to Ti [81, 82]. The powder sizes and the weight fractions

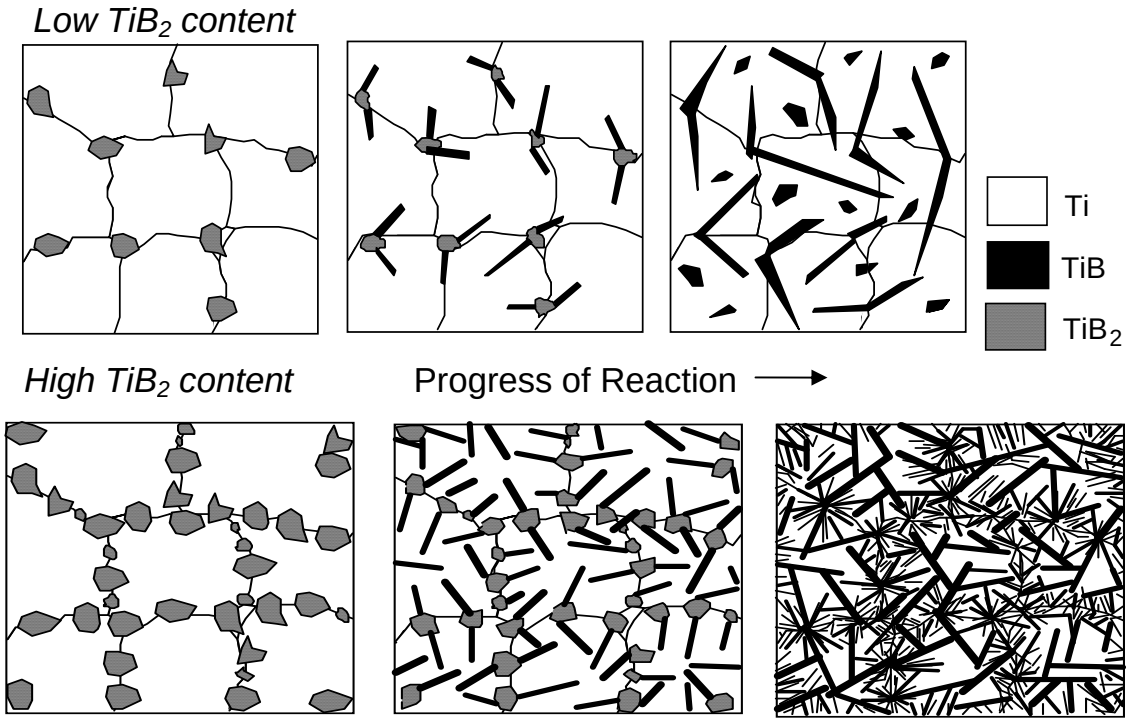

Fig. 2.14 Differences between the development of TiB morphology in systems with low and high initial TiB_2 content. Adapted from [75]

were further optimized [10] leading to TiB-Ti composites with up to 95 % TiB reinforcements. The Ti, TiB_2, and the sintering agent (Fe-Mo powders) were mixed in a trimodal packing arrangement to get homogeneous microstructure and negligible unreacted TiB_2. Figure 2.15 shows the schematic of the sintering process. Fe-Mo particles act as stabilizers of the β phase titanium. In the presence of Fe-Mo, a liquid phase forms with titanium which aids the sintering process. Boron diffuses from the TiB_2 particles through the liquid phase to the Ti-rich regions, leading to the formation of a network of TiB whiskers.

2.3.4 Monolithic Titanium Boride

An approach to synthesize nearly 100% monolithic TiB was developed in earlier research [10] in our group. The approach is described here briefly.

Ti powder, 99.95 % pure, with particle size < 44 μm (supplied by Alfa Aesar,

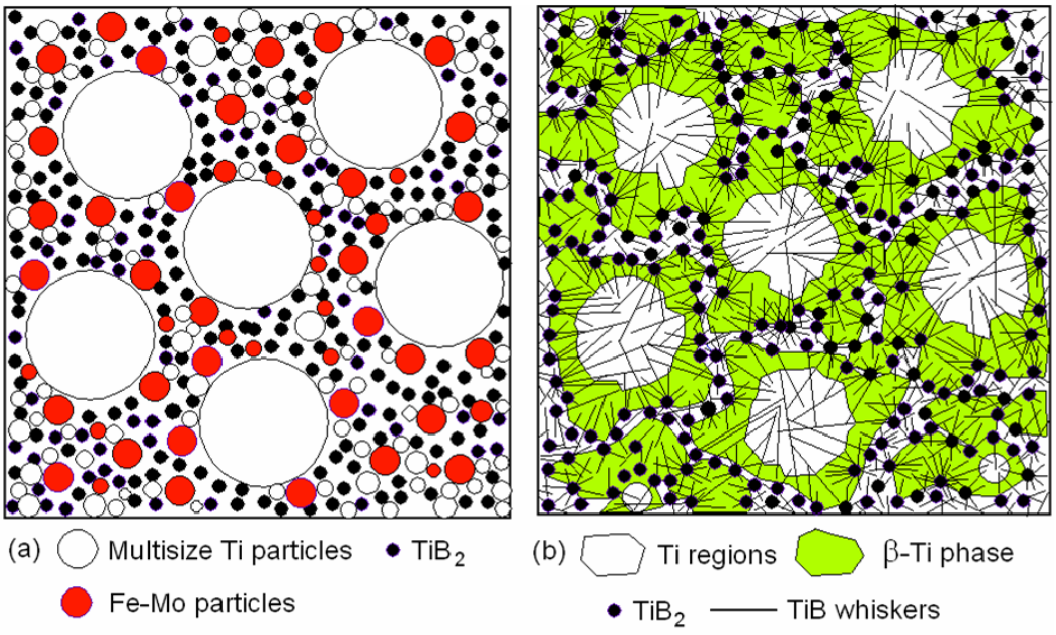

Fig. 2.15 Sintering process of Ti, TiB_2, and Fe-Mo powders

Ward Hill, MA) and TiB_2 powders, > 98.8 % pure, with an average particle size of 10 µm (supplied by Atlantic Equipment Engineers, Bergenfield, NJ) were used in the sintering process. Sintering agents were added in calculated quantities. The powders were cold blended for 16 hours in a tumbling mill. The mixture was then transferred to a graphite die and hot pressed at 1340° C under a pressure of about 10-15 MPa in argon atmosphere for 2 hours. TiB compacts with dimensions 75 x 75 x 12 mm were prepared. After further optimization of the powder mixture composition, nearly 100% monolithic TiB was synthesized [10]. This was obtained for an initial powder mixture composition of 47.4, 48, and 4.5 wt% of Ti, TiB_2, and Fe-Mo powders, respectively.

The hardness, fracture toughness, and flexural strength of this material were measured [10]. SEM micrographs of the material (Figures 2.16 (a) and (b)) revealed that clusters of nanostructured TiB whiskers formed a nearly 100% monolithic TiB matrix. Some amount of titanium was entrapped within the dense whisker network. The small dark regions in the micrographs could be attributed to the dissolution of pockets of the titanium matrix by the etching reagent used. The trapped titanium, which is not available

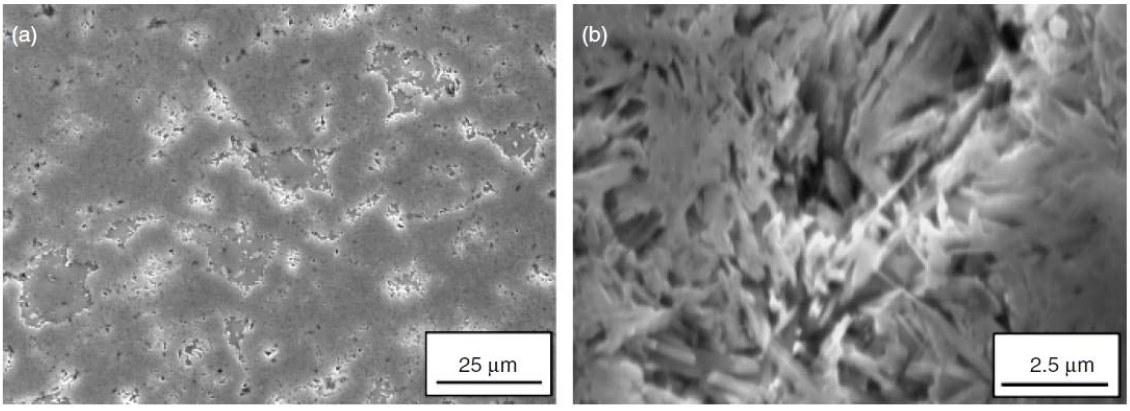

Fig. 2.16 Scanning electron micrographs of nearly monolithic TiB material at (a) low and (b) high magnifications. Adapted from [10]

for reaction, is referred to as the residual titanium. In X-ray diffraction patterns, no peaks were found for either Ti_3B_4 or TiB_2; therefore, it can be concluded that there was no interfacial phase and also that the reaction has been driven to completion. The intensity peak ratios of (111) TiB to (110) Ti were found to be very small when compared with the ratios obtained in the previously synthesized Ti-TiB composites. The amount of residual Ti was calculated to be less than 5% [10].

The physical and mechanical properties of the monolithic TiB were investigated and are presented in Table 2.3. If we compare these properties with those of the other ballistic ceramics given in Table 2.1, we can see that TiB has one of the highest fracture toughness and flexural strength values while possessing reasonable hardness and elastic modulus values. These properties make it an attractive candidate for armor applications. The aim of this research is to carry out ballistic testing of these monolithic TiB plates.

Table 2.3 A compilation of properties of TiB. Adapted from [10]

Property	**TiB (our work)**	**TiB (work by others)**	**TiB_2**	**Cerbec NBD 200 Si_3N_4**
Density (g/cc)	4.6	4.54	4.50	3.16
Hardness (VHN)	1860 ± 38 at 98 N	1900 at 98 N	2200 ±200 at 5.65 N	1550 at 98 N
Polycrystal elastic modulus (GPa)	427	450	565	320
Polycrystal shear modulus (GPa)	185	-	249	-
Fracture toughness ($MPa.m^{1/2}$)	5.46 ±0.28 at 196 N	4.5 at 98 N	6.2	5.5
Three-point flexure strength (MPa)	782 ± 33	360	308 ± 20	900

CHAPTER 3

EXPERIMENTAL PROCEDURE

3.1 Ballistic Testing

3.1.1 Ballistic Setup

A lab-scale setup for the ballistic testing of metal plates was constructed by Wyatt [83]. The basic design of the testing unit consists of a rifle mounted at one end and an isolated test chamber at the other to contain all the debris flying from the sample after firing. The setup is composed of two parts: (a) the ballistic cage consisting of the rifle with a chronograph in front of it and (b) the test chamber containing the mounted target sample. It is illustrated in Figures 3.1 and 3.2.

The cage was made from Lexan sheets held together by unistruts. The test chamber was constructed with the help of 50 mm thick compressed rubber pads bolted to steel angles running on the outside. The whole structure was approximately 10 feet long, 2 feet wide, and 3 feet tall.

For the ballistic testing, the rifle (a Remington 700 bolt action, 0.308" caliber civilian rifle) was mounted on a rest pad and fastened with the help of velcro straps, as can be seen from Figure 3.3. A chronograph was placed in front of the rifle in order to record the bullet velocity. It consists of two infra red sensors 18" apart with shadow screens placed over each of them. Two electric lamps were placed on the Lexan sheet

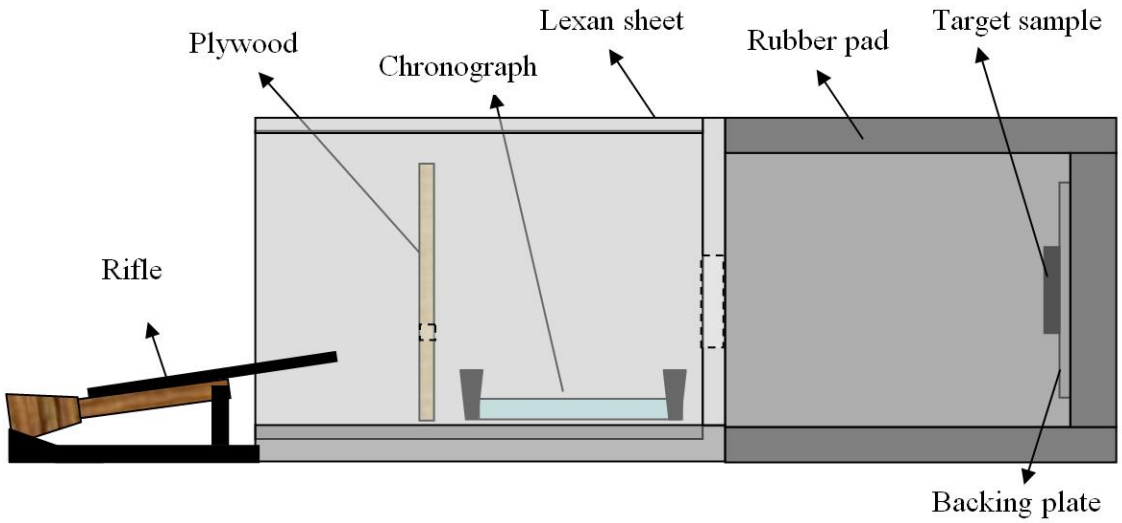

Fig. 3.1 Schematic of the ballistic testing setup

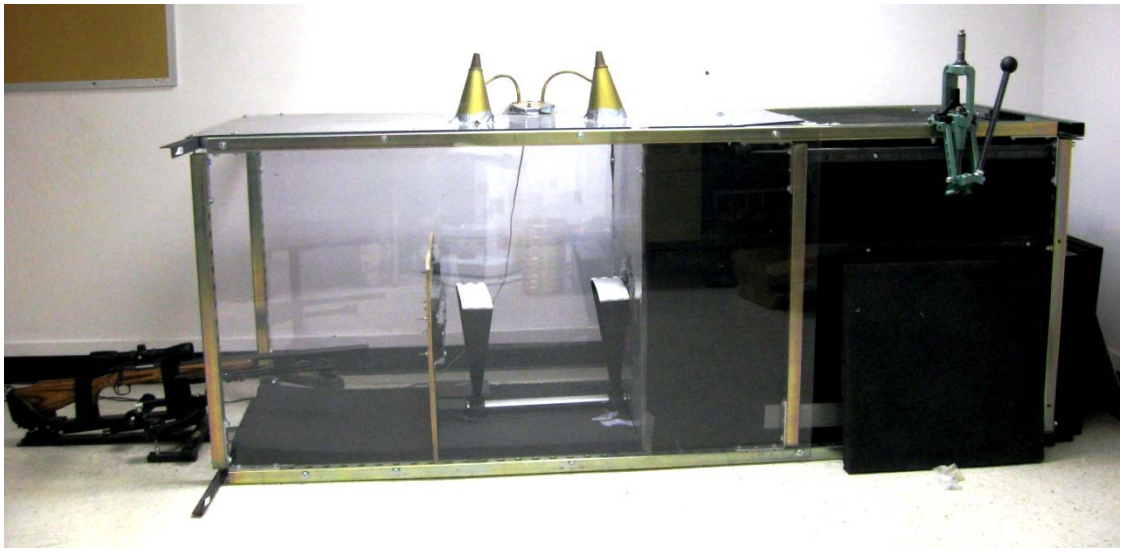

Fig. 3.2 Ballistic setup

Fig. 3.3 Rifle mounted on a rest pad

above the screens in order to enhance the contrast. A plywood sheet (with a hole in the middle to allow the bullet to pass through) was placed in between the rifle and the chronograph to protect the sensors from the muzzle blast emitted from the rifle (Figure 3.4). To prevent the shrapnel from coming back into the firing chamber and damaging the chronograph, a Lexan sheet, with a hole, was fixed behind the chronograph. This sheet separated the test chamber from the cage.

The test chamber was made from 50 mm thick compressed rubber pads on three sides supported by sections of steel beams running on the outside. On the rubber pad facing the gun, a 450 mm x 450 mm x 12.7 mm backing plate was attached. Stainless steel was used as the backing material for the first set of experiments; thereafter, it was replaced by aluminum to reduce the rigidity of the backing plate. Figure 3.5 shows the inside view of the test chamber with the backing plate onto which the target samples were mounted. An extra rubber pad was placed behind the chamber to absorb the residual bullet energy in the event of complete penetration of the backing plate and the rubber behind it.

Fig. 3.4 Shooting chamber

Fig. 3.5 Inside view of the test chamber with aluminum backing

3.1.2 Reloading

Figure 3.6 shows the schematic of a simple bullet assembly. It consists of a primer, a cartridge, gunpowder, and the bullet. A primer is an explosive material pressed onto the bottom of the brass cartridge. The cartridge is filled with an amount of gunpowder and the bullet is crimped into the cartridge. The bullet used in this project was a full metal jacket bullet which consists of a soft lead inner core with a copper jacket outside. The entire bullet assembly is placed in the rifle chamber. When the trigger of the rifle is pulled, a hammer strikes the primer which ignites the gunpowder within the cartridge. This explosion leads to the release of rapidly expanding gases which causes the ejection of the bullet at high velocities. The cartridge stays in the chamber and is ejected when the rifle chamber is unbolted.

The reloading procedure in this project involved the following components: Hornady 0.308" caliber brass cartridge, CCI large rifle bench rest primer, Alliant 15 Reloader gunpowder, and a Winchester 147 grains full metal jacket bullet. “Grain” is a commonly used unit in ballistics and 1 grain is about 0.0648 grams. The steps that were

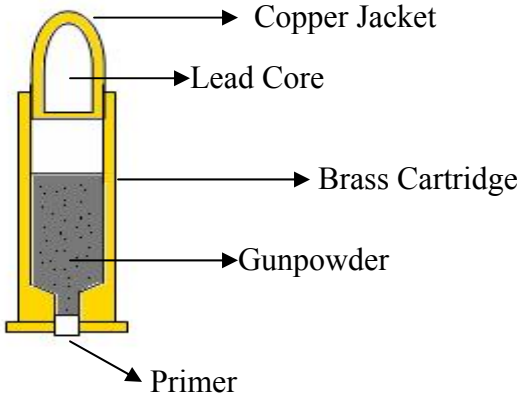

Fig. 3.6 Components of a bullet

followed during reloading were:

1. The primer was seated in the primer holder, anvil side up. A new cartridge was kept in the shell holder and then the press arm was raised to fully seat the primer onto the case until it is flush.

2. The required load of gunpowder to be used was poured in a cup using the powder dispenser and then into the cartridge, as shown in Figures 3.7 and 3.8.

3. The filled cartridge was kept on the case holder and the bullet was placed over its mouth. By lowering the press ram, the bullet was pressed into the case (Figure 3.9) till about half the crimping marks of the bullet were visible. Roughly the same overall length was maintained for all the bullets.

Fig. 3.7 Powder dispenser to get the required gunpowder load

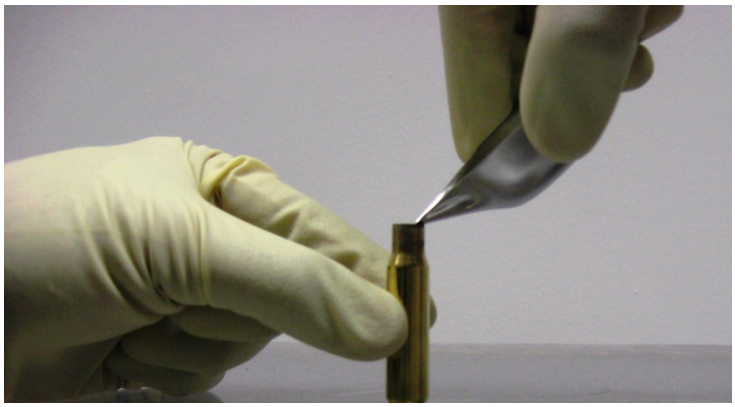

Fig. 3.8 Pouring the gunpowder into the cartridge

Fig. 3.9 Crimping the bullet onto the cartridge

3.1.3 Shooting Procedure

The rifle was secured on the rest pad using velcro straps. The target point was set by adjusting the knobs on either side of the rest pad and checking the crosshairs on the scope. The crosshairs were fixed to the left of and above the intended target point since it was observed that after firing, the bullet drifted toward the right. The plywood sheet was placed in front of the rifle such that its hole was aligned directly in the line of fire.

The test sample was mounted on a stand fixed onto the backing plate. The sample was secured by duct tape. The testing chamber was completely closed by placing the remaining piece of rubber sheet over the structure and the gaps were sealed using duct tape. After the bullet was fired, the bullet velocity was read from the values in the chronograph.

During some of the initial trials, it was observed that the chronograph did not record the bullet velocity. This problem, which was caused by insufficient lighting, was solved by placing two electric lamps over the chronograph shadow screens to increase the contrast when the bullet passed over the screens. The chronograph was placed at the same position for all trials to increase the accuracy of the velocity readings. The impacted plate and all debris including the bullet fragments were collected and labeled.

3.2 Shooting Mild Steel Plates

In the initial experiments, hot rolled A36 mild steel plates were shot with bullets having different gunpowder loads and hence, different velocities. Three batches of plates (with thicknesses 9.5, 15.9, and 19.1 mm) were tested. The gunpowder load was varied from 38 grains to 43 grains as per the manufacturer's recommendations.

A stage was attached to the backing plate by screws and the test samples were

secured in it using tape. The initial set of samples (9.5 mm thick) was shot using the stainless steel backing plate configuration by Wyatt [83]. Then, the backing plate material was changed to aluminum to investigate the role of the backing. The aluminum backing would allow the test sample to deform more as aluminum is softer than stainless steel. With the aluminum backing plate, three sets of plates of different thicknesses were tested against bullets fired at velocities between 716 and 823 m/s.

All the samples showed a crater in the front surface and a bulge at the rear. For the plates, the depth of the crater from the plate surface to the bottom of the crater was measured using a Vernier caliper. The crater volume was also measured by filling it with glycerol (of known density) and measuring its weight.

3.3 Ballistic Testing of Ceramics

3.3.1 Modified Setup for Ceramics

To avoid the influence of the backing plate on the ballistic performance of ceramics, a setup was designed in which two mild steel plates (200 mm x 150 mm x 6.3 mm and 200 mm x 150 mm x 19 mm) with rectangular cutouts in the center were bolted to the steel backing plate. To get an indication of the residual kinetic energy of the bullet after defeating the ceramic, a 6061 T6 Al plate, 100 mm long, 100 mm wide, and 6.3 mm thick, was glued to the ceramic plate. Then this ceramic-aluminum plate assembly was sandwiched between the two mild steel plates with cutouts. The cutout on the rear mild steel plate allows the aluminum plate to deform freely up to a distance of 25 mm without any interference from the bigger backing plate.

Figures 3.10 and 3.11 show the modified setup for testing ceramics. For trial purposes, plates of B_4C (100 mm x 100 mm x 6.3 mm) were shot with bullets having

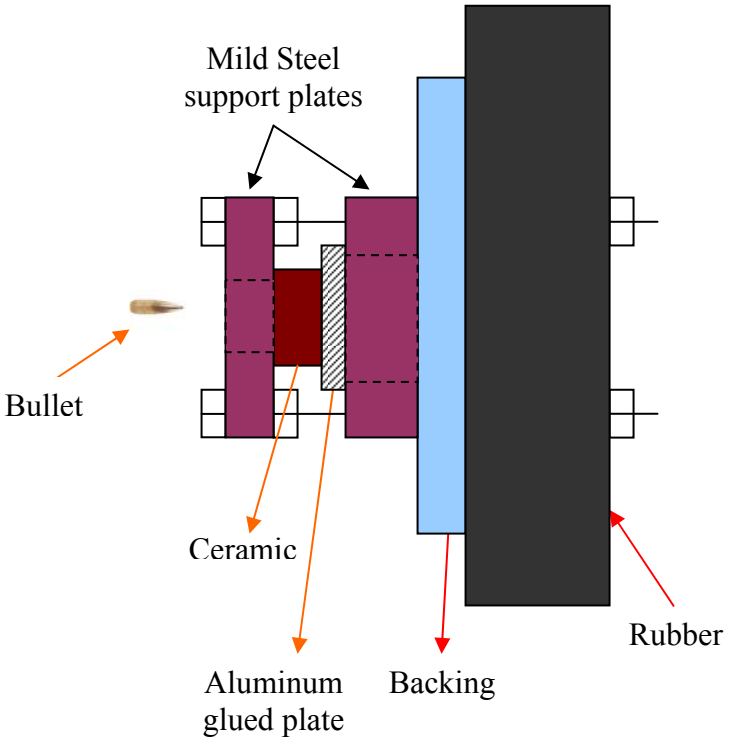

Fig. 3.10 Schematic of the ballistic setup for testing ceramics

Fig. 3.11 Mild steel cover plates for ceramics

gunpowder loads varying between 38 to 42 grains, in order to get different velocities. The front surface of the ceramic was taped with several layers of duct tape in order to hold the fragments together. All the fragmented plates were collected and photographed. Once the B_4C plates were successfully tested, it was decided to test TiB plates.

There can be two approaches to ballistic testing of ceramics. Either the bullet velocity can be varied for plates of the same thickness or plates of different thicknesses can be tested against bullets traveling at similar velocities. In this research, for TiB plates, the second method was adopted to see how the ballistic energy dissipation changes with the thickness of the TiB plate.

3.3.2 Hot Pressing TiB Plates

To get near monolithic TiB, Ti powders (99.95% purity) with particle size less than 44 μm (325 mesh), supplied by Alfa Aesar, Ward Hill, MA, TiB_2 powders (> 98.8% purity) with an average particle size of 10 μm, supplied by Atlantic Equipment Engineers, Bergenfield, NJ, and the sintering agent, Fe-Mo powders with average size of 3 μm, were mixed and blended for 24 hours. The TiB_2, Ti and the sintering agent (Fe-Mo) powders proportion used was 47.4: 48: 4.5 wt% as this proportion was found to yield nearly monolithic TiB in previous research [10].

Two batches of TiB plates with nine different thicknesses (5, 6.5, 8, 10, 12, 14, 15.5, 17, and 18 mm) were hot pressed for ballistic testing. All the plates were 76 mm long and 63 mm wide. For a given thickness, the volume of the plates was calculated and by assuming the density of the plate to be that of monolithic TiB (~ 4.6 g/cc), the total mass of the plate was estimated. For this total mass of the plate, the appropriate amounts of Ti, TiB_2, and Fe-Mo powders required for the preparation of monolithic TiB were

determined. The powders were mixed and cold blended in a tumbling mill container for 24 hours with niobium slugs acting as the grinding media. The milling helps to break down the powder agglomerates and also promotes uniform mixing of the different powders.

After the milling, the powders were taken out and poured into a graphite die. The inside walls of the die were lined with graphite foil to prevent reaction with the powders. The powders were hot pressed at a temperature of 1340˚C and at a pressure of about 10-15 MPa for a sintering time of 2 hours. The schematics of the hot press chamber and the load and temperature profiles are given in Figure 3.12. The chamber was purged with Ar gas initially to minimize oxidation of the powder mixture. The chamber was backfilled with Ar during the hot pressing. The pressed plates were taken out after the chamber was

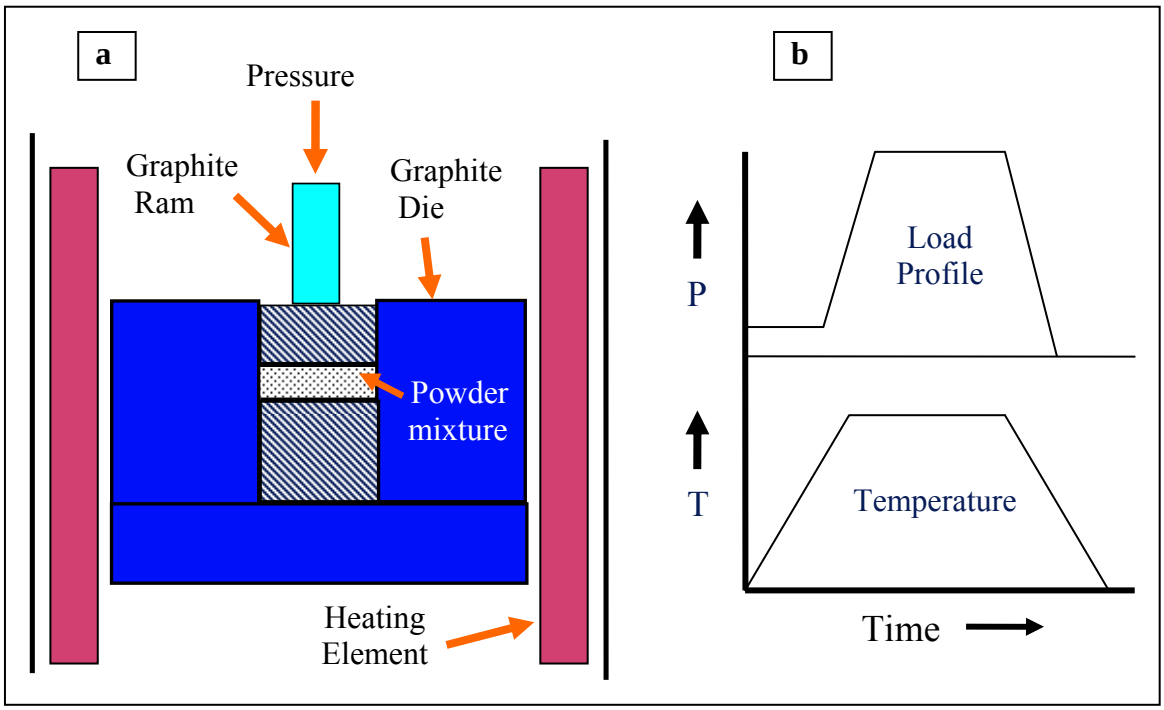

Fig. 3.12 Schematic of (a) hot press chamber and (b) the load and temperature profiles

cooled down to room temperature. The plates were ground to remove the remnants of graphite foil sticking to the surface.

3.3.3 Ballistic Testing of TiB plates

The TiB sample plates were glued to 6061- T6 aluminum plates with dimensions 100 mm X 100 mm X 6.3 mm, as shown in Figure 3.13. The ceramic was painted and numbered to help in assembling the fragments together after the plates were shot. The front faces of the TiB plates were covered with two layers of duct tape to hold the fragments that result from the fracture together. Then, this TiB-Al plate assembly was sandwiched between the two mild steel plates with cutouts. After the TiB-Al plates were shot, TiB fragments were found to be scattered throughout the test chamber. The fragments were collected and were passed through sieves. The deformed surface of the Al backing plate was subjected to deformation analysis as described in the following section.

3.3.4 Aluminum Backing Plate Deformation Measurement

To calculate the energy that went into deformation of the backing plates, it is essential to obtain the surface deformation profile of the bulge in the plates. For this, an

Fig. 3.13 A TiB plate glued to aluminum backing

XYZ stage was used. The deformed backing plate was glued to this stage and the rear surface deformation profile was scanned by a precision dial gage (see Figure 3.14). Figure 3.15 shows the top view of the points at which the Z-deformation displacement of the rear surface of the Al backing plate was measured. The rear surface of the backing plate was divided into 10 radial segments, with increments of 0.2″, *i.e.*, r = 0.2, 0.4, 0.6, 0.8, 1.0, 1.2, 1.4, 1.6, 1.8, 2.0 in inches. For a particular radius, 16 points were chosen on each circle at 16 angles from the x axis, α = 0˚, 22.5˚, 45˚, 67.5˚, 90˚……..337.5˚. In all, there were 160 points at which the Z-deformation of the plate was measured.

The X and Y coordinates for these 160 points were first calculated. One rotation of the X or Y knob in the table moved the stage by 1/16″ so the required points were arrived at by rotating the X and the Y knobs by the appropriate number of turns. A dial gage was used to obtain the Z-deformation at the specified points. The Z-reading was zeroed at the farthest point from the center where the plate touches the stage, which would also be the lowest point. The stage was then moved to the specific points and the

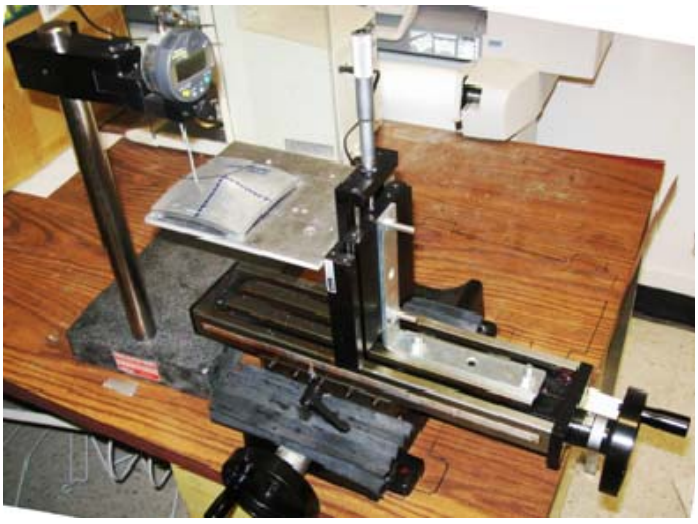

Fig. 3.14 Setup for scanning the rear surface of the deformed aluminum plate

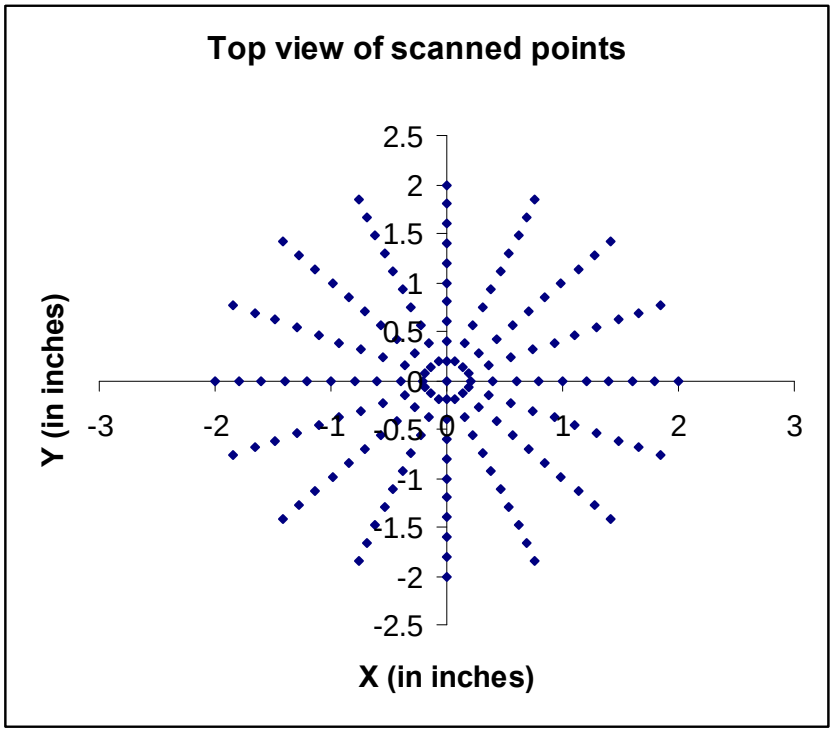

Fig. 3.15 Top view of X, Y points scanned on the backing plates

stylus was raised and allowed to drop to give the Z-reading. Some of the Al plates had bulges which were taller than the span of the stylus. In these cases, the uniaxial slider in the Z direction was used to move the plate down and then the distance moved was added to the stylus reading.

Woodward *et al*. [84] have calculated the energy spent in the bulge deformation of the backing plate. The work done is divided into (a) the work done in tangential/circumferential stretching of the plate and (b) the work done in out of plane bending. The work done in tensile stretching of plate was derived to be

$$W_T = \frac{\pi D^2 t}{4} \sigma_Y \frac{\sum_n \ln(\sec \theta_n)}{N} \tag{3.1}$$

and the work done in bending, W_B, was estimated by using the formula

$$W_B = \frac{\pi t^2 \sigma_Y}{6} \sum_n (R_n \Delta\theta_n) \tag{3.2}$$

where D is the diameter of the dished region, σ_Y, the yield stress, t, the thickness of the backing material, N is the number of radial segments divided, θ_n, the angle of the radial segment r_n to the initial horizontal plane of the plate and $\Delta\theta_n$, the angle between two consecutive radial segments r_n and r_{n+1}, as shown in Figure 3.16.

The scanned Z-deformation profile data were used to construct 2-dimensional curves for each α and the slope at the points corresponding to r_n was calculated using curve fitting. This slope was averaged for the 16 angles for each r_n and then used as tan θ_n, θ_n being the angle of the radial segment r_n to the initial plane of the plate.

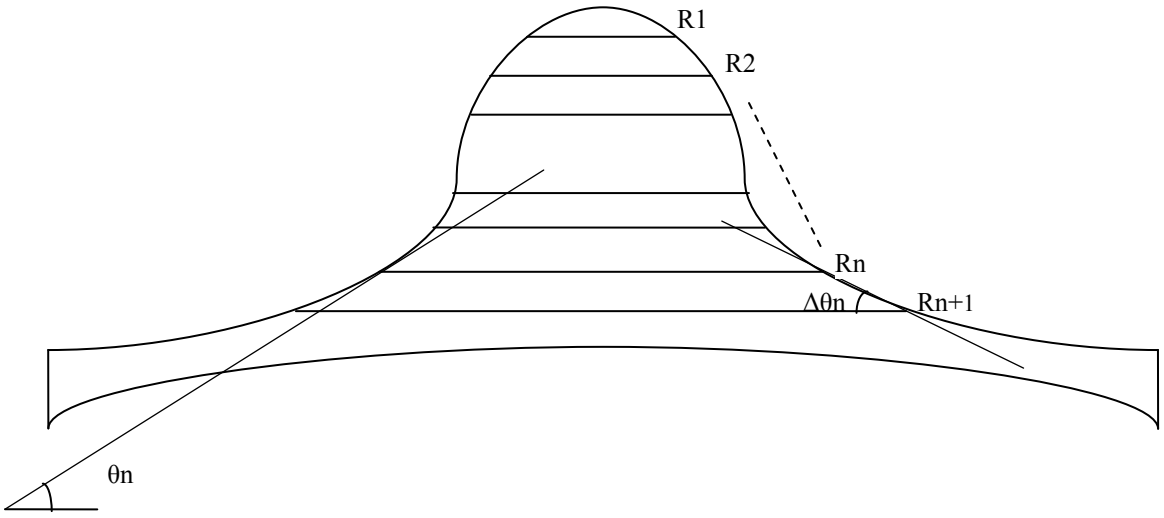

Fig. 3.16 Profile of the bulge on aluminum backing plate

$\Delta\theta_n$, *i.e.*, the angle between two consecutive radial segments, was calculated using the formula

$$\Delta\theta_n = \tan^{-1}\left(\frac{Z_{n+1} - Z_n}{r_{n+1} - r_n}\right) \tag{3.3}$$

where Z_{n+1} and Z_n are the Z values of the radial segments r_{n+1} and r_n, respectively, for a particular angle α. The value of $\Delta\theta_n$ was averaged over 16 values obtained along the 16 angles 0˚, 22.5˚, 45˚, 67.5˚, 90˚……..337.5˚.

3.3.5 Fragmentation of TiB plates

The fragments of the TiB plates resulting from the bullet impact were collected from the ballistic chamber. They were passed through sieves ranging from 13.2 mm to 53 μm in a √2 series. This was repeated for all the plates. To estimate the work done in fragmentation, it is essential to obtain the surface area of the fragments. For this, it was decided to compute the surface area per unit volume of the fragments in each size interval for one particular plate thickness and use these results in calculations for all the plate thicknesses.

The fragments of a particular TiB plate (6.5 mm thick) were chosen and then passed through sieves. This thickness was chosen because it had sufficient fragments in each size interval. A representative sample (upwards of 30 particles) from each size range was taken and randomly dispersed on a paper and photographed at appropriate magnifications. Figures 3.17 to 3.20 show the photographs of dispersed fragments in different size ranges. A grid of horizontal and vertical lines was superimposed over each

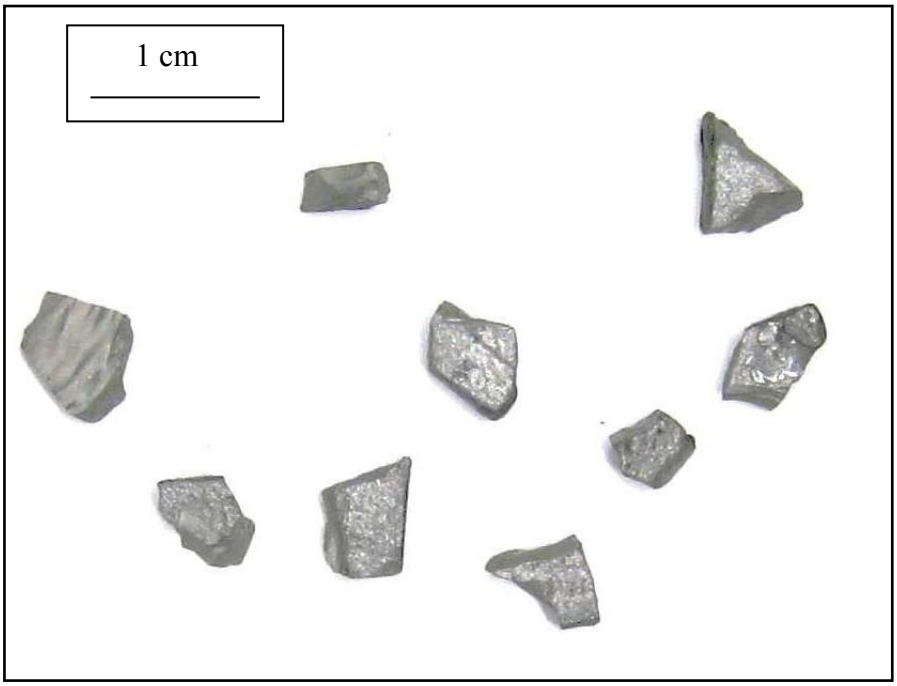

Fig. 3.17 Photograph of dispersed TiB fragments in the size range 9.5 to 13.2 mm

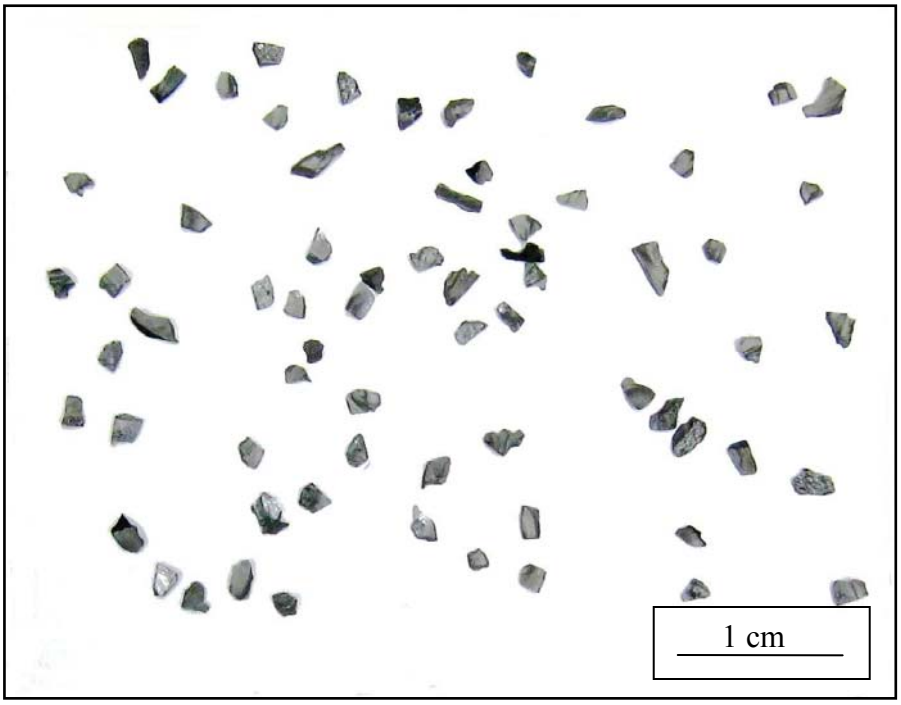

Fig. 3.18 Photograph of dispersed TiB fragments in the size range 2.36- 3.35 mm

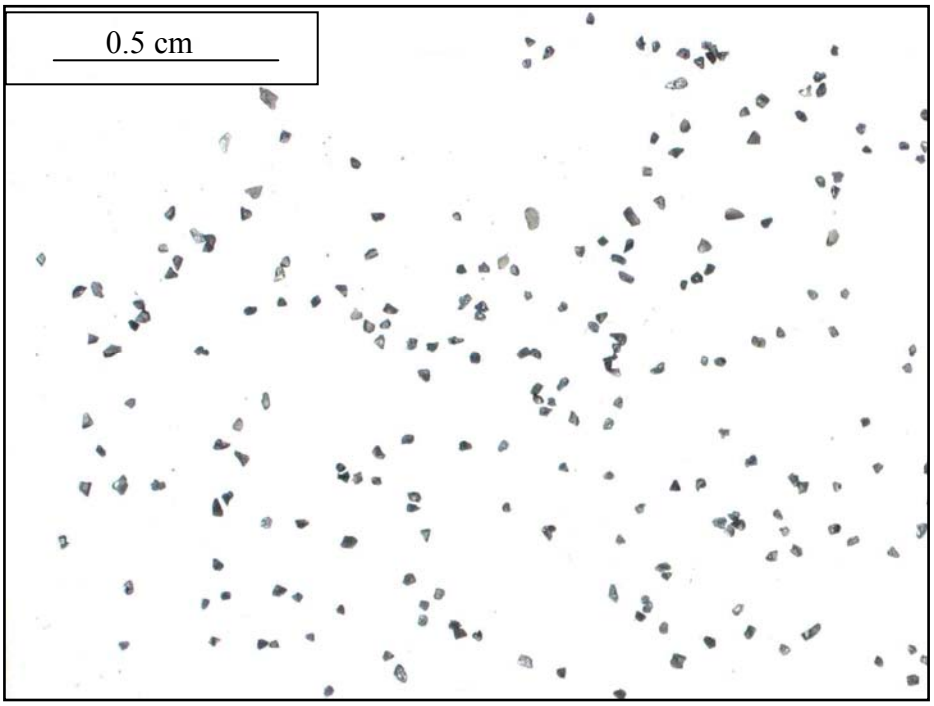

Fig. 3.19 Photograph of dispersed TiB fragments in the size range 425-600 μm

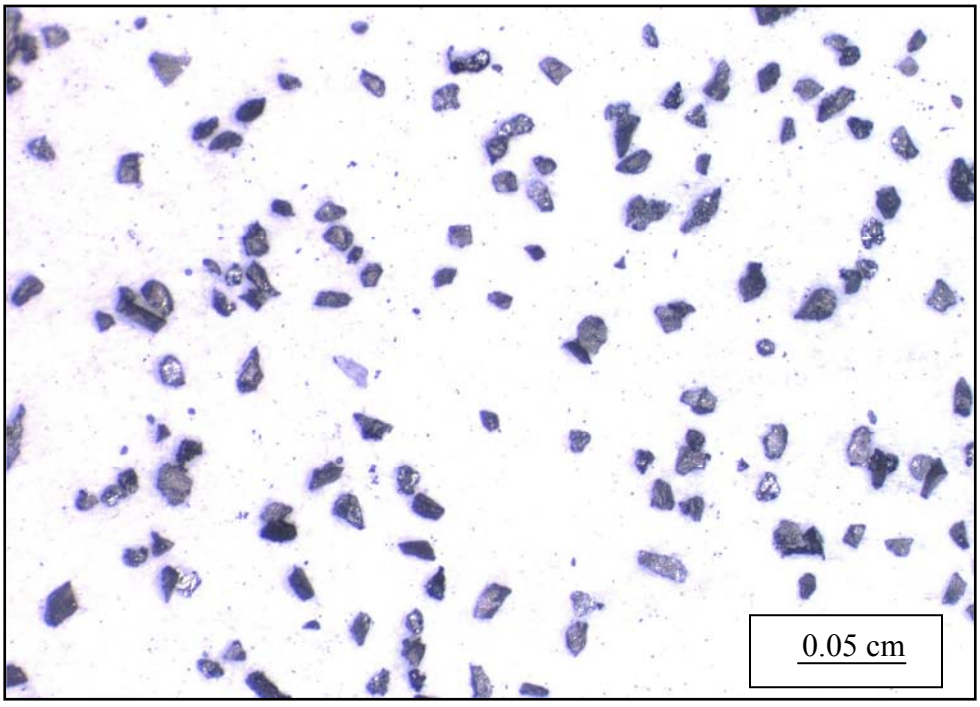

Fig. 3.20 Photograph of dispersed TiB fragments in the size range 75-106 μm

of the photographs to calculate the surface area to volume ratio, as shown in Figure 3.21. The surface area per unit volume is defined as

$$S_v = 2\left(\frac{P_L}{P_p}\right) \tag{3.4}$$

where P_L is the number of particle boundary intersections per unit line length and P_p is the ratio of the number of grid line intersections lying inside particles to the total number of grid line intersection points. S_v values were calculated for fragments from all size ranges for the 6.5 mm thick TiB plate. The volume of fragments in each size range was calculated from the corresponding mass of the fragments assuming constant density for

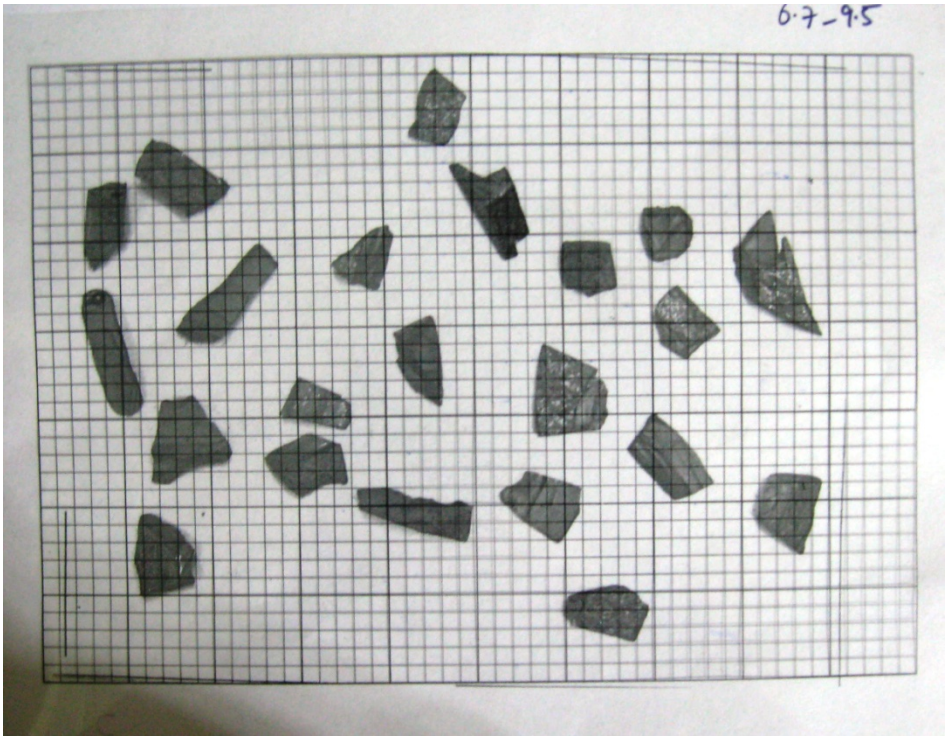

Fig. 3.21 Dispersed TiB fragments in the size range 6.7-9.5 mm with grid

all sizes. The surface area created in each range was calculated by multiplying the volume of fragments in a size range by their surface-to-volume ratio. Then, the total area was obtained by summing up the areas of particles in all the size ranges. Thus, in a particular size interval number, i, if the mass of the fragments is m_i, the bulk material density is ρ, and the surface-to-volume ratio obtained for that interval is $S_{v,i}$, then the total surface area of fragments in that size range, S_i is given by

$$S_i = \left(\frac{m_i}{\rho} \right) S_{v,\,i} \tag{3.5}$$

and hence, the total surface area created, S, would be the summation of the areas created in each size interval, *i.e.*,

$$S = \sum_i \left(\frac{m_i}{\rho} \right) S_{v,\,i} \tag{3.6}$$

Once the total surface area created is known, the work done in fracturing the ceramic, W_f, can be estimated as

$$W_f = \frac{G\,S}{2} \tag{3.7}$$

where G is the toughness or the strain energy release rate. G can be calculated from the formula

$$G = \frac{K_{IC}^{\ 2}}{E} \tag{3.8}$$

where K_{IC} is the fracture toughness and E the elastic modulus. The K_{IC} and E values as determined by Madtha [10] were used to estimate G. The surface-to-volume ratios for each size interval of the fragments obtained from fragments from TiB plate of thickness 6.5 mm were used to calculate the surface areas of fragments of TiB plates of all thicknesses assuming the shape of the fragments is independent of the thickness of the fractured plate. Thus, the energies spent in plastic deformation of the Al backing plate and the fragmentation of TiB were calculated.

CHAPTER 4

RESULTS

4.1 Mild Steel Plates

4.1.1 Bullet Velocity vs. Gunpowder Load

The recorded bullet velocities were plotted against the corresponding gunpowder loads (Figure 4.1). The velocity increased from about 716 m/s to 838 m/s with an increase of gunpowder load from 38 grains to 42 grains. From regression analysis, it was found that the R^2 value for a linear fit was around 0.82 and the standard error for the regression was 13 m/s, which is less than 2% of the mean value.

4.1.2 Penetration in Mild Steel Plates

In all the mild steel plates, the ballistic impact caused the formation of a localized crater on the front surface with a bulge on the rear surface. As the bullet penetrates the plate, it displaces the material around it, causing backward flow of the material which comes out of the crater in the form of "lips." This backward flow also causes the mushroom-like shape of the crater. Figures 4.2 (a) and (b) show sectioned portions of the craters in 9.5 mm and 19.1 mm thick mild steel plates, respectively. They also illustrate how the depth of penetration was measured in the impacted plates.

In Figure 4.2 (a), we can see the crater has reached the rear surface of the plate and has caused bulging whereas in Figure 4.2 (b), the crater is confined to a small depth

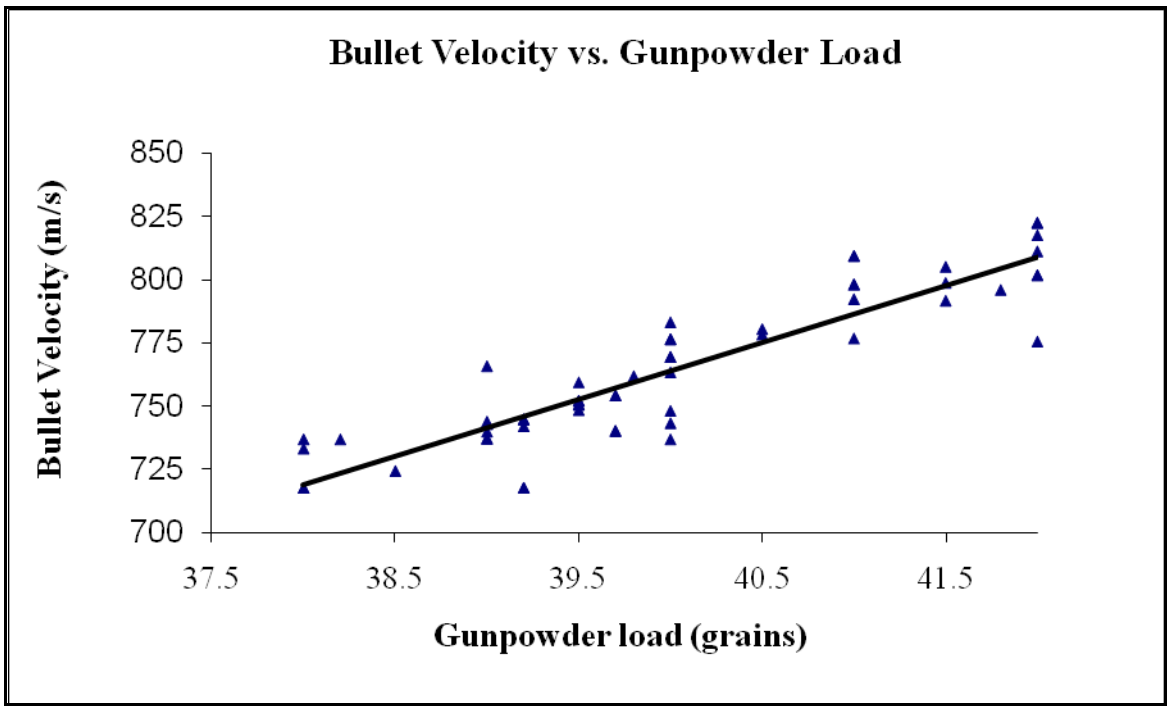

Fig. 4.1 Bullet velocity vs. the gunpowder load

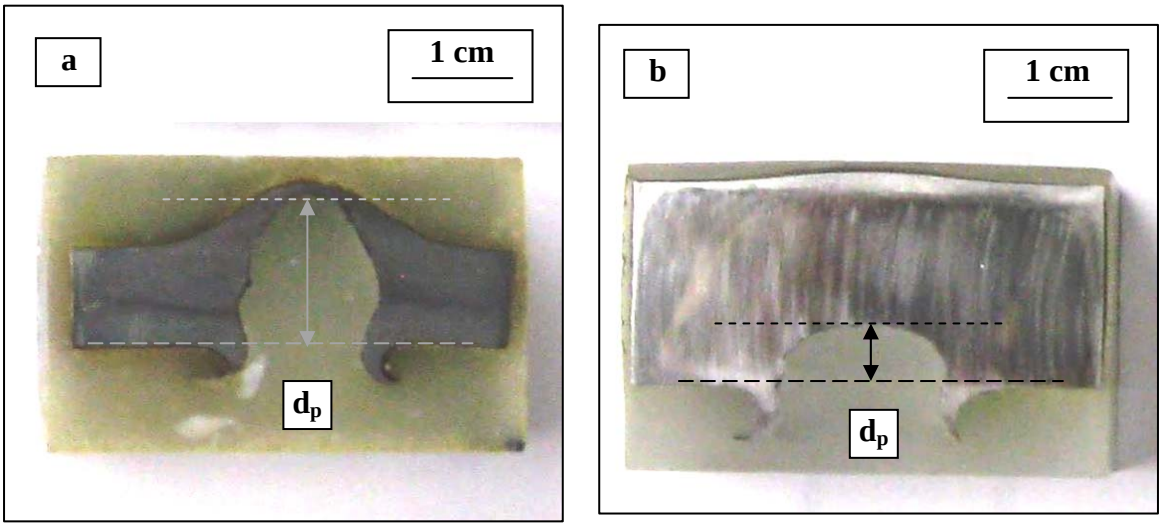

Fig. 4.2 Cross section of a typical crater formed in (a) 9.5 mm and (b) 19.1 mm thick mild steel plates with a schematic of how the depth of penetration, d_p, was measured

and the bulging is minimal.

During the impact, the copper jacket is stripped off the lead core of the projectile and is twisted back, as can be seen from Figure 4.3 (a). The lead core, because of the opposing pressure, expands laterally and flows backward (Figure 4.3 (b)).

The 9.5 mm thick mild steel plates were initially tested with a stainless steel backing against bullets having velocities in the range of 715 to 825 m/s. All the 9.5 mm thick plates showed significant bulging on the rear surface.

For lower velocities, it was observed that the deformed bullet was trapped inside the crater that was created during the penetration process (Figures 4.4, 4.5). Partial penetration was observed for all the velocities and at high velocities (about 820 m/s), complete penetration of the mild steel plate was achieved (Figure 4.6). In this plate, a crack in the bulge on the rear surface was also observed (Figure 4.7).

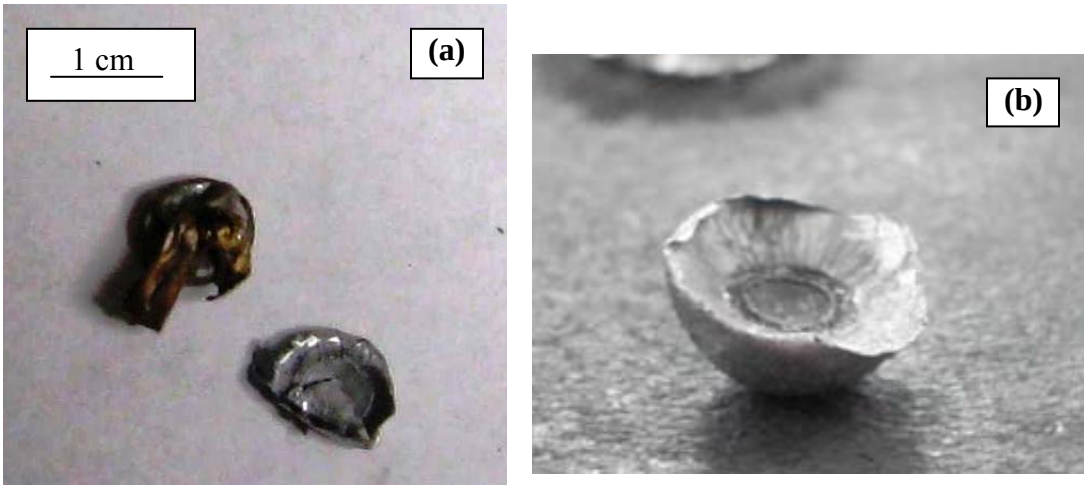

Fig. 4.3 (a) Stripped copper jacket with the deformed lead core after impact with a mild steel plate and (b) a deformed lead core of a bullet after impact

Fig. 4.4 A 9.5 mm thick mild steel plate impacted by a bullet shot at 718 m/s

Fig. 4.5 A 9.5 mm thick mild steel plate impacted by a bullet shot at 777 m/s

Fig. 4.6 Front surface of 9.5 mm thick mild steel plate impacted by a bullet with velocity 823 m/s

Fig. 4.7 Cracked bulge at the rear surface of 9.5 mm thick mild steel plate impacted by a bullet with velocity 823 m/s

To investigate the role of the backing plate, mild steel plates of the three thicknesses were then tested using aluminum backing plate instead of the stainless steel plate. When a 9.5 mm thick mild steel plate was shot at with aluminum as the backing plate, it was found that even for a low bullet velocity (744 m/s), complete penetration was observed. A plug was ejected, as shown in Figure 4.8. When the stainless steel backing plate was used, complete penetration was achieved at a higher velocity (823 m/s) and no plug formation was observed. This indicates that the contribution of the aluminum backing plate in resisting the bullet penetration was less than that of the stainless steel backing. Hence, it was easier for the bullet to shear a plug from the rear side of the mild steel plate in this case.

Fig. 4.8 Rear surface of the impacted 9.5 mm mild steel plate with the ejected plug

The 15.9 mm thick and 19.1 mm thick mild steel plates were also impacted by the bullets with the aluminum backing plate. Figures 4.9 through 4.16 show the front faces of some of the impacted plates of the two thicknesses, 15.9 mm and 19.1 mm, impacted at different velocities. For the 15.9 mm and 19.1 mm thick plates, with increasing bullet velocity, the crater diameter reduces, as can be seen from Figures 4.9 to 4.12 and from Figures 4.13 to 4.15. Also, the crater lips are more clearly formed for lower velocities and do not “petal” out at higher velocities.

Fig. 4.9 A 15.9 mm thick mild steel plate impacted by bullet at 737 m/s

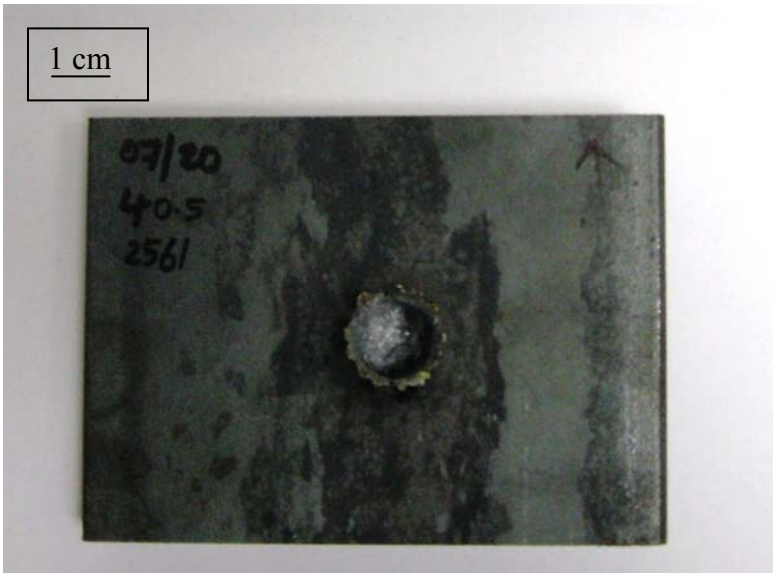

Fig. 4.10 A 15.9 mm thick mild steel plate impacted by bullet at 781 m/s

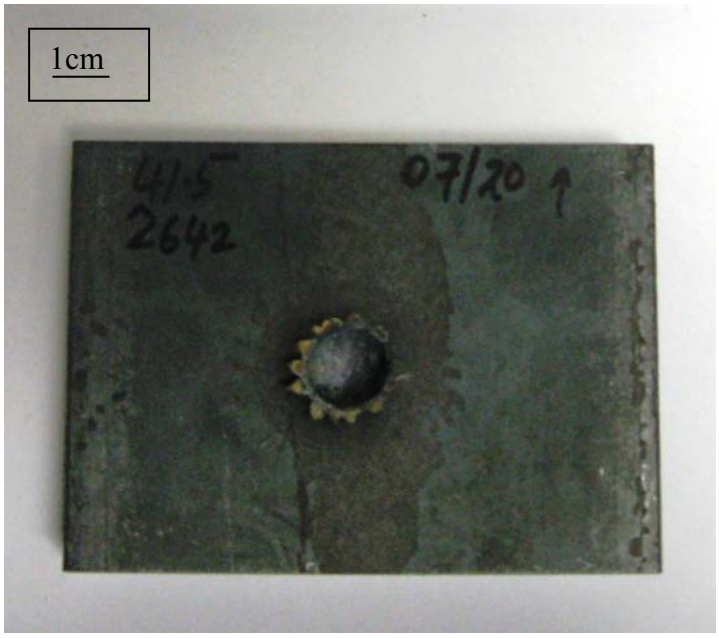

Fig. 4.11 A 15.9 mm thick mild steel plate impacted by bullet at 805 m/s

Fig. 4.12 A 15.9 mm thick mild steel plate impacted by bullet at 839 m/s

Fig. 4.13 A 19.1 mm thick mild steel plate impacted by bullet at 733 m/s

Fig. 4.14 A 19.1 mm thick mild steel plate impacted by bullet at 762 m/s

Fig. 4.15 A 19.1 mm thick mild steel plate impacted by bullet at 776 m/s

Fig. 4.16 A 19.1 mm thick mild steel plate impacted by bullet at 792 m/s

4.1.3 Penetration Depth vs. Velocity

The normalized penetration depth values of the tested mild steel plates were plotted against the bullet velocities for all the thicknesses. These are shown in Figures 4.17 to 4.19. The penetration depth was normalized with respect to the plate thickness.

For the 9.5 mm thick plates, there was not much variation in the penetration depths with increase in the bullet velocity. The penetration depth even for the lowest velocity was more than the plate thickness. This indicates the occurrence of bulging as the bullet has traveled through the plate thickness. The final point (velocity 823 m/s) corresponded to the case of complete penetration with the bulge cracking at the rear surface and thus showed a higher depth. From Figures 4.18 and 4.19, we can see that both the 15.9 mm thick and 19.1 mm thick plates show a general increase in the penetration

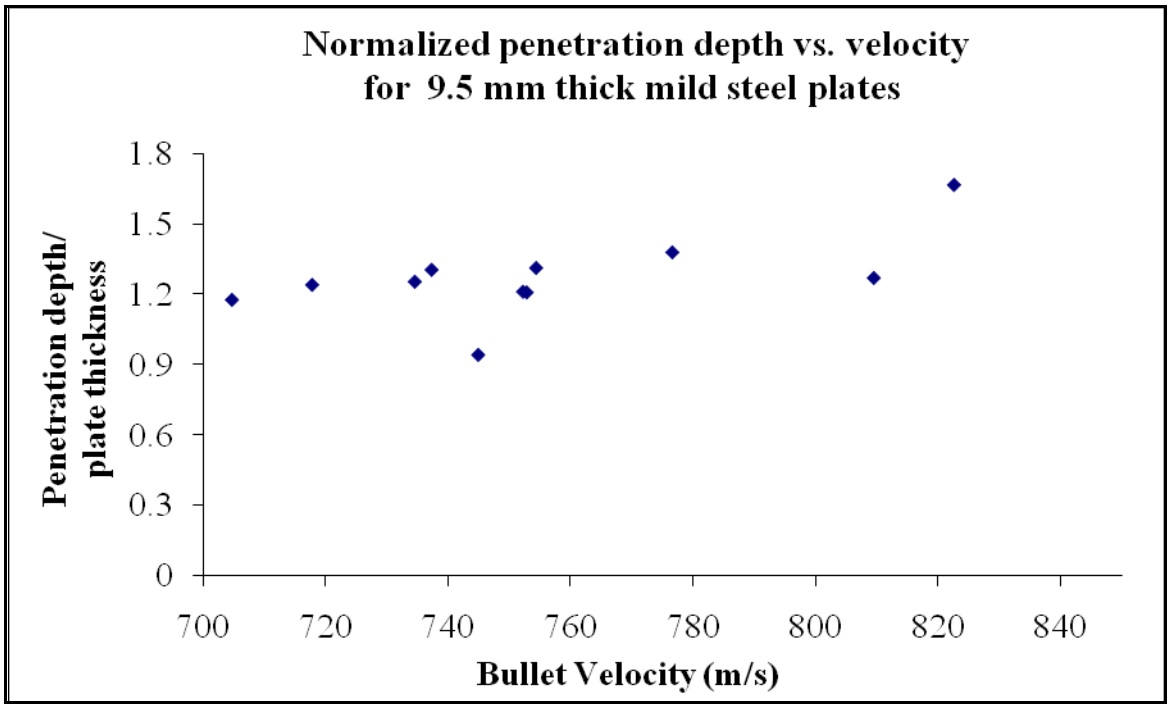

Fig. 4.17 Normalized penetration depths vs. bullet velocity for 9.5 mm thick mild steel plates

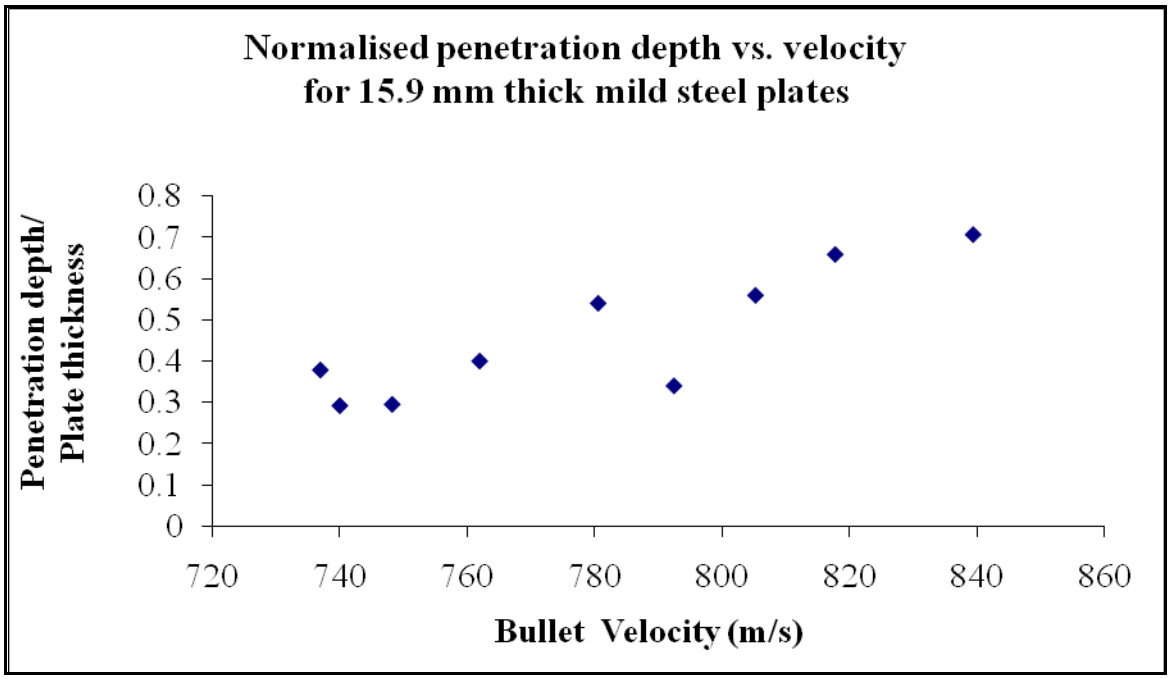

Fig. 4.18 Normalized penetration depth vs. bullet velocity for 15.9 mm thick mild steel plates

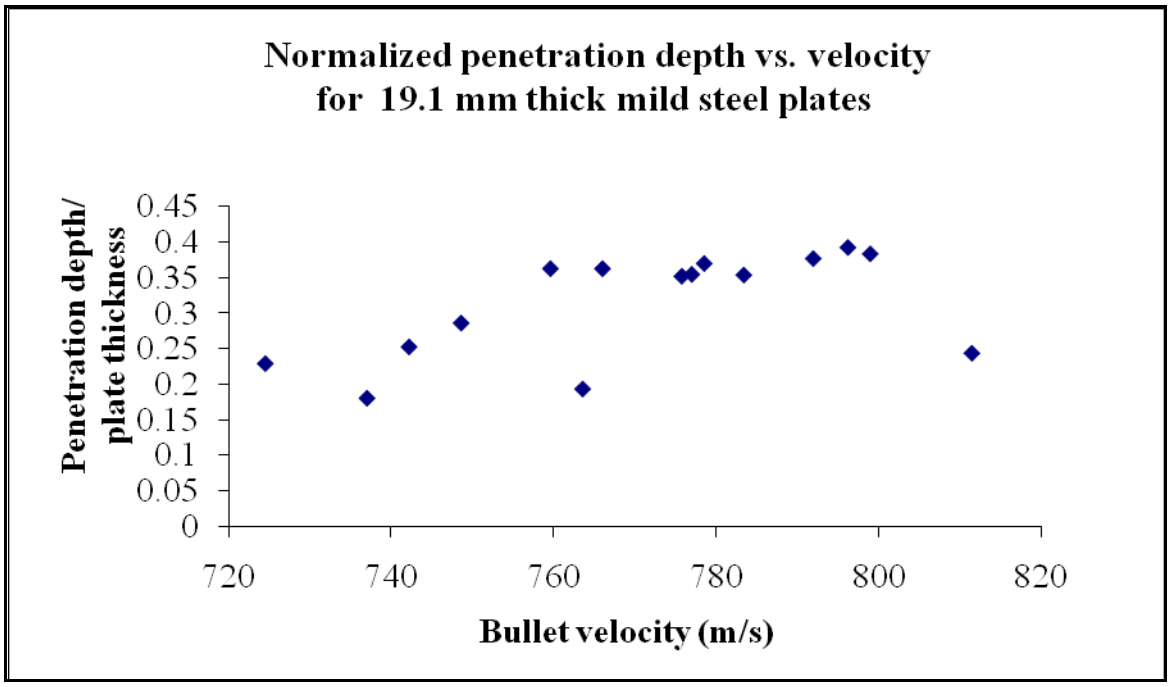

Fig. 4.19 Normalized penetration depth vs. bullet velocity for 19.1 mm thick mild steel plates

depth with velocity. The normalized depth of penetration increases from 0.3 to 0.7 for the 15.9 mm thick plates and from 0.2 to 0.4 for the 19.1 mm thick plates. For lower bullet velocities, the slope of the penetration depth vs. velocity appears steeper for both the thicknesses. Then, this slope becomes gentle at higher velocities. In the 19.1 mm thick plates, the increase in the penetration depth for velocities between 760 and 800 m/s is negligible. This trend can be explained on the basis of two competing modes of energy absorption: (1) ductile hole formation and (2) dishing of the plate. At lower velocities, especially for thicker plates, the first mode will be dominant and then there will be a transition to the second mode where more energy will be consumed in bending or dishing of the rear surface of the plate. A more detailed discussion on this will be included in the next chapter.

In some cases, for plates of all thicknesses, the penetration depth was atypically

low even at high velocities. One reason for this anomaly could be that during the impact, the steel plate might have moved with respect to the bullet and hence, the impact might not have been normal to the plane of the plate. Due to the oblique penetration, the craters observed were more laterally elongated and did not have significant depths. In Figure 4.20, a comparison of one such case with another case of normal impact for similar velocities is illustrated.

4.1.4 Crater Volume vs. Velocity

The crater volume vs. bullet velocity curves (Figures 4.21 to 4.23) were more consistent than the penetration depth vs. velocity curves. Even in cases of oblique impact where the penetration depth is significantly lower than that with perpendicular impacts, the crater volume value does not reflect the drastic decrease in depth. This is because, for an oblique impact, though the penetration depth is less than that in the case of normal penetration for similar velocities, the crater volumes generated in both the cases are not very different.

The curves reveal a steeper increase in the volume for lower velocities and then a modest increase at higher velocities. This trend could again be explained by the transition from one energy absorbing mechanism (ductile hole formation) to another (dishing). For the 9.5 mm thick plate (Figure 4.21), there is not much difference in the crater volume generated beyond 732 m/s. The 15.9 mm thick plates (Figure 4.22) show a steep increase in the crater volume up to a velocity of 762 m/s and then the slope decreases beyond 793 m/s. The increase in crater volume with velocity is less in this range of higher velocities. For the 19.1 mm thick plates (Figure 4.23), the crater volume again shows a general trend of increase. For velocities between 762 m/s and 793 m/s, there is not a significant

Fig. 4.20 Oblique penetration (left) and normal penetration (right) for similar bullet velocities, 764 and 760 m/s, respectively

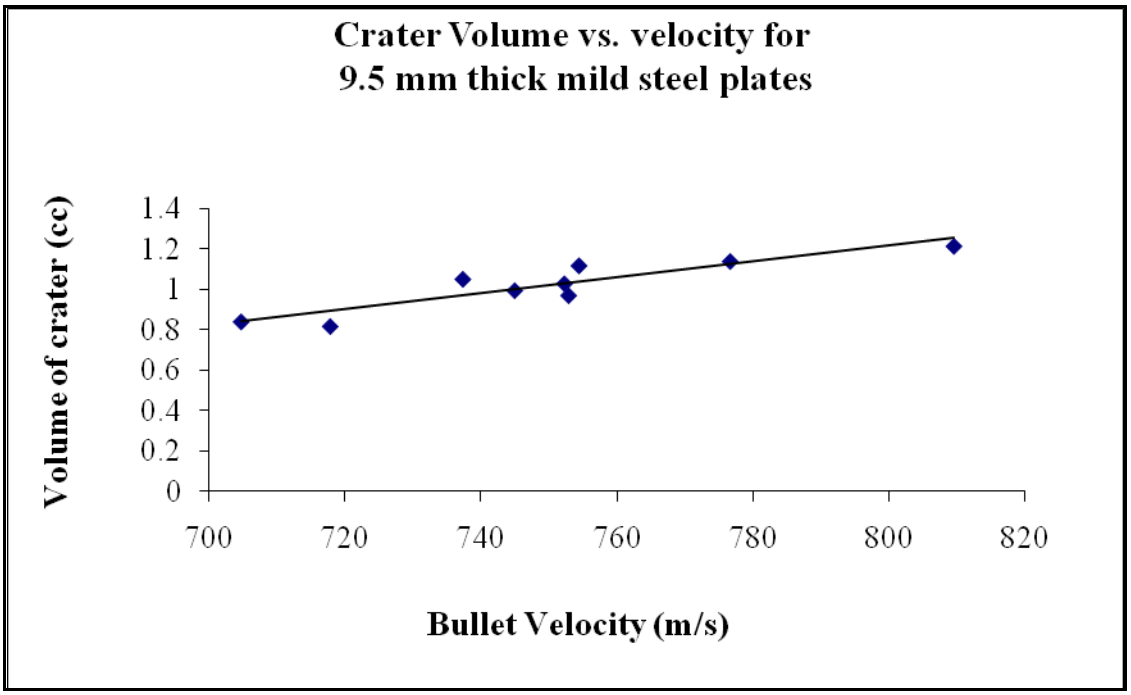

Fig. 4.21 Crater volume vs. bullet velocity for 9.5 mm thick mild steel plates

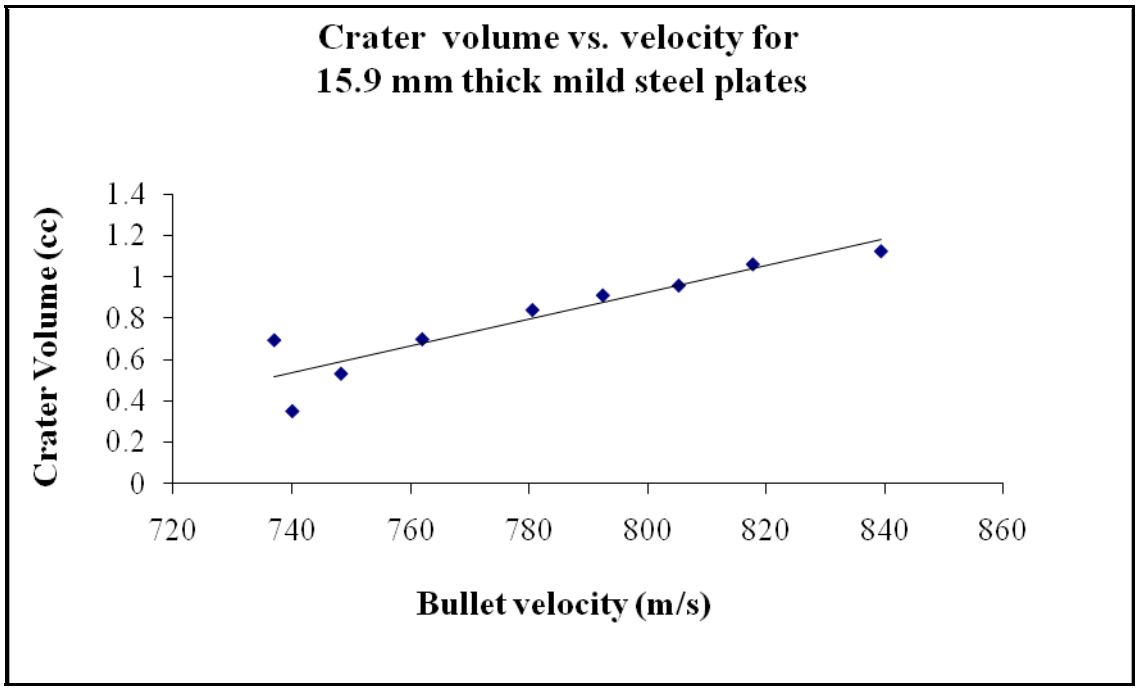

Fig. 4.22 Crater volume vs. bullet velocity for 15.9 mm thick mild steel plates

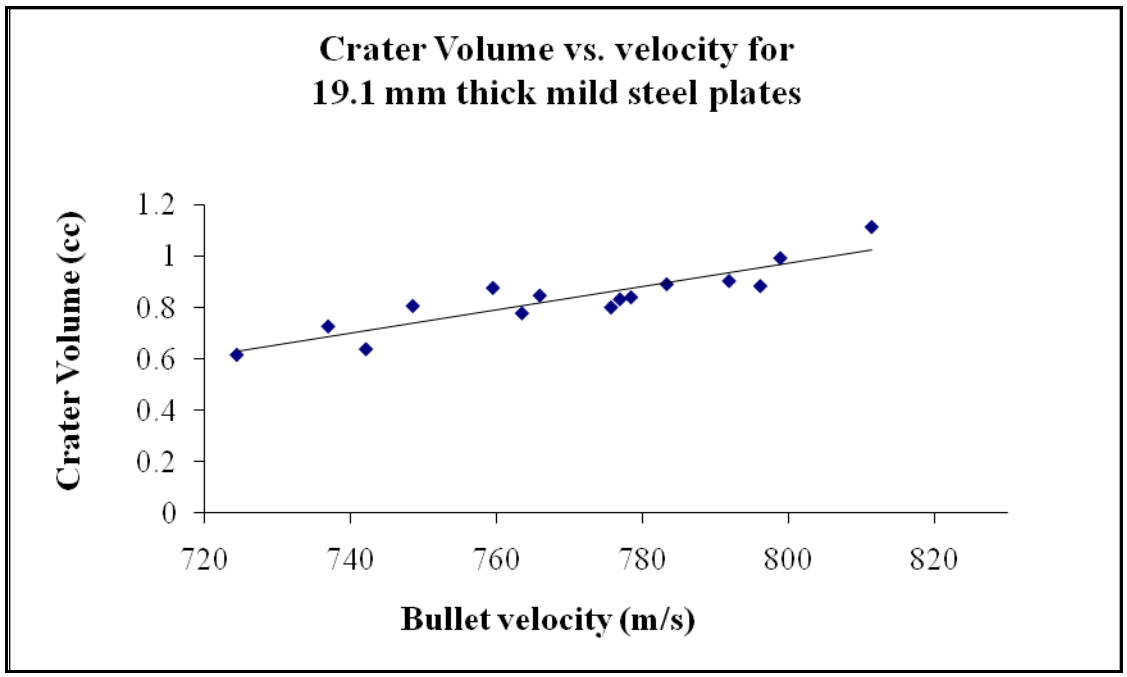

Fig. 4.23 Crater volume vs. bullet velocity for 19.1 mm thick mild steel plates

increase in the volumes.

For the 9.6 mm thick plates, the change in crater volume with velocity is not significant because dishing is the dominant mechanism. The transition from one mode to another is most prominent for the 15.9 mm thick plates.

4.2 Ballistic Testing of Ceramic Plates

4.2.1 Boron Carbide Trial Plates

Boron carbide tiles of dimensions 100 mm x 100 mm x 6.3 mm were impacted with bullets shot at seven different velocities ranging from 737 to 823 m/s. The fragments were held together by layers of duct tape and also by the confining pressure of the mild steel cover plates with cutouts. It was observed that the fracture waves propagated from the rear surface towards the front in a radial fashion. For lower velocities, the outermost portions of the rear surface reveal the presence of star cracks but still were intact as the fracture conoid did not reach those regions. The radial nature of these fracture waves can be seen in Figure 4.24.

Figures 4.24 to 4.27 show that as the impact velocity increases, the fragmentation becomes more severe. For the lower velocities, barring the comminution zone, the rest of the fractured ceramic fragments are held in place but as the velocities increase, the size of the comminution zone increases and the fragmentation occurs over a larger area. In Figures 4.24 to 4.26, the outermost fragments are coarse and the surface is intact over some area. In Figure 4.27, however, the outer fragments are smaller and the surface is intact only over a small area near the edges. The backing aluminum plates also showed greater bulging on their rear surfaces for higher velocities, indicating a higher amount of residual energy of the bullet left after defeating the ceramic.

Fig. 4.24 Boron carbide plate shot by bullet at 715 m/s

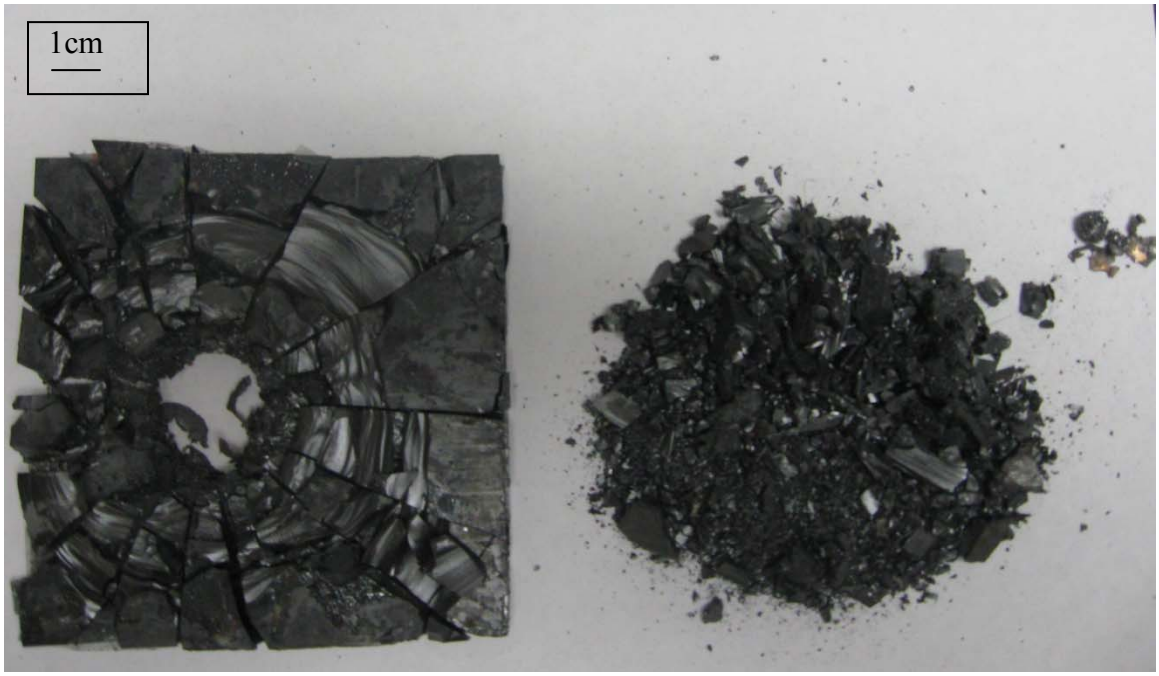

Fig. 4.25 Boron carbide plate shot by bullet at 750 m/s

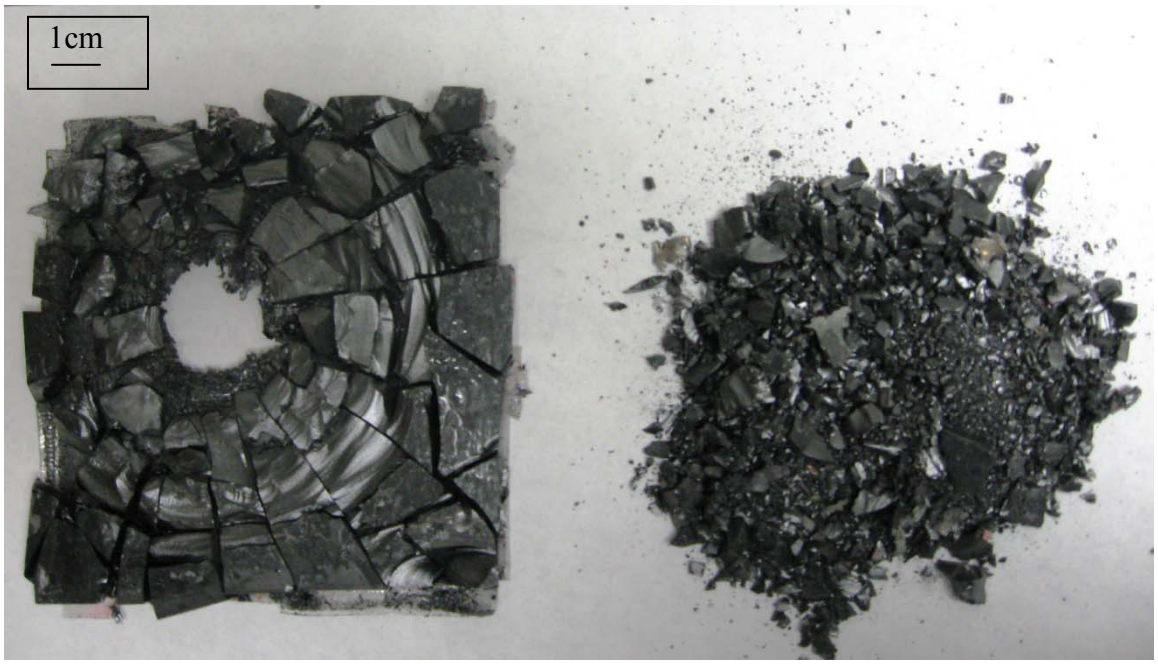

Fig. 4.26 Boron carbide plate shot by bullet at 764 m/s

Fig. 4.27 Boron carbide plate shot by bullet at 814 m/s

4.2.2 Titanium Boride Plates

Two batches of TiB plates of nine thicknesses were tested against bullets with the same gunpowder loading of 37.5 grains. If the chronograph failed to display the bullet velocity in an experiment, the trial was repeated for another plate of the same thickness until two data points for each thickness were obtained. Table 4.1 shows these velocities for the tested plates. All velocities were between 725 m/s and 755 m/s. The mean velocity was close to 739 m/s and the standard deviation was about 8.5 m/s (~ 1.2 % of the mean value).

Table 4.1 TiB plates of different thicknesses and the corresponding bullet velocities

Sample Name	Ceramic thickness (mm)	Bullet Velocity (m/s)
TiB 5b	5	727
TiB 5c	5	735
TiB 6.5b	6.5	753
TiB 6.5c	6.5	741
TiB 8b	8	737
TiB 8c	8	739
TiB 10a	10	739
TiB 10b	10	739
TiB 12a	12	724
TiB 12b	12	743
TiB 14a	14	751
TiB 14b	14	750
TiB 15a	15	744
TiB 15b	15	727
TiB 17a	17	736
TiB 17b	17	735
TiB 18a	18	752
TiB 18b	18	737

The fragments ejected after ballistic impact on two batches of TiB plates of nine thicknesses were collected. The fragments were not held in place and usually were found dispersed throughout the ballistic testing area. It was attempted to rearrange them based on initial markings on the edges. The fragments were angular in shape and thicker on the front surface than on the rear. This is a result of the propagation of the fracture wave from the rear surface towards the front.

The fragments were passed through sieves with sizes ranging from 13.2 mm to 53 μm in a √2 series. Figures 4.28 and 4.29 show the cumulative weight percent of the fragments of the two batches, passing through a mesh size, plotted against a log scale of the upper mesh size. These figures reveal that in general, thicker plates have a higher percentage of coarser fragments.

For example, in Figure 4.28, if we look at a narrow range of the cumulative percentage of fragments, say 27% to 32%, we can see that the corresponding upper mesh size increases with the plate thickness. For plate thicknesses of 5, 6.5, and 8 mm, fragments finer than the mesh size 2.36 mm comprise about 30% of the total mass. On the other hand, for 17 mm thick and 18 mm thick plates, 26.5% and 32% of the total mass belongs to fragments that passed through the mesh size 6.7 mm. For the 12 mm thick plate, fragments finer than 3.35 mm comprise of 28.1% of the total mass whereas for the 15 mm thick plate, 27.6% of the total mass is found in fragments finer than 4.75 mm.

Similarly, in Figure 4.29, for a particular upper mesh size, say, 3.35 mm, we can see that the cumulative mass percentages of fragments which are finer than that size decrease with plate thickness. For a 5 mm thick plate, close to 43 % of the total mass is carried by fragments finer than 3.35 mm, whereas for an 18 mm thick plate, less than

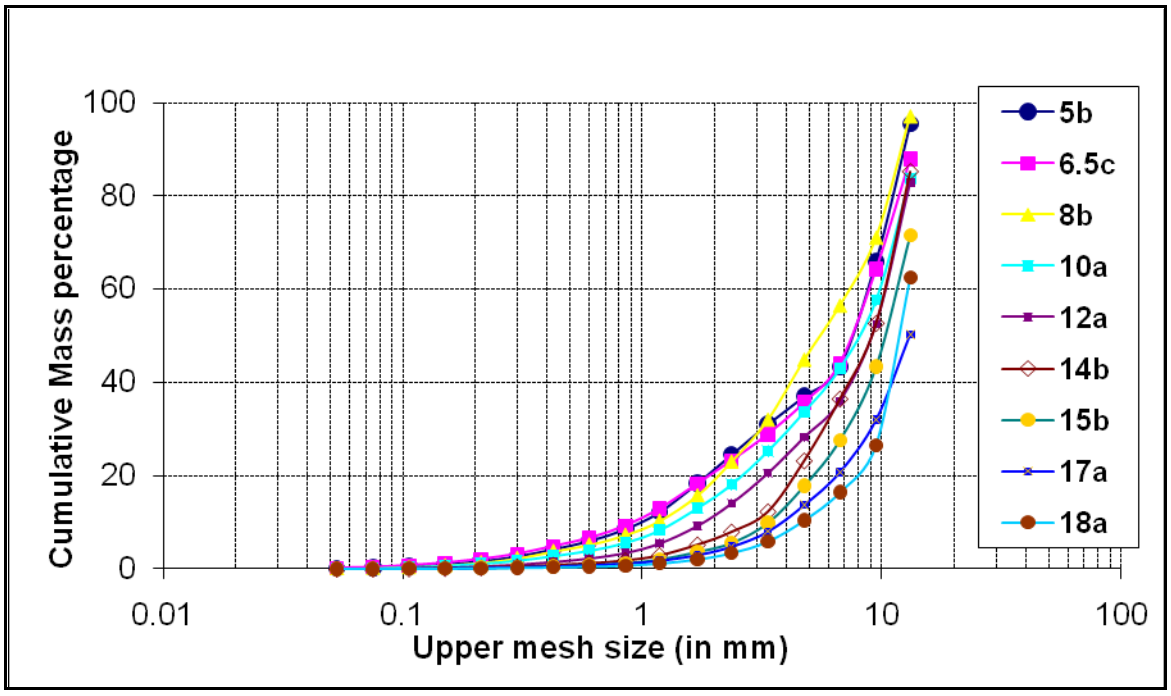

Fig. 4.28 Cumulative mass % less than mesh size of TiB fragments, from batch 1, vs. log (upper mesh size, in mm)

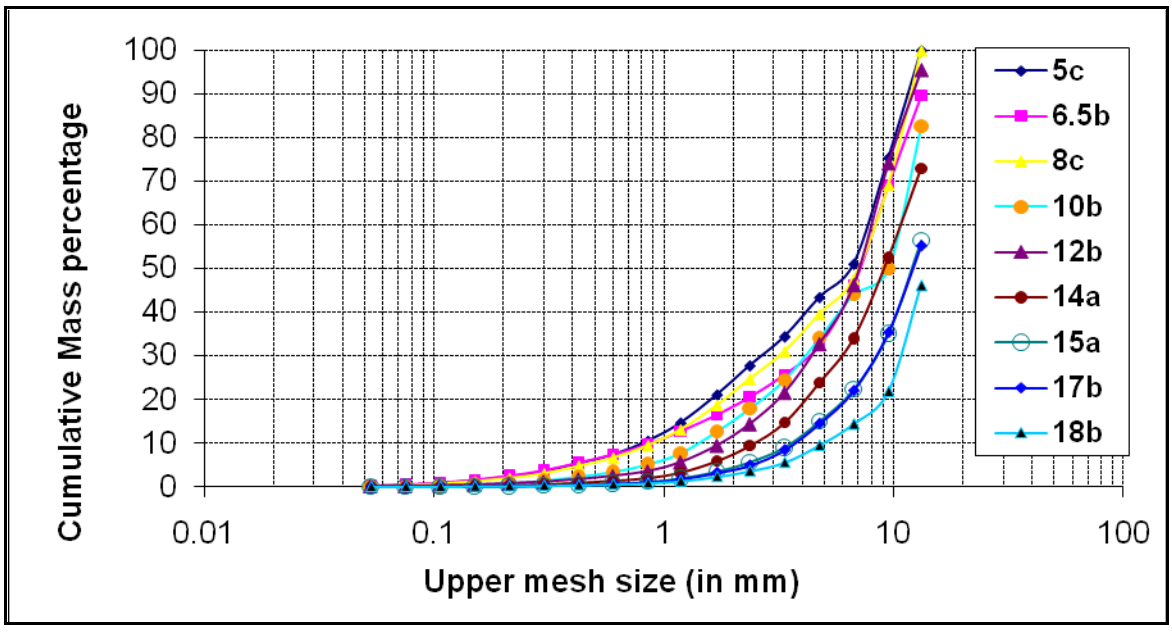

Fig. 4.29 Cumulative mass % less than mesh size of TiB fragments, from batch 2, vs. log (upper mesh size, in mm)

10% of the total mass of fragments is finer than 3.35 mm. This percentage decreases from 40% to 15% as we go from plate thickness of 8 mm to 17 mm.

For the thicker plates (*e.g.*, more than 14 mm), most of the fragments outside the comminution zone were intact and were in the form of big chunks. For the thinner plates, the fragments were smaller and it was difficult to reassemble them in their original positions. This can be seen from the figures of the assembled fragments. Figures 4.30 to 4.38 show the coarser fragments which could be re-assembled in their initial positions and the finer fragments, which mainly comprised of powder obtained from the comminution zone. All these figures show the rear surface of the ceramic. As explained before, the base of the fracture cone is situated on the rear surface and the cone narrows down to a smaller area at the front surface of the ceramic. We can see that for the thicker plates, the outer fragments are intact and the comminution zone is small as a result of which the fragments become much coarser. In the thinner plates, the comminution zone

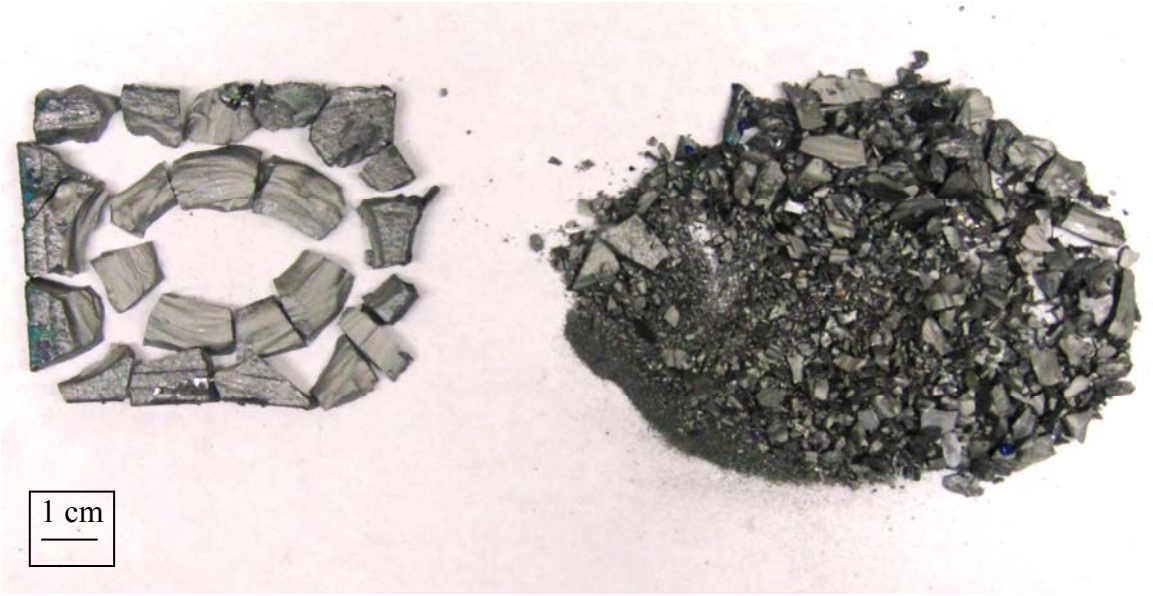

Fig. 4.30 5 mm thick TiB plate shot by bullet at 727 m/s

Fig. 4.31 6.5 mm thick TiB plate shot by bullet at 741 m/s

Fig. 4.32 8 mm thick TiB plate shot by bullet at 739 m/s

Fig. 4.33 10 mm thick TiB plate shot by bullet at 739 m/s

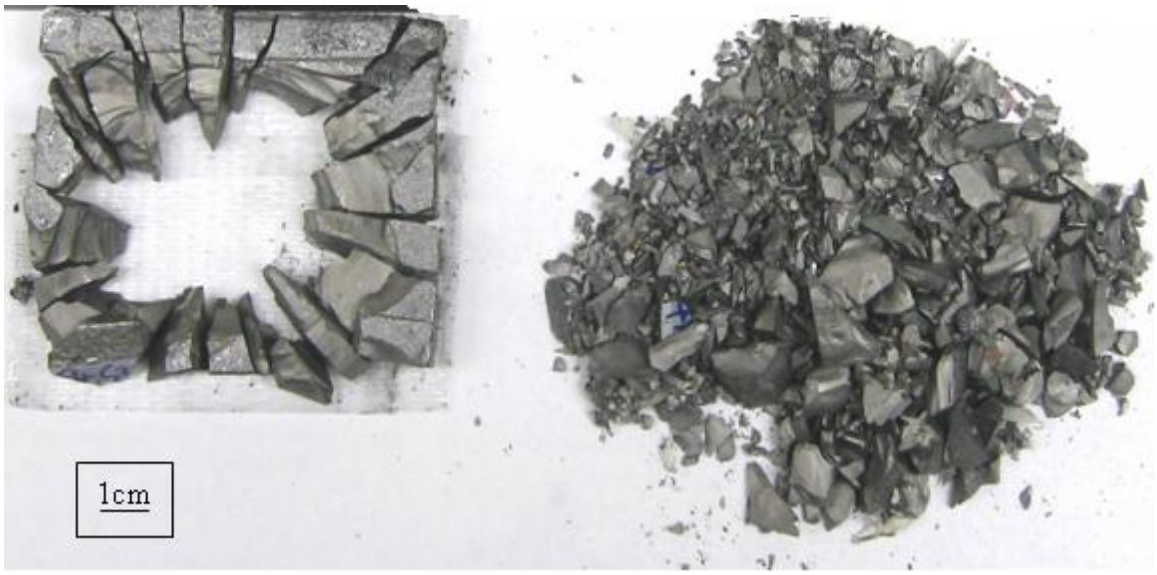

Fig. 4.34 12 mm thick TiB plate shot by bullet at 724 m/s

Fig. 4.35 14 mm thick TiB plate shot by bullet at 750 m/s

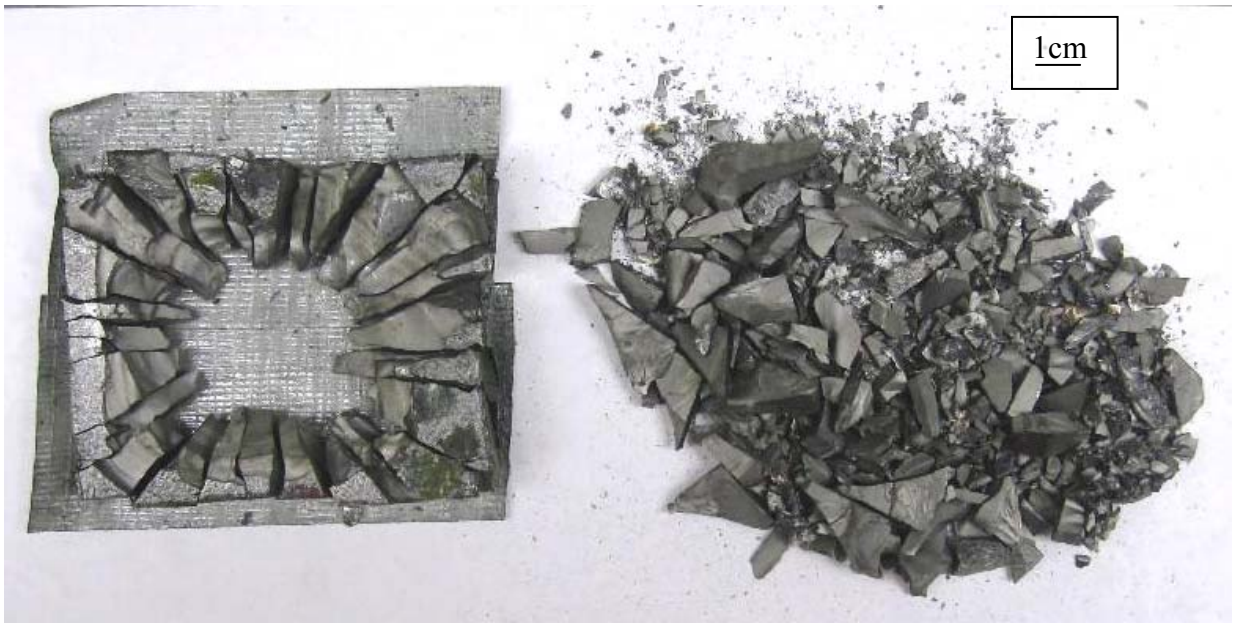

Fig. 4.36 15 mm thick TiB plate shot by bullet at 744 m/s

Fig. 4.37 17 mm thick TiB plate shot by bullet at 736 m/s

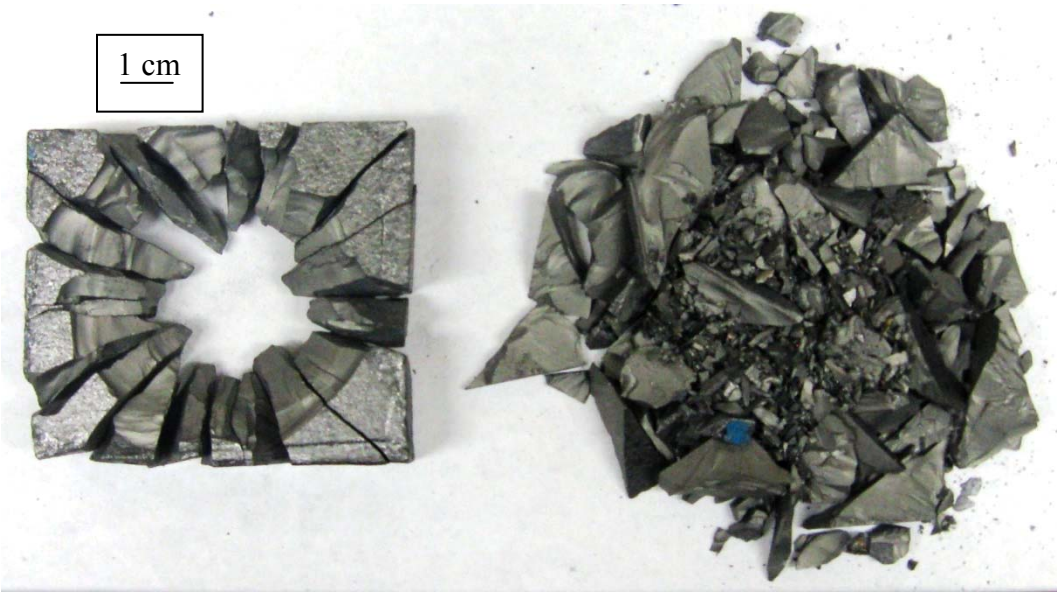

Fig. 4.38 18 mm thick TiB plate shot by bullet at 737 m/s

almost extends to the edges of the plates and the fragments are smaller in size. Fracture waves can be seen to propagate in a radially outward direction. Most of the coarser fragments are wedge shaped and angular. Particles having such shapes have high surface-to-volume ratios.

4.2.3 Aluminum Backing Plates Deformation

The aluminum backing plates were collected after the impact and investigated. All the plates typically show some curvature due to the bending loads while the plates behind thinner TiB plates also show signs of plug formation. In some rare cases where the ceramic is not able to absorb sufficient energy, tensile cracks were present on the rear surface (Figure 4.39).

Figures 4.40 to 4.42 show how the bending curvature gets reduced as the TiB plate thickness is increased. Apart from the bending, localized tensile stretching of the plate, which causes plug formation, can be seen in Figure 4.40.

The rear surface of these backing plates was scanned and the Z-deformation at 160 points was measured by means of a dial gage as described earlier. These points were fed into a MATLAB program to obtain three-dimensional profiles of the rear surfaces. Some of these profiles are shown in Figures 4.43 to 4.46.

4.2.4 Ceramic Fragmentation Energy

The energy spent in fragmentation of the plates for all thicknesses was calculated based on the method discussed in Section 3.3.5. It was found that this energy represented only a miniscule portion of the initial kinetic energy of the projectile. Table 4.2 lists the fragmentation energy calculated for all the thicknesses. The percentage of the bullet

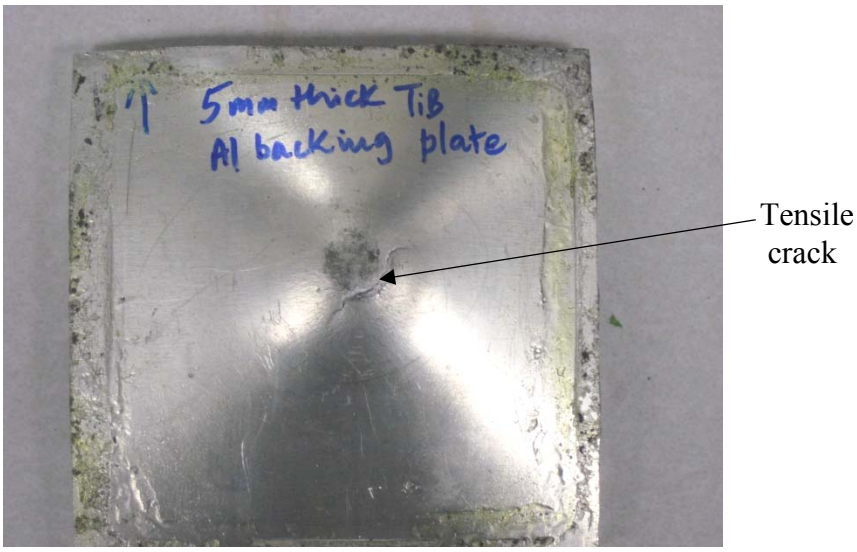

Fig. 4.39 A tensile crack on the rear face of an aluminum backing plate

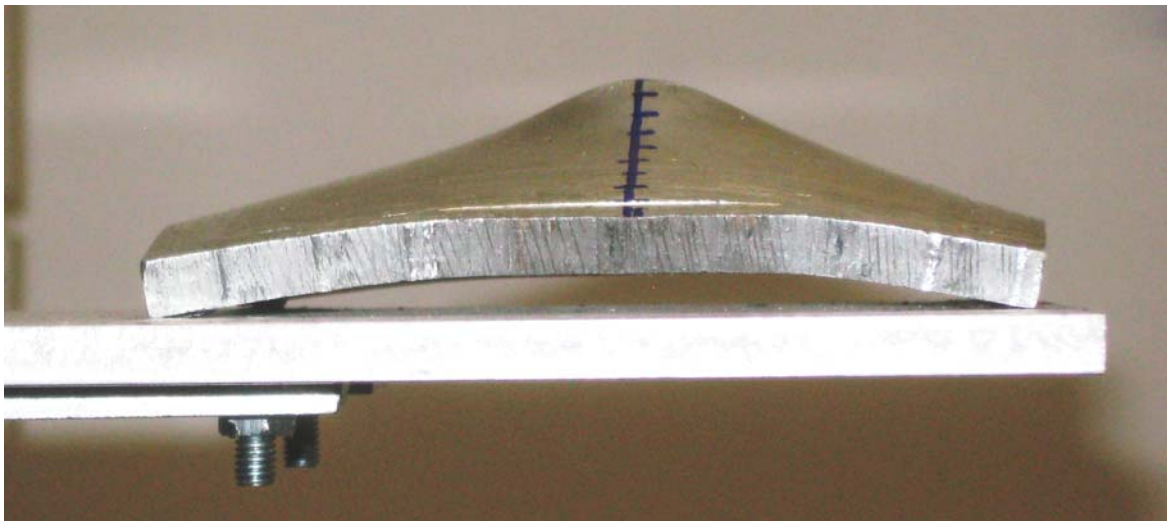

Fig. 4.40 Aluminum backing plate behind 6.5 mm thick TiB plate

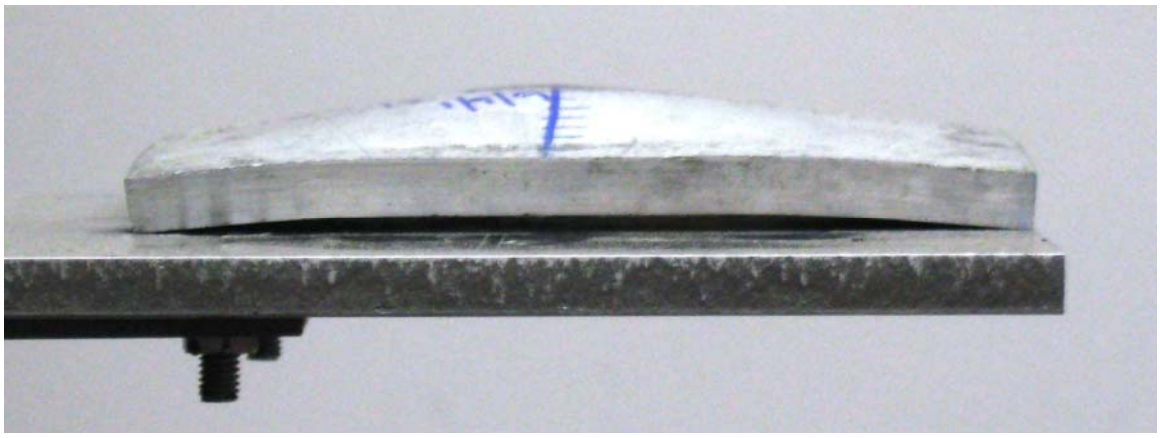

Fig. 4.41 Aluminum backing plate behind 12 mm thick TiB plate

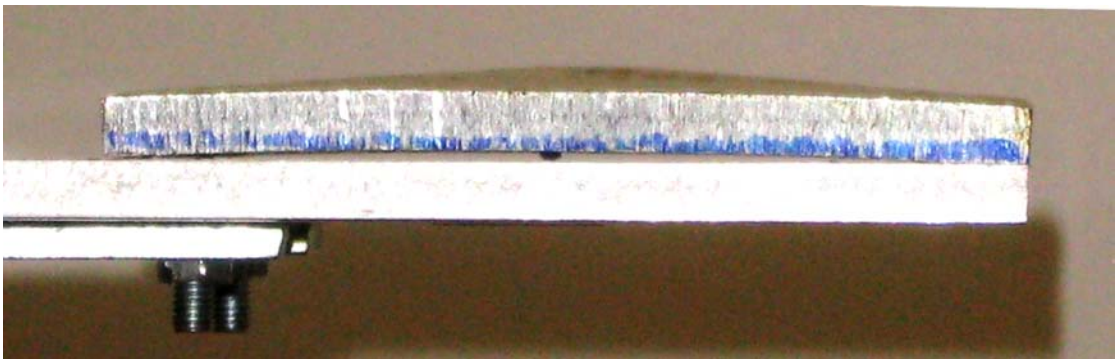

Fig. 4.42 Aluminum backing plate behind 18 mm thick TiB plate

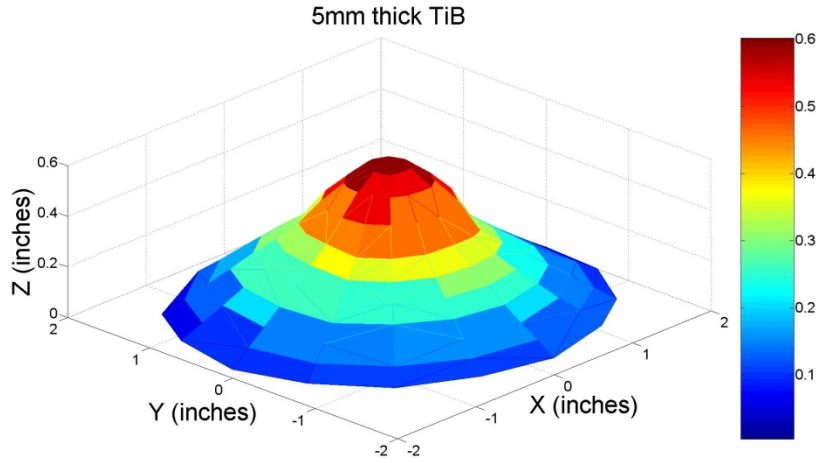

Fig. 4.43 Deformation profile of aluminum backing plate behind 5 mm thick TiB plate

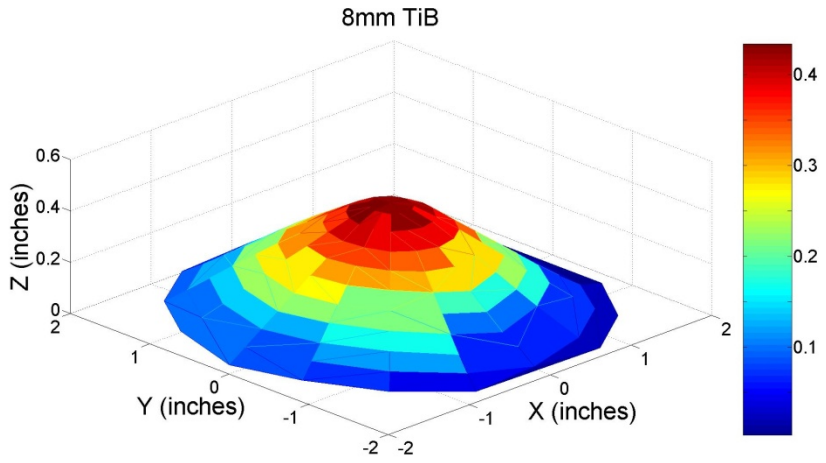

Fig. 4.44 Deformation profile of aluminum backing plate behind 8 mm thick TiB plate

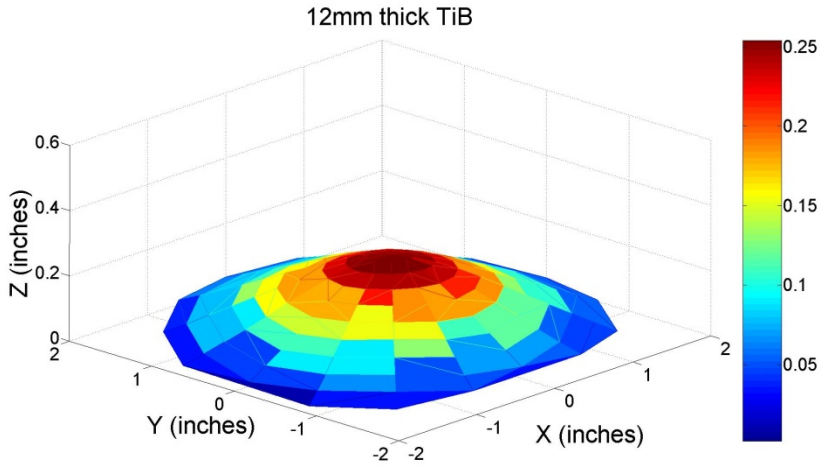

Fig. 4.45 Deformation profile of aluminum backing plate behind 12 mm thick TiB plate

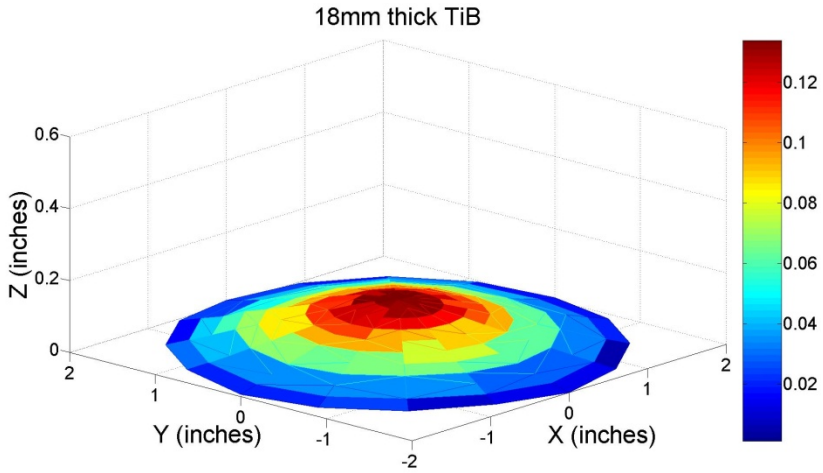

Fig. 4.46 Deformation profile of aluminum backing plate behind 18 mm thick TiB plate

Table 4.2 Energy spent in fragmentation for all the tested TiB plates

Sample	Ceramic thickness (mm)	Total area created (cm^2)	Fragmentation energy (J)	Bullet velocity (m/s)	Kinetic energy of bullet (J)	% of total energy spent in fragmentation
TiB 5b	5	544	3.11	727	2539	0.12
TiB 5c	5	626	3.57	735	2592	0.14
TiB 6.5b	6.5	750	4.28	753	2725	0.16
TiB 6.5c	6.5	698	3.98	741	2638	0.15
TiB 8b	8	707	4.04	737	2605	0.16
TiB 8c	8	842	4.81	739	2622	0.18
TiB 10a	10	789	4.50	739	2622	0.17
TiB 10b	10	713	4.07	739	2622	0.16
TiB 12a	12	673	3.84	724	2515	0.15
TiB 12b	12	800	4.57	743	2648	0.17
TiB 14a	14	608	3.47	751	2705	0.13
TiB 14b	14	596	3.40	750	2701	0.13
TiB 15a	15	431	2.46	744	2657	0.09
TiB 15b	15	510	2.91	727	2539	0.11
TiB 17a	17	468	2.67	736	2599	0.10
TiB 17b	17	470	2.68	735	2596	0.10
TiB 18a	18	437	2.50	752	2716	0.09
TiB 18b	18	396	2.26	737	2609	0.09

kinetic energy that goes into fragmentation was less than 0.2% for all cases. The differences between the fractions of incident energy dissipated in fragmentation for different thicknesses are not significant.

4.2.5 Backing Plate Deformation Energy

Table 4.3 lists the energy used in backing plate deformation for all the plates shot, calculated using equations 3.1 and 3.2. The energy absorption by the aluminum backing plates varied from about 4.5 % to 53% of the total incident energy of the bullet. It was found that for the thin TiB plates (5 mm and 6.5 mm thick), the energy that went into

Table 4.3 Work done in backing plate deformation for the tested TiB plates

Sample name	Bullet kinetic energy (J)	Work done in stretching (J)	Work done in bending (J)	Total backplate deformation energy (J)	% of total energy used in backplate deformation
TiB 5b	2539	861	328	1189	**46.8**
TiB 5c	2592	710	444	1154	44.5
TiB 6.5b	2725	945	499	1444	53.0
TiB 6.5c	2638	614	446	1060	40.2
TiB 8b	2605	369	359	728	27.9
TiB 8c	2622	567	392	959	36.6
TiB 10a	2622	184	263	447	17.0
TiB 10b	2622	186	267	454	17.3
TiB 12a	2515	125	221	346	13.7
TiB 12b	2648	119	210	329	12.4
TiB 14a	2705	88.0	182	270	9.99
TiB 14b	2701	86.9	181	268	9.93
TiB 15a	2657	32.9	94.1	127	4.78
iB 15b	2539	45.7	133	178	7.02
TiB 17a	2599	36.8	125	161	6.21
TiB 17b	2596	34.5	114	148	5.71
TiB 18a	2716	33.1	110	143	5.26
TiB 18b	2609	24.0	92.8	117	**4.48**

backing plate deformation was about 45 to 55% of the initial bullet energy whereas for the thicker TiB plates (17 mm and 18 mm thick), it accounted for only 5% of the bullet energy. The backing plate deformation energy decreased as the thickness of the ceramic plate increased which indicates increasing resistance of the TiB plate to the bullet motion However, beyond a certain thickness, the residual energy does not decrease much.

The backing plate deformation consists of two mechanisms: (a) bending and (b) tensile stretching of the plate. Table 4.3 also lists the relative values of the work done in

bending and stretching of the plate. The fraction of work done in tensile stretching of the backing plate was higher for the aluminum plates behind thinner TiB targets. This explains the presence of plugs and tensile cracks on the rear surfaces of some aluminum plates placed behind 5 mm and 6.5 mm thick TiB samples. In these cases, the projectile might not have been entirely defeated by the ceramic and thus would have continued to penetrate the aluminum plate after going through the ceramic thickness.

On the other hand, for the thicker plates, bending was the more dominant mechanism. This suggests that the ceramic entirely disintegrates the projectile and distributes the impact via the fracture conoid onto the backing plate over a large area. This causes a curvature in the aluminum plate which is created due to the bending loads and hence, more work is done in bending than in tensile stretching.

4.2.6 Other Mechanisms of Energy Absorption

Some of the bullet energy would be spent in deforming itself. In all the trials, it was observed that the bullet was completely eroded. The copper jacket was stripped off the lead core and torn into very small pieces. The lead core also was eroded into fine fragments. Typical debris of the projectile is shown in Figure 4.47.

Videos of the impact tests showed emission of light sparks from the flying fragments just after impact (Figures 4.48 and 4.49). This phenomenon of emission of light under mechanical loading is known as mechanoluminescence. The luminescence is believed to be caused due to the creation of new surfaces during fracture. Studies have shown that the amount of light produced during such an impact is directly related to the surface area created [85].

The TiB fragments were found dispersed throughout the chamber and they dented

Fig. 4.47 Debris from a bullet after impact with a TiB plate

Fig. 4.48 Light emission from fragments of 12 mm thick TiB plate after impact

Fig. 4.49 Light emission from fragments of 6.5 mm thick TiB plate after impact

the Lexan sheet separating the test chamber from the cage. Thus, the ejected fragments carry off some energy through their flight. It is difficult to calculate this kinetic energy of the fragments and requires high speed image capturing techniques such as X-ray photography. Apart from previously mentioned mechanisms, some energy is lost in the form of sound, heat due to friction during penetration, and also by the shock waves traveling through the ceramic and the backing plate.

CHAPTER 5

DISCUSSION

5.1 Energy Absorption Mechanisms in Mild Steel Plates

In metallic plates, the principal mechanisms through which the initial energy of a bullet is dissipated include ductile hole (or crater) formation, displacement of material from the projectile path, stretching, and bulging of the plate [86]. Some energy is also lost in the form of friction between the advancing projectile and the plate material. It has been found that there is a transition in the penetration mode from ductile hole formation to bulging when the plastic deformation zone reaches the rear surface of the plate. In the first phase, the plastic zone is constrained and the major portion of the energy is dissipated through ductile hole formation. In the bulging phase, the penetration is unconstrained and the energy is primarily consumed in plate bending and stretching.

For the thinner plates (where the plate thickness to the bullet diameter ratio is less than 1), the bulging mode is more dominant at reasonably high velocities and at very high velocities, tensile cracking or plug ejection is observed. For the thicker plates, a greater fraction of the incident energy is spent in ductile hole formation. For these plates, as the bullet velocity increases, there will be a transition in the penetration mode at a certain velocity when the plastic deformation zone reaches the rear surface of the plate.

As observed in Figure 4.18, for the 9.5 mm thick plates placed against the stainless steel backing plate, the penetration depth does not change significantly with

increasing bullet velocity. The ratio of depth of penetration to the plate thickness is almost constant, around 1.2, which indicates that the bulging is significant as the bullet has gone through the plate thickness. As bulging is the more dominant mechanism, the penetration depth remains independent of the bullet velocity. The major part of the energy goes into stretching and bending of the plate on the rear surface and not in the crater formation.

For the 15.9 mm and 19.1 mm thick mild steel plates tested against the aluminum backing plate, as seen in Figures 4.19 and 4.20, the penetration depth is always less than the plate thickness. This indicates that the bulging is not as severe as in the case of 9.5 mm thick plates. The penetration depth increases steeply for lower bullet velocities but the slope becomes gentle at higher velocities. Silsby [87] observed a similar trend for armor steel targets against tungsten alloy long rod projectiles moving at velocities between 1.3 to 4.5 km/s. In those experiments, it was also observed that the projectile deformed after impact and was eroded during penetration.

The plateau in the penetration depth or the crater volume vs. velocity curves might appear because of the transition in the dominant penetration mechanisms from ductile hole penetration to plate bending or stretching. Apart from ductile hole formation, the other processes which consume the energy are the following:

1. bulging which includes the bending and stretching of the plate.
2. displacement of the plate material from the path of the projectile.
3. deformation of the projectile.
4. friction between the projectile and the plate material.

Among these, bulging would be most dominant when the normalized penetration

depth approaches unity. The energies spent in material displacement and friction increase with velocity, often showing a v^2 dependence [86]. Thomson [88] estimated the dynamic work related to displacement of plate material, W_D, in the case of an ogival projectile to be

$$W_D = \pi R^2 h_0 \rho V^2 (R/L)^2 \quad (5.1)$$

where R and L are the radius and the ogive length of the bullet respectively, V is the bullet velocity, h_0, the initial plate thickness, and ρ, the plate density. This indicates that the contribution from this term will become more significant at higher velocities**.** The material displaced from the path of the penetrating projectile could either flow back along the sides of the deforming projectile towards the mouth of the crater or could be pushed ahead, as in the case of bulging.

The frictional energy increases for higher velocities because of increased contact area for greater penetration depths and higher values of the sliding friction [89]. However, it is difficult to quantitatively calculate the frictional energy. Krafft [90] estimated this to be only about 3% of the impact energy of the projectile. If the lip height is not significant, most of the material flow would occur in the direction of the projectile and hence, the frictional effects can be ignored [86].

5.2 Role of Backing Plate

For the batch of 9.5 mm thick mild steel plates shot against the stainless steel backing plate, it was found that complete penetration was observed at a velocity of 823 m/s. Then, when the stainless steel backing was replaced by an aluminum plate, the bullet

completely penetrated the 9.5 mm thick mild steel plate even at a lower velocity of 744 m/s. This suggests that in the first case, the stainless steel backing contributed more to the dissipation of the incident kinetic energy of the bullet than the softer aluminum backing plate. As discussed in Section 2.2., a compressive shock wave travels through the target plate until it reaches the backing plate interface, after which it is reflected. A compressive wave then passes through the backing material as well, which absorbs a portion of the energy.

To estimate the ballistic efficiency of a material accurately, it is essential to remove the role of the backing plate during the impact. Hence, for ceramic testing, it was decided to design a setup where the ceramic armor system would be isolated from the larger backing plate. Since a backing plate was still required to measure the residual penetration after the projectile defeats a ceramic, the armor system consisted of the ceramic plate glued to a 6.3 mm thick, 100 mm by 100 mm square aluminum plate, which is a more realistic alternative to the larger 450 mm by 450 mm backing plate used with mild steel targets.

5.3 Differences between Penetrations in Mild Steel and TiB Plates

The response to high velocity impact in a ceramic is very different from that in a metallic plate, even for similar thicknesses and bullet velocities. A ceramic distributes the load over a larger area than a metallic plate. Figures 5.1 and 5.2 show the rear surfaces of an impacted mild steel plate and an aluminum backing plate glued to a TiB plate for similar impact velocities. The entire load of the bullet is concentrated in the small area of the bulge in the mild steel plate whereas the deformation is spread over a much larger area by the ceramic due to the formation of a fracture conoid originating from the impact

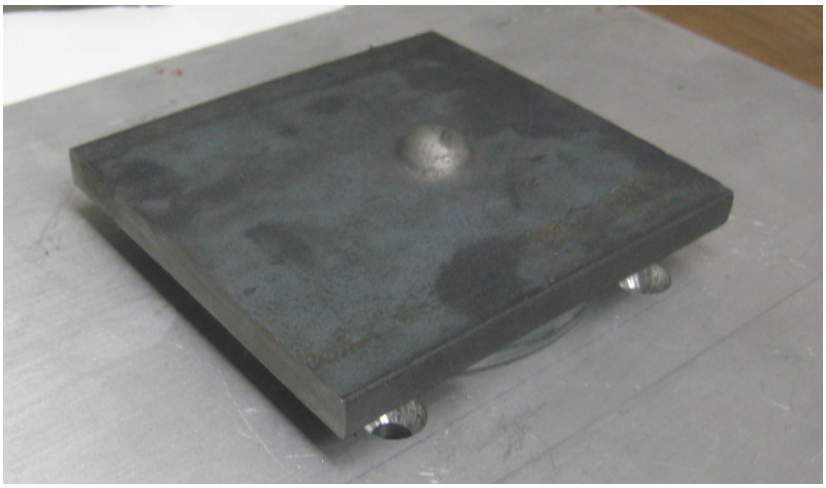

Fig. 5.1 Rear surface of an impacted mild steel plate

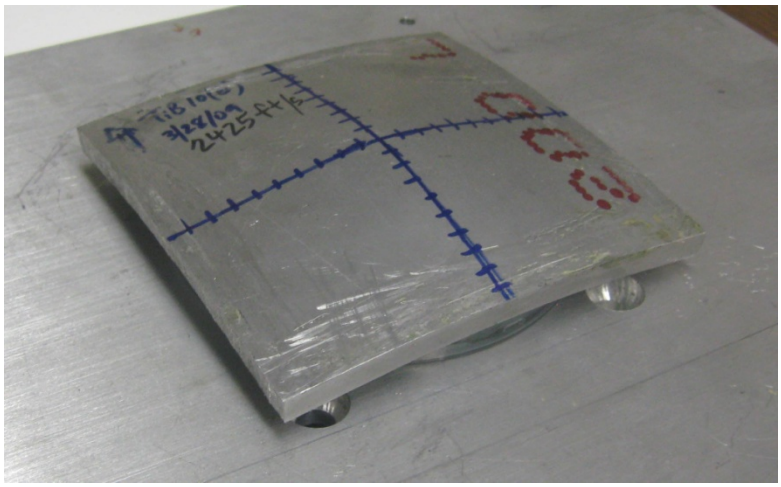

Fig. 5.2 Deformed surface of an aluminum backing plate glued to an impacted TiB plate

point. The localized bulge formation was observed at the rear surfaces for mild steel plates of all thicknesses. On the other hand, in the case of ceramic plates, even though there was bending of the aluminum backing for all the thicknesses, for the thinner ceramics, there was also some localized tensile stretching due to insufficient protection provided by the ceramic, as was seen in Figures 4.40 and 4.43.

The bullet erosion is more severe in the case of ceramic plates due to the higher hardness. In penetration of the mild steel plates, the copper jacket is stripped off the bullet and the lead core is deformed during penetration (see Figure 4.3(b)). But the copper jacket and the lead core were still intact. On the other hand, ceramic plate causes the stripped copper jacket and the lead core to be torn into small pieces (see Figure 4.47). This is beneficial because in the case of mild steel plates, in the event of complete penetration, the deformed lead core still can have some residual velocity and cause further damage.

5.4 Energy Absorption Mechanisms in Ceramic Plates

It was attempted to determine the amount of ballistic energy dissipated through various processes after ballistic impact on the TiB plates. Some of these important processes are the following:

1. The fragmentation of the ceramic.
2. The kinetic energy of the fragments.
3. The plastic deformation of the backing plate.
4. The erosion of the projectile.
5. Heat lost in friction, sound, light, and shock waves.

Of these, (1) and (3) have been calculated in this research. The fragmentation of

the ceramic was found to be a very small percentage of the total initial kinetic energy of the projectile (less than 0.2%). The work done in plastic deformation of the backing plate varied from about 50% to 5% of the initial kinetic energy of the bullet for the TiB plates with thicknesses between 5 mm and 18 mm, respectively. Table 5.1 lists the percentages of the bullet energy used in back plate deformation and ceramic fragmentation. The percentage of the bullet energy unaccounted ranges from 53% to 95.4%. This energy could be in the form of 2, 4, or 5.

The disintegration of the projectile involves stripping of the copper jacket from the lead core after which both get torn into small pieces. Researchers have claimed that the work done in stripping the copper jacket is negligible (< 0.01 kJ) compared to the initial energy of the bullet [90]. The maximum energy spent in bullet erosion would be roughly of the order of the product of the yield strength and the volume of the projectile [40]. Since lead has a low value of yield strength and the bullet volume is small, this energy would not be a significant fraction of the total kinetic energy.

Therefore, it can be safely assumed that the major portion of the incident energy is carried off by the kinetic energy of the ceramic fragments and the debris. Pavel *et al*. [89] have demonstrated, through spark cinematography of glass perforation by impacting projectiles, that the fragments were ejected at velocities close to that of the incoming projectile. Ballistic pendulum experiments conducted by Woodward *et al*. [84] also showed fragment ejection velocities obtained through radiographs to be as high as 50% of the incident velocity. The residual kinetic energy in that experiment was calculated to be roughly 34% of the incident energy. Hence, the flight of the fragments can be thought of as the most important energy absorbing mechanism for the ceramics. It can account for

Table 5.1 Energy partitioning of a ballistic impact on TiB ceramic plates

Sample	Bullet Kinetic Energy (J)	Fragmentation Energy (J)	% of Total Energy used in fragmentation	Back plate Deformation Energy (J)	% of Total Energy used in Back plate Deformation	% of Total Energy unaccou-nted
TiB 5b	2539	3.11	0.12	1189	46.8	53.0
TiB 5c	2592	3.57	0.14	1154	44.5	55.3
TiB 6.5b	2725	4.28	0.16	1444	53.0	46.8
TiB 6.5c	2638	3.98	0.15	1060	40.2	59.6
TiB 8b	2605	4.04	0.16	728	27.9	71.9
TiB 8c	2622	4.81	0.18	959	36.6	63.2
TiB 10a	2622	4.50	0.17	447	17.0	82.8
TiB 10b	2622	4.07	0.16	454	17.3	82.5
TiB 12a	2515	3.84	0.15	346	13.7	86.1
TiB 12b	2648	4.57	0.17	329	12.4	87.4
TiB 14a	2705	3.47	0.13	270	9.99	89.9
TiB 14b	2701	3.40	0.13	268	9.93	89.9
TiB 15a	2657	2.46	0.09	127	4.78	95.1
TiB 15b	2539	2.91	0.11	178	7.02	92.9
TiB 17a	2599	2.67	0.10	161	6.21	93.7
TiB 17b	2596	2.68	0.10	148	5.71	94.2
TiB 18a	2716	2.50	0.09	143	5.26	94.6
TiB 18b	2609	2.26	0.09	117	4.48	95.4

almost all of the 50% to 95% energy that was consumed by the ceramic plates.

Though the fragmentation by itself does not influence the ballistic behavior to a significant extent, it seems to determine the amount of energy carried off through the flight of the fragments. The more the mass of the ejected fragments and higher their velocities, the more will be the energy consumed in the flight. The energy consumed in the flight can be thought of as:

$$E_{flight} = \sum_{i=1}^{N} \frac{1}{2} m_i v_i^2 \tag{5.2}$$

where N is the total number of fragments created, m_i is the mass of the i^{th} fragment, and v_i its velocity. If v_i value reaches a fraction of the initial bullet velocity and a lot of fragmentation occurs, *i.e.*, N is large, then the E_{flight} can form a sizeable fraction of the incident kinetic energy.

It is important to note that some energy will be used up in the form of heat, sound, light, shock waves, and through the impact delivered to the confining mild steel plates. These, although not quantified in the present research, are likely to be smaller compared to the energy partitioning in back plate deformation and fragment flight.

5.5 Ceramic Thickness vs. Ballistic Efficiency

The net ballistic energy absorbed by the ceramic alone can be defined as the kinetic energy of the bullet minus the residual energy used up in backing plate deformation. The ceramic defeats the bullet through fragmentation and ejection of the fragments, disintegration of the bullet, and the heat generated due to friction during

penetration. Figure 5.3 shows the net energy absorbed by the ceramic alone, plotted against the ceramic thickness for all the trials. For the initial thicknesses, increase in the thickness results in greater ballistic resistance. But increasing the thickness beyond 15 mm does not necessarily increase the ballistic energy absorbed by the ceramic. This indicates that the projectile is entirely defeated within the ceramic and any further increase in the thickness is only likely to add to the weight of the armor system without significantly improving the ballistic resistance.

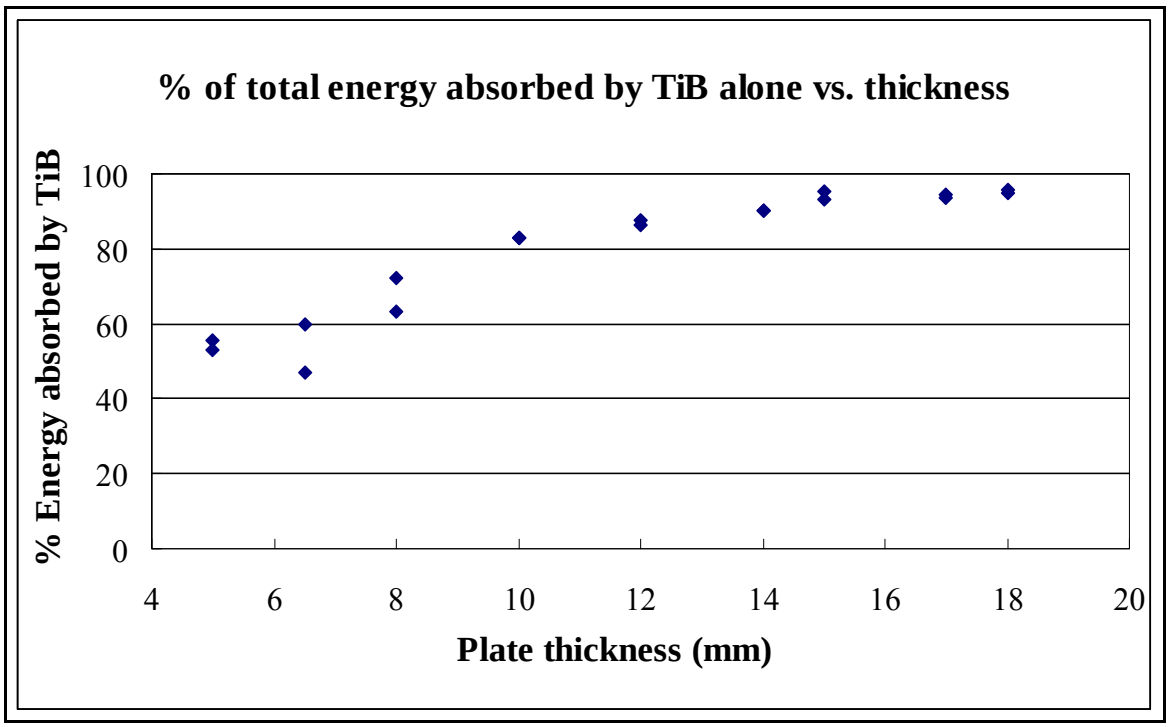

Fig. 5.3 Percentage of bullet energy absorbed by TiB alone vs. plate thickness

CHAPTER 6

CONCLUSIONS

The conclusions of this research can be summarized as the following:

1. A ballistic testing unit was successfully set up. By varying the amount of gunpowder loaded into the bullets, a reasonable control over the bullet velocity was obtained. Given a particular gunpowder load, the velocity could be predicted within a range of 30 m/s which is less than 2% of standard deviation. The velocities obtained were in the range of 715 m/s to 825 m/s.
2. The impacted mild steel plates absorbed the bullet energy by localized plastic deformation which is manifested as crater formation on the front surface and bulging on the rear. Complete penetration was observed in the 9.5 mm thick mild steel plates at higher velocities whereas the 15.9 mm and 19.1 mm thick plates only showed partial penetration. The crater volume had a better correlation with bullet velocity than the penetration depth. It was found that for the 9.5 mm thick mild steel plates, dishing was a more dominant mechanism of energy absorption than ductile hole formation. In the plates of thicknesses 15.1 mm and 19.1 mm, a transition in the energy dissipation mode from ductile hole formation to dishing was observed.
3. In the TiB plates, the proportion of the coarser fragments generally increased

with plate thickness. Also, in the thicker plates, the zone of comminution was confined to a small region at the center of the plate. The surface of the fragments outside this region was undamaged. This comminution zone extended almost up to the edges for the thinner plates (5 mm to 8 mm thick), thus resulting in a higher mass percentage of finer fragments.

4. The fragmentation energy of TiB plates was found to be negligible for all thicknesses, when compared with the incident kinetic energy. In all the cases, it comprised less than 0.2% of the initial bullet energy. The lead core and the copper jacket of the bullet were eroded and torn into pieces after impact with the TiB plates. The flight of the fragments followed by the erosion of the bullet can be thought of as the most important energy dissipation mechanisms for the TiB plates.
5. If the energy absorbed by the TiB plates only (the total bullet energy minus the backplate deformation energy) is considered, it was found that this energy increased more steeply with thickness for the thinner plates (5 mm to 12 mm). Increasing the thickness beyond 15 mm did not cause a significant increase in the energy absorbed by ceramic. Plates with thicknesses less than 8 mm did not show good ballistic resistance.

REFERENCES

1. M.J. Normandia and W.A. Gooch: *Ceram. Trans.,* 2002, vol. 134, pp. 113-38.

2. P. Gonçalves, F.C.L De Melo, A.N. Klein, and H.A. Al-Qureshi: *Int. J. Mach. Tools Manuf.,* 2004, vol. 44 (2-3), pp. 307-16.

3. C. Kaufmann, D. Cronin, M. Worswick, G. Pageau, and A. Beth: *Shock and Vibration,* 2003, vol. 10, pp. 51-58.

4. M.L. Wilkins, C.F. Cline, and C.A. Honodel: *Fourth Progress Report of Light Armor Program,* 1969, Report No UCRL 50694.

5. B. Matchen: *Final Report, Joint US-Canadian Defense Development Sharing Project on Ceramic Armor Material,* 1969, Contract No DAAG46-68-0096.

6. B. Matchen: *Key Eng. Mater.,*1996, vol. 122-124, pp. 333-42.

7. J.P. Moskowitz: US Patent 4739690, April 1988.

8. D.J. Viechnicki, M.J. Slavin, and M.I. Kliman: *Ceram. Bull.,* 1991, vol. 70, pp. 1035-38.

9. J. Rioux, C. Jones, M. Mandelartz, and V. Pluen: *Adv. Mater. Processes,* 2007, vol. 165(10), pp. 31-33.

10. S. Madtha, C. Lee, and K.S.R. Chandran: *J. Am. Ceram. Soc.,* 2008, vol. 91(4), pp. 1319-21.

11. M.W. Barsoum: *Fundamentals of Ceramics,* Taylor and Francis Group, New York, NY, 2003, p. 2.

12. R.W. Rice: *Mechanical Properties of Ceramics and Composites: Grain And Particle Effects*, Marcel Dekker, Inc., New York, NY, 2000, pp. 127-314.

13. S.C. Carniglia: *J.Am.Cer.Soc.,* 1965, vol. 48(11), pp. 580-83.

14. R.W. Rice, C.Cm. Wu, and F. Borchelt: *J.Am. Cer. Soc.,* 1994, vol. 77(10), pp. 2539-53.

15. R.W. Rice: *J. Mat.Sci,* 1996, vol. 31, pp. 1969-83.

16. R.W. Rice: *J. Mat.Sci,* 1996, vol. 31, pp. 4503-19.

17. R.L. Woodward and B.J. Baxter: *Int. J. Impact. Eng,* 1993, vol. 15(2), pp. 119-24.

18. P.C. Den Reijer: *Dissertation,* Technische Univ. Delft (Netherlands), 1991.

19. D. Viechnicki, W. Blumenthal, M. Slavin, C. Tracy, and H. Skeele: *Third TACOM Armor Coordinating Conference*, 1987, pp. 27-53.

20. D.A. Shockey, A.H. Marchand, S.R. Skaggs, G.E. Cort, M.W. Burkett, and R. Parker: *Int. J. Impact Eng,* 1990, vol. 9, pp. 263-75.

21. M.L. Wilkins: *Int.J. Eng. Sci.,* 1978, vol. 16, pp. 793–807.

22. E. Medvedovski: *Am. Ceram. Soc. Bull.,* 2002, vol. 81(4), pp. 45-50.

23. Z. Rosenberg: *Int. J. Impact Eng,* 1990, vol. 9, pp. 45–49.

24. J. Sternberg: *J. Appl. Phys.*,1989, vol. 65, pp. 3417–24.

25. E. Medvedovski: *Am. Ceram. Soc. Bull.,* 2002, vol. 81, pp. 27-32.

26. J. B. Wachtman: *Mechanical Properties of Ceramics*, John Wiley & Sons, Inc., New York, NY, 1996, pp. 357-86.

27. E. Dorre and H. Hubner: *Alumina Processing, Properties and Applications*, Springer-Verlag Berlin, Heidelberg, 1984, p. 75.

28. J.H. Park, Y.H. Lee, Y.H. Koh, H.E. Kim, and S.S. Baek: *J. Am. Ceram. Soc.,* 2000, vol. 83, pp. 1542-44.

29. R.G. Munro: *J. Res. Nat. Inst. Stand. Technol.,* 2000, vol. 105, pp. 709-20.

30. M.A. Kuzenkova, P.S. Kislyi, B.L. Grabchuk, and N.I. Bodnaruk: *J. Less Common Metals*, 1979, vol. 67, pp. 217-23.

31. S. Yamada, Sakaguchi, K. Hirao, Y. Yamauchi, and S. Kanzaki, *Ceram. Eng. Sci. Proc.,* 2001, vol. 22, pp. 215-20.

32. R.F. Davis, J.E. Lane, C.H. Carter Jr., J. Bentley, W.H. Wadlin, D.P. Griffis, R.W. Linton, and K.L. More: *Scan. Electron. Micros.,* 1984, vol. 3, pp. 1161-67.

33. J. Thomson: *Key Eng. Mater.,* 1991, vol. 53-55, pp. 575-78.

34. E. Medvedovski: *Ceram. Trans.*, 2006, vol. 178, pp. 3-17.

35. B.A. Cheeseman and T.A. Bogetti: *Compos. Struct.,* 2003, vol. 61, pp.161-73.

36. J.M. Salame´: *Personal Armour Systems Symposium*, 2000, pp. 327-36.

37. T.A. Mirzeabasov: *Personal Armour Systems Symposium*, 2000, pp. 211-34.

38. D. Cronin: Contract Report, *DREV CR 2000-146*, Defence R&D Canada, 2000.

39. A. Kelly: *Concise Encyclopedia of Composite Materials*, Elsevier Science Inc, Tarrytown, NY, 1994, pp. 58-59.

40. C. Ruiz: *Int. Conf. Mech. Prop. Materials at High Rates of Strain*, 1989, Oxford, pp. 337-53.

41. S.K. Chung: *Am. Ceram. Soc. Bull.,* 1990, vol. 69(3), pp. 358 - 66.

42. S.C. Chou, A. M. Rajendran, and D.J. Grove: *Conference on Structural Stability and Dynamics*, December 16-18, 2002, Singapore, vol. 1, pp. 987-96.

43. F. Huang and L. Zhang: *AIP Conf. Proc.*, 2006, vol. 845(1), pp. 1383-86.

44. P. Woolsey, S. Mariano, and D. Kokidko: *Proceedings of the 5th Annual TACOM Armor Coordinating Conference for Combat Vehicles (U)*, 1987, vol. 1, pp. 195-212.

45. R.R. Franzen, D.L. Orphal, and C.E. Anderson Jr: *Int. J. Impact. Eng.,* 1997, vol. 19(8), pp. 727-37.

46. Z. Rosenberg and Y. Yeshurun: *Int. J. Impact. Eng.,* 1988, vol. 72, pp. 357-62.

47. N.K. Bourne and J.C.F. Millet: *J. Phys. IV France*, 2000, vol. 10, pp. 281-86.

48. P. Li: *Dissertation*, Beijing Institute of Technology, 2002.

49. Z. Rosenberg, E. Dekel, V. Hohler, A.J. Stilp, and K. Weber: *10th Am. Phys. Soc. Top. Conf. Shock Compres. Condens. Mater.,* 1998, vol. 429, pp. 917-20.

50. V.A. Hohler, J. Stilp, and K. Weber: *Int. J. Impact. Eng.*, 1995, vol.17, pp. 409-18.

51. G.E. Hauver, P.H. Netherwood, R.F. Benck, and L.J. Kecskes: *Proceedings of the 13th Army Symposium on Solid Mechanics*, 17–19 August 1993, Plymouth, MA, pp. 23-34.

52. P. Lundberg, R. Renstrom, and B. Lundberg: *Int. J. Impact Eng.*, 2000, vol. 24(3), pp. 259-75.

53. R.L.Woodward, W.A.Gooch, R.G.O'Donnell, W.J.Perciballi, B.J.Baxter, and S.D.Pattie: *Int. J. Impact Eng.*, 1994, vol. 15(5), pp. 605-18.

54. B. Heidenreich, M. Gahr, E. StraDburger, and E. Lutz: *Advances in ceramic armor II, Ceram. Eng. Sci. Proc.*, 2006, vol. 27(7), pp. 20-31.

55. S.R. Skaggs: *27th Annual Cocoa Beach Conference on Advanced Ceramics and Composites, Ceram. Eng. Sci. Proc.,* 2008, vol. 24(3), pp. 337-49.

56. J.M. Staehler, W.W. Predebon, and B.J. Pletka: *US Patent 5352643*, 4 October 1994.

57. G. Fanchini, D.E. Niesz, R.A. Haber, J.W. McCauley, and M. Chhowalla: *Advances in Ceramic Armor II, Ceram. Eng. Sci. Proc.,* 2008, vol. 27(7), pp. 179-88.

58. D. Maiorano, R. Haber, and G. Fanchini: *Advances in Ceramic Armor II, Ceram. Eng. Sci. Proc.*, 2008, vol. 27(7), pp. 189-95.

59. M. Chen, J.W. McCauley, and K.J. Hemker: *Science*, 2003, vol. 299, pp. 1563 - 66.

60. D. Ge, V. Domnich, T. Juliano, E.A. Stach, and Y. Gogotsi: *Acta Mater.*, 2004, vol. 52, pp. 3921-27.

61. F. Thevenot: *J. Eur. Ceram. Soc*, 1990, vol. 6, pp. 205–25.

62. I. Pickup: *Ceram. Eng. Sci. Proc.*, 2005, vol. 26(7), pp. 77-88.

63. W. Krenkel: *Dissertation*, Universitat Stuttgart, 2000.

64. C. Ziccardi and R. Haber: *Advances in Ceramic Armor II, Ceram. Eng. Sci. Proc.*, 2008, vol. 27(7), pp. 97-103.

65. D.E. Grady: *J. Phys. IV*, 1994, vol. 4(8), pp. C8-385 - C8-391.

66. T.J. Holmquist and G.R. Johnson: *J. Appl. Phys.*, 2006, vol. 100(9), pp. 93525-1-13.

67. J.E. Reaugh, A.C. Holt, and M.L. Wilkins: *Int. J. Impact Eng*, 1999, vol. 23, pp. 771-82.

68. G. Gilde, J.W. Adams, M. Burkins, M. Motyka, P.J. Patel, E. Chin, L. P. Franks, M. Sutaria, and M.J. Rigali: *25th Annual Conference on Composites, Advanced Ceramics, Materials, and Structures: A Ceram. Eng. Sci. Proc.*, 2008, vol. 22(3), pp. 331-42.

69. A. Pettersson, P. Magnusson, P. Lundberg, and M. Nygren: *Int. J. Impact Eng*, 2006, vol. 32, pp. 387-99.

70. R.G. O'Donnell: *J. Mater. Sci. Lett.*, 1992, vol. 11, pp. 1227-30.

71. T.J. Moynihan, S.C. Chou, and A.L. Mihalcin: ARL- TR 2219, *US Army Research Laboratory,* 2000, Aberdeen Proving Ground, MD.

72. C. Roberson and P.J. Hazell: *Ceram. Trans.*, 2003, vol. 151, pp. 153-63.

73. L.R. Vyshnyakov, A.V. Mazna, A.V. Neshpor, V.A. Kokhanyi, and O.N. Oleksyuk: *Strength Mater.*, 2004, vol. 36(6), pp. 643-48.

74. K.B. Panda and K.S. Ravichandran: *Metall. Mater. Trans. A*, 2003, vol. 34, pp. 1993-2003.

75. S.S. Sahay, K.S. Ravichandran, R. Atri, B. Chen, and J. Rubin: *J.Mater.Res.,* 1999, vol. 14, pp. 4214-23.

76. *Binary Alloy Phase Diagram*, *ASM Handbook,* H. Baker, ed., ASM International, Materials Park, OH, vol. 3, p. 2.85, 1993.

77. M.E. Hyman, C. McCullough, J.J. Valencia, C.G. Levi, and R. Mehrabian: *Metall. Trans. A,* 1991, vol. 22(7), pp. 1647-62.

78. B.F. Decker and R. Kasper: *Acta Crystallogr.,* 1954, vol. 7, p. 77.

79. M. De Graef and J.P.A. Lofvander: *Acta Metall. Mater.,* 1991, vol. 39, pp. 2381-91.

80. J.A. Philliber, F.C. Dary, F.W. Zok, and C.G. Levi: *TMS-AIME Proceedings*, P.K. Rohatgi, ed., TMS-AIME, Warrendale, PA, 1996, pp. 55-66.

81. R. Atri: *Dissertation*, University of Utah, Salt Lake City, UT, 2000.

82. U. Leushake, A.N. Winter, B.H. Rabin, and B.A. Corff: *Mater. Sci. Forum*, *Proceedings of the 5th International Symposium on Functionally Gradient Materials*, Trans Tech Publications, Uetikonzeurich, Switzerland, 1999, vol. 308-11, pp. 13-18.

83. Z. Wyatt: *Report*, University of Utah, Salt Lake City, UT, 2007.

84. R.L. Woodward, R.G. O'Donnell, B.J. Baxter, B. Nicol, and S.D. Pattie: *Mater. Forum*, 1989, vol. 13, pp. 174-81.

85. B. P. Chandra, M. S. Khan, and M. H. Ansari: *Cryst. Res. Technol.*, 1998, vol. 33(2), pp. 291-302.

86. S.N. Dikshit: *Defence Science Journal*, April 1998, vo1. 48(2), pp. 185-95.

87. G. F. Silsby: *Proceedings of the Eighth International Symposium on Ballistics*, TB/31-35, 1984, Orlando, Florida.

88. W. Pavel, H.J. Raatschen, R. Schwartz, H. Senf, J.F. Kalthoff, and S. Winkler: *Proc. 3rd Oxford Conference, Inst. Of Physics Conf. Ser. No. 70*, 1984, pp. 291-98.

89. W.T. Thomson: *J. Appl. Phys.*, 1955, vol. 26(1), pp. 80-82.

90. S.N. Dikshit and G. Sundararajan: *Int. J. Impact Eng*, 1992, vol. 12(3), pp. 373-408.